UNIVERSITY OF CALIFORNIA
SANTA CRUZ

THE MAGNETIC AND PLASMONIC PROPERTIES OF METAL AND METAL-OXIDE NANOPARTICLES AND THEIR APPLICATIONS

A dissertation submitted in partial satisfaction
of the requirements for the degree of

DOCTOR OF PHILOSOPHY

in

CHEMISTRY

by

Staci A. Adams

March 2018

The dissertation of Staci A. Adams is approved:

_____
Professor Jin Z. Zhang, chair

_____
Professor Scott Oliver

_____
Professor Yat Li

_____
Tyrus Miller
Vice Provost and Dean of Graduate Studies

Table of Contents

List of Figures

List of Tables

List of Symbols

AMF: applied magnetic field

B: magnetic induction

C_{abs}: absorption contribution to the extinction cross-section

C_{ext}: extinction cross-section

DMEM: Dulbecco's modified eagle's medium

EDS: energy dispersive spectroscopy

EDX: energy dispersive x-ray

EGR: epidermal growth factor

EM: electromagnetic

EPR: electron paramagnetic resonance

***f*:** fraction of the core volume

FBS: fetal bovine serum

FTIR: Fourier transform infrared

FWHM: full width half maximum

H: applied magnetic field

ħ: Planck's constant/2Π

HAADF-STEM: high angular dark field scanning transmission electron microscopy

HAuNS: hollow gold nanosphere

H_C: coercivity

HCP: hexagonal close packed

HGN: hollow gold nanosphere

HGSC: hollow gold-silica composite

HGSDS: hollow gold-silica double shell

HRTEM: high resolution transmission electron microscopy

IL-PVS: intra-lymphatic primo vascular system

LSPR: localized surface plasmon resonance

LV: lymphatic vessels

M: magnetism

m: mass

M_R: magnetic retentivity

MRI: magnetic resonance imaging

M_S: magnetic susceptibility

NIR: near infrared

NIRF: near infrared fluorescence

NP: nanoparticle

OAT: optical acoustic tomography

ϕ: one flux quantum

PAT: photo acoustic tomography

PCF: photonic crystal fiber

PET: positron emission tomography

PN: primo node

PTA: photothermal ablation therapy

PV: primo vessel

PVS: primo vascular system

PXRD: powder X-ray diffraction

QD: quantum dot

R: particle radius

S/V: surface to volume ratio

SEM: scanning electron microscopy

SERS: surface enhanced Raman scattering

SHE: standard hydrogen electrode

SPR: surface plasmon resonance

SQUID: superconducting quantum interference device

sub-PV: primo sub-vessel

T: tesla

T_C: critical temperature

TEM: transmission electron microscopy

T_N: Neel temperature

TPRS: two photon Rayleigh scattering

UV-Vis: ultra violet-visible

V: particle volume

XRD: X-ray diffraction

α: polarizability

β: first hyperpolarizability

ε_0: vacuum permittivity

ε_i: imaginary component of the complex dielectric constant

ε_m: dielectric constant of surrounding medium

ε_r: real component of the complex dielectric constant

Λ: wavelength of light

λ_{max}: maximum wavelength of absorption

μ: permeability

χ: susceptibility

Abstract

Staci A. Adams

Magnetic and Plasmonic Properties of Metal and Metal-Oxide Nanoparticles and Their Applications

Nanomaterials are designed and synthesized for a wide range of applications including clinical diagnostics, therapeutics, the targeting of bioterrorism agents, wastewater treatment, energy, environmental remediation and sensing. In order to enhance performance in these fields researchers often work with materials that are either magnetic, plasmonic or a combination of both. Nanomaterials can be customized through synthetic variation in size, shape, aspect ratio, the dielectric constant of the surrounding media, surface morphology and whether particles are aggregated. Chapter 1 serves as an introduction to hollow gold nanospheres (HGNs) including their unique plasmonic properties and how these properties can be refined and harnessed for emerging applications. HGNs have hollow solvent filled dielectric cores and polycrystalline gold shells that, due to the two surfaces or interfaces, can generate an enhanced electromagnetic (EM) field. They possess a unique combination of properties that include small size (20-125 nm), large surface to volume (S/V) ratios, spherical shape, narrow and tunable SPR (~520-1000 nm) and biocompatibility. Their surfaces can also be easily functionalized to target and deliver biomolecules and are resistant to photobleaching. Additionally, their scattering and absorption cross-sections can be tailored, making them excellent candidates for a

variety of applications including surface enhanced Raman scattering (SERS), sensing, imaging, drug delivery, site specific silencing and photothermal therapies (PTTs). Chapter 2 describes the detailed synthetic mechanism for creating highly reproducible near infrared (NIR) absorbing HGNs with an emphasis on the cobalt seed particle growth step of the synthesis. Several studies describing HGNs and their applications are found in chapter 3. The first study investigates the interaction of HGNs with Cu^{2+}, commonly found *in vivo,* and the role that these ions play in aggregation, since aggregation can strongly influence the optical and photothermal properties of HGNs. The second study utilizes HGNs to visualize the Primo Vascular System (PVS) in a rat model. The use of hollow gold−silica double-shell (HGSDS) and hollow gold-silica composite (HGSC) nanostructures as surface enhanced Raman scattering (SERS) substrates for the detection of glucose is detailed in the third study found in chapter 3. Chapter 4 describes the synthesis of large Fe_3O_4@SiO_2 nanoparticles (~200 nm) functionalized with gold and poly(vinylpyrrolidone) synthesized for bio-separation and SERS sensing applications. These particles have a unique surface morphology comprised of roughened gold nodules. The surface coatings prevent oxidation and render the particles easy to functionalize in order to target a wide range of moieties. The gold coverage is not only uniform across the entire particle surface but also ultra-thin so as to maintain a high percentage of the cores magnetic saturation (~68%) when compared to bare magnetite. The gold nodules facilitate the generation of hot spots that enhance the EM associated with the particle surface and are useful in sensing applications like SERS spectroscopy whereas the strong magnetic core allows

for rapid separation (~30 s) of target molecules from solution once they are bound to the particles. Finally, in Chapter 5 the effect of polymer and gold functionalization on the magnetic properties of Fe_3O_4 nanoparticles is examined by superconducting quantum interference device (SQUID) and electron paramagnetic resonance (EPR) along with thoughts on future experimentation that can help to create a more complete story with respect to this unique nanocomposite material.

Dedication and Acknowledgments

I am grateful for the opportunity to be a part of Professor Jin Z. Zhang's laboratory. He has taught me what it means to be a scientist in today's world, how to develop patience and how to be more professional. I have appreciated his flexibility, his work ethic, his generosity, his feedback and his ability to afford independence to his graduate students. His mentorship is something I will never forget.

The Zhang Laboratory, in all its iterations, has impacted me deeply. Spending so much time in such a small a space with so many people has changed me as a person. I want to thank Sara Bonabi, Sarah Lindley, A'Lester Allen, Evan Vickers, Kurt Lindquist, Dalena Thai, Xiomara Mascona, Conner Leahy, Ghada Elmaghraby, Tzarara Lopez-Luke, Adam Schwartzberg, Dylan Simpson, Sarah Weaver, Binbin Luo, Zach Schwartz, Raymond Pu, Jason Cooper, Bob Fitzmorris, Carley Corrado, and so many more visiting scholars, graduate students and undergraduates who have called the Zhang lab home over the years.

I want to thank my committee members Professor Scott Oliver and Yat Li. They've seen me through my second year seminar, my orals, my annual reviews, my thesis and my dissertation. The scientist I've become has been influenced by their guidance and feedback.

I would like to give a special acknowledgment to Dr. Randa Roland for providing me with the opportunity to become a better teacher over the years, for hours of advice and for being a friend. I also want to thank Dr. Bin Chen for

mentoring me through my fellowship at NASA, Professor Arthur Ramirez for his help and feedback related to my magnetic research and Dr. Tom Yuzvinsky at the W.M. Keck Center for Nanoscale Optofluidics at UCSC for his electron microscopy imaging skills.

My projects over the years were supported by: ECCS-082391, the BES Division of the US DOE (DE-FG02-05ER46232), the US National Science Foundation, Delta Dental Plan Associates, the UCSC Faculty Special Research Fund, Smart Technologies, NASA through the MACES center at UC Merced (NNX15AQ01A) and UCSC Senate Special Research Fund.

I want to give a special acknowledgement to the comrades I have made along the way: Dr. Tianyu Liu for helping me keep things in perspective; Jesse Hauser for helping me keep one foot in front of the other (we've come a long way since our undergraduate physics study group); Dylan Simpson for keeping me laughing and Sara Bonabi for helping me pass the time in five different languages.

I want to acknowledge the Li lab, the Chen lab, the Oliver lab, the Ayzner lab, the Kliger lab, the Bogomolni lab and all the students and scientists who have come and gone through these labs over the years especially: Dr. Hanyu Wang, Jorge Jimenez, Pamela Schleissner, Vincent Duong, Will Hollingsworth, Michael Roders, Rafael Silverman and Gabe Mednick.

I want to acknowledge the Chemistry Department office and all the women working hard in it to keep our department running smoothly especially Janet Jones,

Karen Meece, and Patti Schell. They've all helped me to navigate this process with a little more ease and grace. I also want to thank Emma from Perks for thousands of shots of espresso over the years. (I did a rough calculation and estimate ~6600)

I want to thank Tanya Bashaw, Christina Sheppard and Dena Crowell for being like sisters to me. I couldn't have made it through without them. I also want to thank my grandparents for raising me and giving me a home in this world and always believing in me.

I want to dedicate this thesis to my best friend and the love of my life Daniel Capon. No one can understand all that we've been through and how far we've come together in this world. There is no one like him. He has been with me through every step of this process; always encouraging me, listening to me, supporting me and most importantly, keeping me smiling. I could not have done this without him. I love him with all my heart. Finally, I could not have done this without the love and support of our animals: Tasha, Scotchie, Mr. Luci, Agatha and Iggi.

The text of this dissertation includes reprints, in part or in whole, of the following previously published materials:

1. **Adams, S**., Hauser, J.L., Allen, A.C., Lindquist, K.P., Ramirez, A.P., Oliver, S., Zhang, J.Z. "*Fe_3O_4@SiO_2 Nanoparticles Functionalized with Gold and Poly(vinylpyrrolidone) for Bio-Separation and Sensing Applications*". ACS Appl. Nano Mater. 2018 doi 10.1021/acsnm.8b00225

2. **Adams, S**., Zhang, J.Z. "*Unique Optical Properties and Applications of Hollow Gold Nanospheres (HGNs)".* Coord. Chem. Rev. 320-321(2016)18
3. Miller, A., **Adams, S**., Zhang, J.Z., Wang, L. *"Study of the Interaction of Citrate-Capped Hollow Gold Nanospheres with Metal Ions".* J. Nanomed. Technol. 7(2016)371
4. Carlson, E., Perez-Abadia, G., **Adams, S**., Zhang, J.Z., Kang, K.A., Maldonado, C. "*A Novel and User-Friendly Technique for Visualization of Intra-Lymphatic Primo Vessels Using Hollow Gold Nanospheres*." J. Acupuncture and Meridian Studies. 8(2015)294
5. **Adams, S**., Thai, D., Mascona, X., Schwartzberg, A.M., Zhang, J.Z. "*Key Factors Affecting the Reproducibility of Synthesis and Growth Mechanism of Near Infrared Absorbing Hollow Gold Nanospheres".* ACS Chem. Mater. 26(2014)6805
6. Lopez-Luke, T., Wheeler, D., de la Rosa, E., **Adams, S**., Zavodivker, L, Zhang, J.Z. "*Synthesis, Characterization and Surface Enhanced Raman Scattering of Hollow Gold-Silica Double Shell Nanostructures"* Biomed. Spectrosc. Imag. 1(2013)679

Chapter One

Unique Optical Properties and Applications of Hollow Gold Nanospheres (HGNs)

1.1 Localized surface plasmon resonance (LSPR) and Mie theory

Localized surface plasmon resonance (LSPR), one of the unique properties associated with noble metal nanoparticles, has been studied extensively.[1-12] When metal nanoparticles are exposed to light on resonance with their absorption wavelength, a collective oscillation of electrons in the conduction band takes place.[13-14] This creates a charge separation with respect to the lattice.[2,15] The confined conduction band electrons in the small particle volume then begin to move in phase with the radiation plane wave excitation, creating a coherent electromagnetic (EM) response which strengthens both the near field energy and the optical extinction associated with the nanoparticle surface.[16,17] The optical extinction, or maximum intensity of the oscillation frequency, is composed of both scattering (elastic and radiative) and absorption (inelastic and non-radiative) efficiencies.[14,17] The coherent oscillatory response of a dipole induced noble metal nanoparticle conduction band electrons on resonance with an indent light at a specific frequency is illustrated schematically in Figure 1.1.

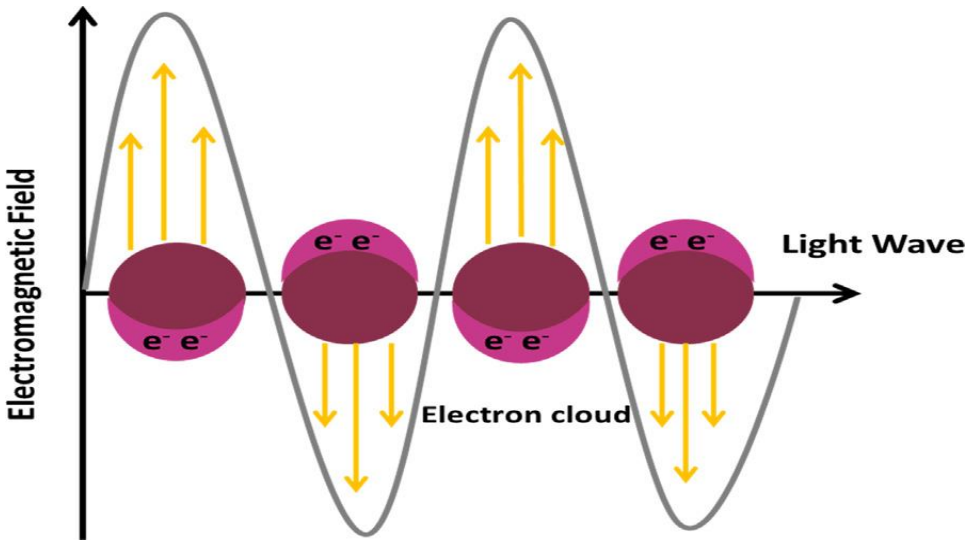

Figure 1.1: The coherent oscillatory response of the dipole induced noble metal nanoparticle conduction band electrons on resonance with incident frequency of light.

The bandwidth, or full width half maximum (FWHM) of the absorption peak is inversely proportional to the coherence time, or periods that the oscillating electrons stay in-phase before damping.[14,18,19] The effective radiative damping of a dipolar plasmon will be proportional to the nanoparticle volume where smaller nanoparticles will have intrinsic, or thermoelastic, damping as their dominant decay mechanism.[9,20] For nanoparticles with diameters greater than 50 nm radiative damping will dominate.[16,21]

Faraday was the first to propose that the brilliant colors observed in gold doped stain glass and colloidal solutions illuminated by visible light were the result of

"finely divided" minute particulates of bulk gold.[22] Later, Mie developed the relationship between light and noble metal nanoparticles, which generates the LSPR.23 Using Maxwell's equations, he modeled the interaction of spherical nanoparticles with a diameter much smaller than that of the resonant incident radiation and determined the scattering of their EM waves in terms of an infinite series of multipolar partial wave contributions.[24,25] Mie established that under these conditions nanoparticles will experience a spatially constant EM field with a time dependent phase known as the quasistatic limit and that the dipolar mode with polarizability α will dominate the LSPR of a spherical metal nanoparticle.[26,27] This polarizability can be defined by:

$$\alpha = 3\varepsilon_0 V\left(\frac{\varepsilon - \varepsilon_m}{\varepsilon_r + 2\varepsilon_m}\right) \qquad (1)$$

where, ε_0 is the vacuum permittivity, V is the particle volume and ε_m is the dielectric constant of the surrounding medium.[1]

According to Mie theory, the extinction cross-section for a given nanoparticle can be determined by Eq. (2) and the absorption contribution can be evaluated with Eq.(3):

$$C_{ext} = \frac{24\pi^2 R^3 {\varepsilon_m}^{3/2}}{\lambda} \frac{\varepsilon_i}{(\varepsilon_r + 2\varepsilon_m)2 + {\varepsilon_i}^2} \qquad (2)$$

$$C_{abs} = \frac{18\pi f {\varepsilon_m}^{3/2}}{\lambda} \frac{\varepsilon_i}{(2\varepsilon_m + \varepsilon_r)^2 + {\varepsilon_i}^2} \qquad (3)$$

where R is the particle radius, λ is the wavelength of light, f is the fraction of the core volume, ε_m is the dielectric constant of the surrounding medium and ε_r and ε_i are the real and imaginary components of the complex dielectric constant of the nanoparticle.[28,29] The scattering contribution can then be calculated by subtracting the absorption coefficient from the total extinction value. Here the real part of the dielectric constant determines the position of the wavelength while the bandwidth, or time spent dephasing, is determined by the imaginary component.[18,30-33] In general, for smaller nanoparticles, <40 nm, the optical extinction is dominated by absorption whereas scattering contributions increase as the diameter of the nanoparticle grows.[21,33,34]

1.2 Metal nanostructures

The use of metal nanostructures in many applications including bio-diagnostics, bio-delivery and photothermal therapies depends almost entirely upon their ability to harvest light and generate strong EM fields. Tuning of the LSPR properties can be achieved through synthesis by exploiting differences in nanoparticle size, geometry, surface morphology, aggregation, aspect ratio and the dielectric constant of the surrounding media.[15,33,35-45] Since each application relies on a specific set of conditions for optimized efficiency, the structural parameters of the nanoparticles employed for use must be tailored accordingly.

In general, overlap between nanoparticles LSPR and the incident wavelength of light should be maximized to ensure the greatest absorption of light and thereby

amplification of the EM field. This can be achieved largely through geometric design.[2,16,17,46-51] While many structures exhibit suitable enhancement of their EM field in response to incident light, their lack of symmetry results in multiple resonances due to non-degenerate electronic transitions.[52,53] This means for a given light wavelength, not all the LSPR transitions will be excited or on resonance.

For example, nanorods have two resonant peaks, a transverse band and another corresponding to the longitudinal mode of the structure.[35,54,55] Aggregates, which are random assemblies of nanoparticles, can have multiple resonances depending on their size and shape, especially when the interaction between particles is strong.[18,53,56,57] This is also true for triangles, stars, cubes and cages.[37,42,46,48,58]

Nanoshells are another type of metal nanostructure with interesting optical properties useful for various applications.[59-63] These structures, which are typically made of spherical silica cores surrounded by a layer of noble metal aggregates, have variation in size, shape and surface morphology due to the random nature of aggregration.[64,65] The polydispersity found within a given ensemble of shells will lead to a broadening of the extinction line width.[66] This results in reduced overlap with incident light and lower efficiency for processes such as photothermal conversion.

Since skin, tissue and blood are most readily penetrated by NIR light, nanoparticles employed in biological applications should have strong absorption in this region.[5,67,68] Structures should ideally be spherical with diameters in the range of 20-100 nm.[69-72] This promotes both optimal cell penetration and bio-clearance.[70,71,73]

Additionally, nanomaterials must be stable to photodegradation, biocompatible and capable of conjugating easily to biomolecules.[53,60,74] However, most commonly used structures lack one or more of these requirements, and their use in many bio-applications still needs to be optimized.

One particularly attractive class of nanoparticles is the hollow gold nanosphere (HGN). HGNs are comprised of a hollow, solvent filled dielectric core and a polycrystalline gold shell.[66,75-77] Both the core width and shell thickness can be tuned through synthesis to produce a range of overall diameters (20-125 nm) and aspect ratios. As a two-interface system HGNs have enhanced LSPR which is the result of strong coupling in the near-field between the plasmon modes of the inner cavity surface and the outer surface.[8,9,29,38] This coupling leads to the hybridization of the two individual plasmon modes where the plasmons interact electrostatically with one another in the same manner as a coupled harmonic osciallator.[8,9] The strength of this coupling is proportional to the aspect ratio of the nanoparticle.[8] As the shell becomes thinner and the aspect ratio increases, the interaction between the cavity and the shell plasmons is amplified producing an enhancement of the EM field associated with the HGNs.

HGNs are also biocompatible, stable to photodegradation and can be easily functionalized for use in bio-targeting and bio-delivery.[53,60,78-80] These particles also possess large surface to volume (S/V) ratios, tunable plasmon resonance, pinholes that act as hot spots to further intensify EM surface energy and, as hollow structures,

are known to be more sensitive to the refractive index of their surroundings than their solid counterparts.[15,66,81-84] Additionally, their scattering and absorption cross-sections can be adjusted through synthesis to maximize efficiency for specific applications, and since the first hyperpolarizabilities (β) of hollow nanoparticles are much larger than those of solid NPs having the same size, HGNs are excellent candidates for any application involving non-linear optics.[85,86]

This chapter will focus on the current understanding of the plasmonic properties of HGNs and their various emerging applications. The synthetic development of HGNs will also be explored with an emphasis on how differences in synthetic parameters results in nanoparticles with various sizes, aspect ratios, surface morphologies and scattering and absorption efficiencies. Additionally, the expanding use of HGNs in a variety of bio-medical applications including photothermal therapies, drug delivery, imaging and sensing will be described.

1.3 Synthesis of hollow gold nanospheres (HGNs)

1.3.1 Amorphous template mediated approaches to synthesis

Early hollow structures were typically made from amorphous materials like ceramics or polymeric substances where the sacrificial core was dissolved out chemically.[87-89] However, dissolvable template mediated approaches typically produce structures that are larger than 100 nm, making them undesirable for most biological applications where particles should be in the 20-100 nm size regime.[72,74,80] Additionally, removal of templates generally involves the introduction of impurities

and adds an additional step in the synthetic process which increases both the difficulty of nanoparticle preparation and the time involved for synthesis.[90-92]

It has been reported that hollow gold nanospheres have been produced in this way.[93-95] In one case HGNs were synthesized by deposition of gold on to a template that was then exposed to tetrahydrofuran as a chemical leaching agent.[94] In another, an Si template that was functionalized with 3-aminopropyltrimethoxysilane (APTMS) to facilitate gold shell deposition was subjected to hydrofluoric acid (HF) etching in order to generate HGNs.[95] Chah et al reported the synthesis of both 50 and 100 μm hollow gold microspheres from dissolvable ceramic hollow sphere templates.[93]

1.3.2 Galvanic replacement

A less complicated approach for synthesizing hollow structures is galvanic replacement. Galvanic replacement is an electrochemical redox reaction where the oxidation of one metal, the sacrificial template, is generated by contact in solution with another metal having a higher reduction potential.[96-99] The template being oxidized, possessing the lower reduction potential and higher rate of diffusion, loses electrons and the metal being reduced gains electrons. Oxidation is initiated on the crystal lattice plane of the sacrificial template exhibiting the highest surface energy.[84,100-102] Small pinholes, or Kirkendall voids, are formed as a result of this oxidation.[103,104] It is the diffusion of the template through an increasing number of voids that generates the hollow structure.[105]

In the mid-20th century, Kirkendall established, in an alloying reaction, using copper and zinc in brass, that atomic diffusion between an interacting atomic pair occurs not through the direct interchange of atoms, but by vacancy exchange generated by the oxidation of one metal.[105] Simple steady state diffusion governed by Fick's first law and the Gibbs-Thomson effect, which states that diffusion is driven by differences in the chemical potential and equilibrium concentrations of interacting atoms, govern the thermodynamics of the reaction.[97,104,106,107]

Recently Goris et al. used high angle annular dark field scanning transmission electron microscopy (HAADF-STEM) tomography to investigate pinhole formation during a galvanic replacement reaction between Ag nanocubes and chloroauric acid ($HAuCl_4$).[102] As gold salt was added to the Ag nanocubes, circular holes appeared on the highest energy [111] plane. Previously Wu et al used TEM to demonstrate the formation of pinholes on the surface of Ag nanocubes involved in a galvanic replacement reaction with $HAuCl_4$ and two of these images can be seen in Figure 1.2.[84] However, Gori's work was the first experimental evidence that pinholes are initiated on only one facet of the crystal lattice and that the reduced metal in a galvanic replacement reaction is deposited first around these pinholes.[102]

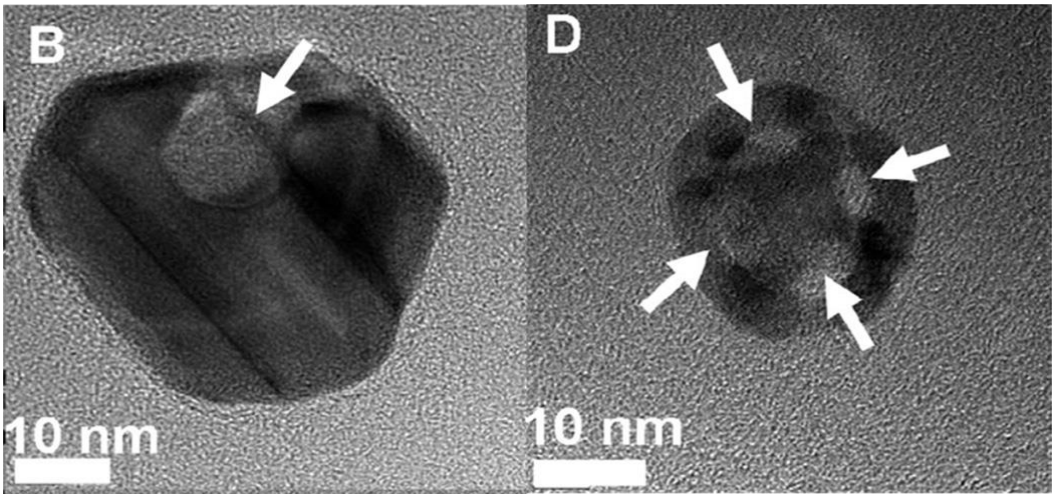

Figure 1.2: TEM images of HGN synthesized after reacting the Ag NPs with (B) 0.75 ml and (D) 1.45 ml of aqueous $HAuCl_4$ solution. The arrow in B indicates the formation of holes on the surface and the hollow nanostructure in the interior. The arrows in D indicate the pinholes and the porous surface.[84]

1.3.3 Tuning the LSPR of HGNs

The first HGN produced through galvanic replacement were synthesized by Xia et al.[108] In this work the authors utilized the fact that the reduction potential of the $AuCl_4^-/Au$ pair is greater than that of the Ag^+/Ag and that silver suspended in solution can be readily oxidized by $HAuCl_4$ to produce a hollow gold nanostructure. The resultant HGNs had a 50 nm diameter, a 6.6 nm shell, an SPR of 634 nm and a full width half maximum (FWHM) of 227 nm.[108]

In 2005 Liang et al also used galvanic replacement to produce HGNs but instead of using silver as a sacrificial template used cobalt ($Co^{2+/}Co^0$ -0.377 V vs. SHE) and gold ($AuCl_4/Au^0$ -0.935 V vs. SHE) as the redox pair.[75] In this case the

facet energies of the hexagonal close packed (HCP) structure of the cobalt template are known to increase 0001<10-10<10-11<11-20<10-12<11-21 with respective energies of 131, 140, 149, 155, 163 (meV/A^2).[109] This means that the oxidation and generation of Kirkendall voids were initiated on the [11-21] plane of the cobalt lattice.

By varying the stoichiometric ratio of $HAuCl_4$ to cobalt, Liang et al was able to red shift the LSPR of the HGNs from ~520 nm, where solid gold absorbs, to ~628 nm.[75] The key to controlling the nucleation and growth of the cobalt template was through the use of excess reducing agent (sodium borohydride), which had been previously reported by Lisiecki et al.[110] The red shift in absorption was attributed to differences in shell thickness which were controlled by the addition of varying stoichiometric ratios of gold to cobalt with smaller additions of gold resulting in thinner shells with enhanced absorption at longer wavelengths.[75]

1.3.4 Tuning LSPR to the NIR

Expanding on the work on Liang et al, Schwartzberg et al used the same redox pair (cobalt and gold) to tune the LSPR of HGNs across the entire visible spectrum and out to the NIR.[66] It was recognized that control of the cobalt sacrificial template diameter was the key to producing larger HGNs with red shifted absorptions. This could be achieved by varying the stoichiometric ratio of the $CoCl_2$ precursor and capping agent as described by Kobayashi et al who reported that as the concentration of the capping agent was reduced, the size of the cobalt nanoparticle diameter

increased.[111] Since the concentration of capping agent not only stabilizes the cobalt nanoparticle seed-mediated growth but also affects the number of nucleations sites generated post-reduction, lower concentrations of capping agent lead to a smaller number of larger seed nuclei being formed.[112] This resulted in cobalt nanoparticles, and therefore HGNs, with larger diameters.[66]

The kinetics related to the addition of the borohydride reducing agent was also investigated.[66] In order to obtain monodispersed particles, it is necessary to increase the nucleation rate so that after the initial nucleation burst no more seeds are formed.[113] When the reduction kinetics were slowed, seeds that formed initially had more time to grow, while those seeds formed later had less time to grow.[66] This resulted in an undesirable polydisperse population. In contrast, increasing the rate at which the reducing agent was added to the reaction precursors resulted in an even reduction of the Co salt and an equal growth period for all the seeds.[66] This enhanced the homogeneity of the size distribution of the ensemble.

The HGN synthetic reaction proceeds according to the following proposed mechanism:[75,114]

$$2CoCl_2+4NaBH_4+9H_2O \rightarrow Co_2B+4NaCl+12.5H_2+3B(OH)_2 \quad (1)$$

$$4Co_2B+3O_2 \rightarrow 8Co+2B_2O3 \quad (2)$$

$$3Co^0+2AuCl_4- \rightarrow 3Co_2++2Au^0+8Cl^- \quad (3)$$

In the first step, a Co_2B species is formed following the reduction of the $CoCl_2$ salt by $NaBH_4$. In the absence of oxygen only this species is formed.[114] However, in the presence of oxygen, the boron atom is oxidized to B_2O_3 as the cobalt atom is reduced to elemental Co (step 2).[114] In the process of reduction, the $NaBH_4$ overcomes an energy barrier through supersaturation and creates a nucleation burst of cobalt seeds.[115] Then through diffusional capture of atoms in solution, seeds coalesce in to primary clusters that then aggregate to form larger spherical particles.[115]

In general, particle growth kinetics are governed by differences in chemical equilibrium at the solid-liquid interface, the total free energy of the nanoparticle (sum of surface free energy and bulk free energy) and by the concentration of reagents available to the growing particle.[113,116,117] In the case of HGNs, there needs to be some oxygen to facilitate the reduction of cobalt salt and growth of cobalt nanoparticles, but if too much oxygen is present the cobalt will oxidize to form cobalt oxide.[114] Once the cobalt template has reached a fixed diameter, galvanic replacement (step 3) is initiated. In this step elemental cobalt is oxidized back to a salt and the $HAuCl_4$ species is reduced to a polycrystalline shell.[66,75]

The LSPR of the HGNs can be tuned by changing the aspect ratio or the ratio between the core and shell diameter. As the aspect ratio increases, the HGNs will absorb longer wavelengths of light.[66,83,118,119] For a fixed core diameter, decreasing the volume of the gold that is delivered produces a thinner shell and red-shifted absorption whereas a constant shell thickness and a decreasing core diameter produce

blue-shifted SPR.[66,83,120,121] Figure 1.3 shows the UV-Vis absorption spectra of nine HGN samples with varying diameters and shell thicknesses. As the ratio of the core diameter to the shell thickness increases the extinction peak red shifts.[6]

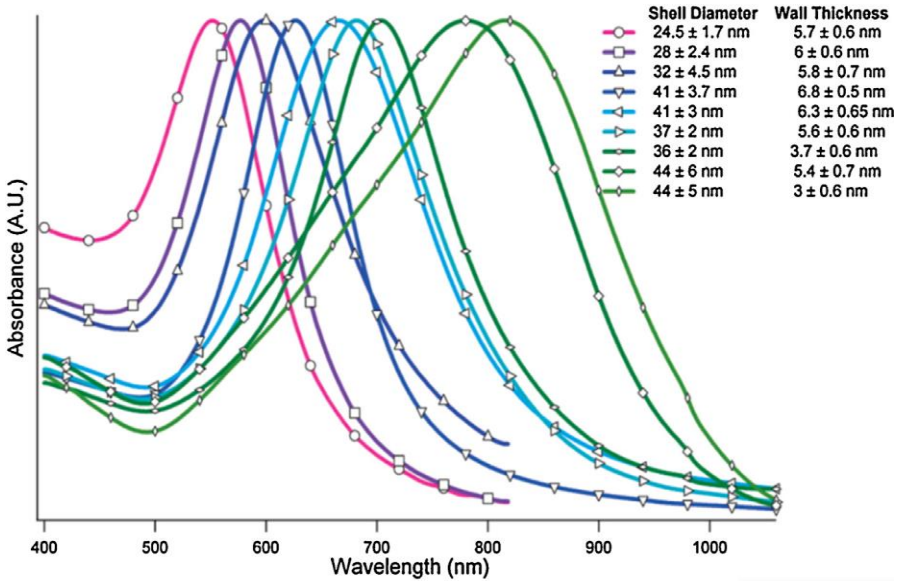

Figure 1.3: UV-Vis absorption spectra of nine HGN samples with varying diameters and shell thicknesses.[66]

1.3.5 Tuning the LSPR with temperature

Another means of tuning the size and LSPR of HGNs is through temperature. Pu and Song et al found that by altering the temperature during the cobalt reduction step, control could be gained over the final template diameter which alters the optical extinction of the resulting HGN. It has been reported previously that HGNs synthesized by an alternative synthetic method have absorption wavelengths that blue

shift as the reaction temperature is increased.[122] Pu and Song et al also observed this trend.[123]

In their work, Pu and Song et al found that as the reaction temperature was raised in ten degree increments from 10 degrees C to 80 degrees C, the overall diameter of the HGN decreased from 150 nm to 30 nm and the SPR was blue shifted from 855 nm to 565 nm. (Pu and Song ref) Figure 4 is a photograph of HGNs synthesized at various temperatures. Lower temperatures produce larger HGNs that scatter more light and appear blue or green, while higher temperatures produce HGns that appear purple or red. It was determined that temperature was directly proportional to the size of the cobalt sacrificial template produced, with higher temperatures producing smaller Co core. This is believed to be the result of the thermodynamic influence on nucleation which is controlled in part through the increase in surface free energy associated with the increase in reaction temperature.[124,125]

1.3.6 Optimizing reproducibility of NIR absorbing HGNs

The ability to tune the SPR of HGNs was significant allowed for their use in a variety of applications like photothermal ablation therapy (PTA), surface enhanced Raman scattering (SERS) and imaging that require nanoparticles with specific colors, sizes and absorption wavelengths. However, the ability to generate NIR absorbing HGNs for biological applications including photothermal therapies still needed to be improved.

1.3.7 NIR reproducibility using poly(vinylpyrrolidone) (PVP)

The first to address enhancing HGN reproducibility in the NIR was Preciado-Flores et al who employed the integration of poly(vinylpyrrolidone) (PVP) during the reduction step to generate large cobalt core diameters with thin Au shells.[76] This strong interaction was determined to be the key in slowing down Au nucleation which resulted in thinner shell diameters, increased aspect ratio and redder wavelengths or absorption.[76]

However, the addition of PVP produced variation in both the core diameter and shell thickness. Additionally, shells had spikey, star-shaped morphologies believed to result from a lack of porosity caused by the presence of PVP which prevent efficient diffusion.[76] It was also observed that the addition of PVP lead to organized backbone like structures in which the gold shell formed preferentially along the traverse axis of the particle chain due to the dense solvating shell of the polymer.[76]

These structures showed broadening of the total extinction indicative of a polydispersed ensemble.[56] While these morphologies and extended spatial arrangements may benefit an application like SERS, where aggregation and particle alignment generate hot spots which enhance scattering, a more monodispersed population is desired for applications like photothermal therapies tht require enhanced resonance with incident laser light for greater efficiency of heat generation and transfer.[126]

1.3.8 Non-polymer NIR reproducibility

Another effort focused on improving the synthetic reproducibility of NIR absorbing HGNs will be detailed in chapter 2.[77] Chapter 2 will describe the emphasis placed on not only gaining control of the cobalt NP growth in order to maximize the size of the template but also on separating the nucleation and growth phases of the growing Co NPs. This was achieved by optimizing reagent concentrations and evaluating the kinetics of the cobalt nanoparticle growth.[77] Figure 1.4 shows electron microscopy images of HGNs synthesized with and without polymers. It can be seen that HGNs synthesized with PVP produce spikey, uneven surface morphologies and align themselves in chain like formations while HGNs prepared without the addition of polymers are more uniform in size and exhibit smooth surface morphologies.[77]

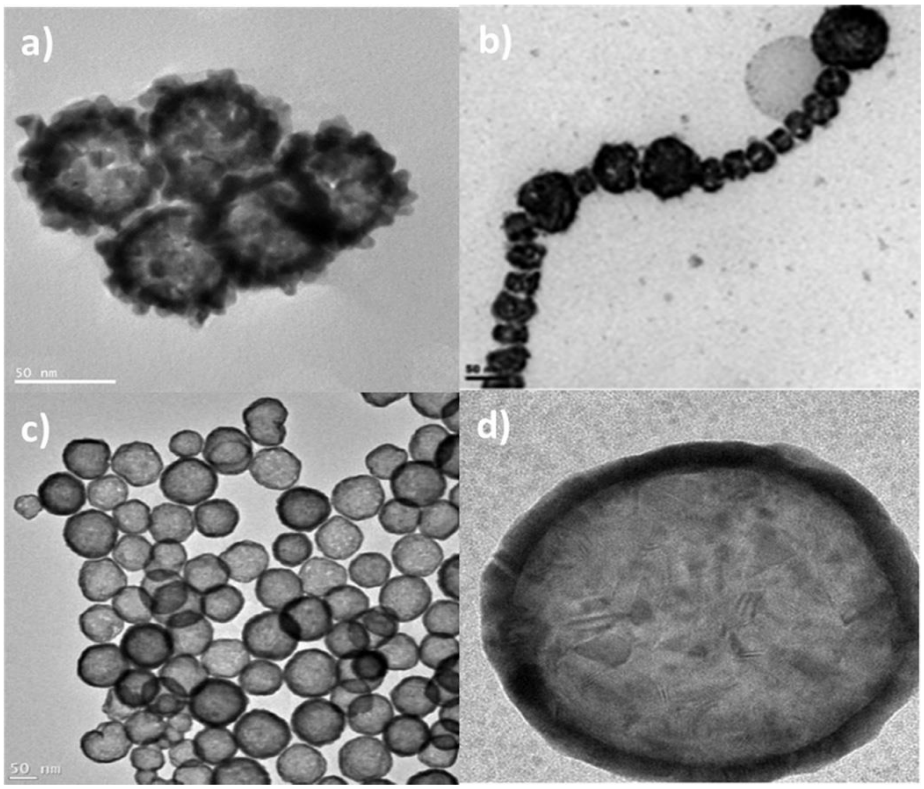

Figure 1.4: HGNs synthesized with PVP produce: (a) spikey star shaped surface morphologies[77] and (b) backbone like chain structures.[77] HGNs synthesized in the absence of polymers are: (c) more homogeneous with respect to size and surface morphology and (d) have smoother and more uniform shells. [(c) and (d) unpublished Adams/Zhang 2015]

1.4 Surface enhanced Raman scattering (SERS) and electromagnetic (EM) field enhancement

1.4.1 Plasmon coupling in aggregates for SERS

Since its discovery in the late seventies SERS, which relies on a roughened noble metal substrate to enhance the sensitivity of Raman detection, has become a powerful tool in the early identification and diagnosis of disease.[129-139] The highly localized EM field of the metal, due to LSPR, is known to enhance the Raman signal by 5-10 orders of magnitude.[140-143] Aggregation of metal nanoparticles can also be employed to produce significant SERS enhancement through the generation of hot spots which result from EM coupling between particles in near field proximity to one another.[56,64,144-146]

The most common substrate used in SERS applications is Ag.[147-151] However, Ag is considered unstable, degrades in vivo and is typically synthesized with cetrimonium bromide (CTAB) which is considered cytotoxic.[152-154] Additionally, it has been demonstrated that the peak intensity ratios of the Raman signal change

significantly when silver aggregates are used leading to inconsistent results and poor reproducibility.[143,155-157]

It has been reported that HGNs show improved SERS activity when compared to Ag aggregates.[157-159] When Schwartzberg et al compared HGNs to silver aggregates, the Rayleigh scattering intensity of HGNs showed nearly a 10-fold improvement over Ag.[158] Figure 1.5 shows the SERS intensity spectra for both HGNs and Ag aggregates bound to the Raman reporter molecule 4-mercaptobenzoic acid (MBA). There is significant signal enhancement for the HGNs. Furthermore, all the peak intensity ratios for the HGNs fall within 0.9-1.1.[158] This represents a statistical distribution of 5%. In contrast, the Ag NPs exhibit a 45% statistical distribution (0.5-1.7) with respect to consistency. This inconsistency is due to the randomness of aggregation which, depending on size and shape, will produce variation in the EM field associated with the ensemble.[64-65,158, 160-161]

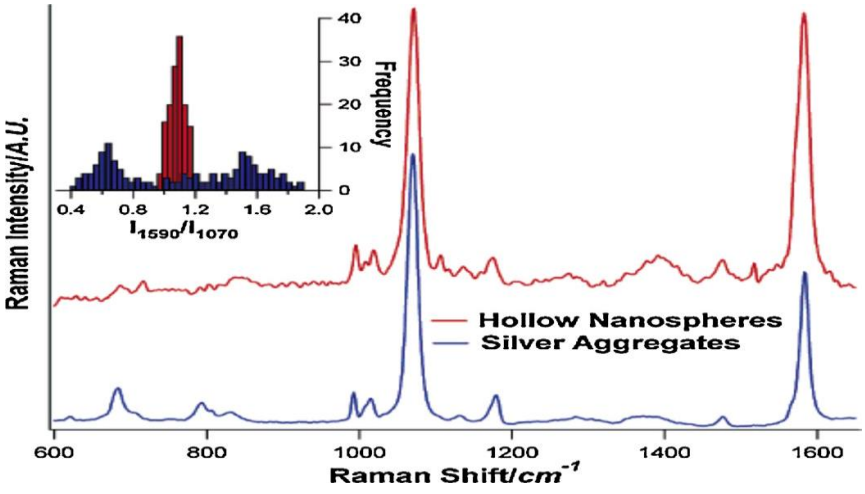

Figure 1.5: Single particle SERS spectrum comparing HGNs (red top trace) and Ag aggregates (blue bottom trace). The inset is a histogram o the relative intensity of the two most prominent peaks of the Raman reporter molecule 4-mercaptobenzoic acid (MBA) at 1070 and 1590 cm-1 of 150 HGNs (red bars) and 150 silver aggregates (blue bars).[158]

Lee et al also found that antibody conjugated HGNs targeting the HER2 breast cancer marker over-expressed in MCF7 cells had much better homogeneous scattering properties with more consistent intensity ratios than bioconjugated Ag aggregates targeting the same cells.[157] For HGNs the intensity ratios ranged from 0.8 to 1.4 compared to 0.9 to 3.1 for Ag. Both Schwartzberg and Lee attribute the enhancement of the Raman signal and consistency of intensity ratios to the uniform structure and narrow plasmon dispersity of HGNs.[157-158]

1.4.2 Plasmon coupling in aggregates for SERS

In order to optimize HGN use in SERS based applications it is critical to understand the effect of their structure, size and aggregation on EM field enhancement. In general, aggregation intensifies the second harmonic generation of HGNs in contact with one another, effectively combining their collective energy to generate new photons with twice the frequency and half the wavelength.[161-164] HGN aggregates are also known to exhibit both hybridized plasmon modes, which are the result of surface plasmon interactions with cavity plasmon modes, and collective charge transfer resonances.[165-167] However, even when not in direct contact with one

another there is an intensification of the dipole charge at the interparticle gap of nanoparticle aggregates in near field proximity.[8,168-170] For example, Xu et al observed that the junction between two nanoparticles 1 nm apart exhibited an EM field enhancement of 10^{10} compared to an individual particle.[171] The charge transfer between two HGNs in a dimer interacting with an EM field polarized parallel to the interparticle axis is shown in Figure 1.6. It can be seen that the two surfaces in contact with each other are polarized with opposite signs which contributes to the enhancement of charge-transfer between particles.[172]

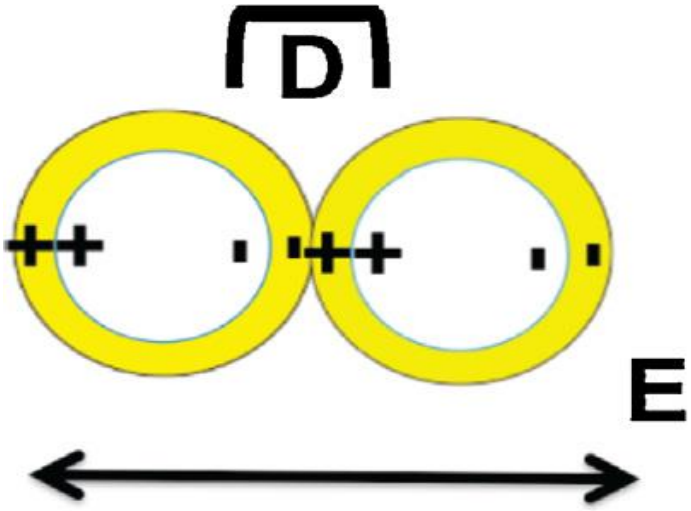

Figure 1.6: Schematic representation of stable charge-transfer plasmon configuration between a contact dimer. The incident EM field is polarized parallel to interparticle axis of the two HGNs. The combined interfacial shell thickness is given by D.[172]

Chandra et al used thiol mediated aggregation to study the experimental impact of aspect ratio (3.5-11.7) on the plasmonic response of HGNs.[172] Aggregation intitiated with ethanedithiol produced contact dimers with substantially blue-shifted

SPR, while those treated with cysteine produced large extended structures of spatially separated dimers having interparticle gaps ≥1 nm and red shifted SPR. While the authors found no direct correlation between aspect ratio and plasmonic response, they observed a trend correlating shell thickness and SPR shift.

As shell thickness decreased for contact dimers generated by ethanedithiol, the change in absorption shifted to shorter wavelengths.[172] This blue shift is believed to be the result of delocalized electrons confined within the cluster and the interactions of antibonding or higher energy HGN modes.[173] However, for contact dimers with shells ≥7 nm, no significant spectral shift was reported.[172] In comparison all cysteine induced aggregates with interparticle gaps ≥1 nm showed red shifted absorption regardless of shell thickness. The red shifted SPR is attributed to the generation of symmetric coupling of the bonding modes between the surface SPR and the inner cavity plasmon modes which lowers the energy of the symmetric modes of the dimer.[170,174]

Xie et al reported that HGNs with thicker shells, which have enhanced scattering cross-sections, generated greater SERS intensity whether they were on resonance or aggregated.[44] This is because thicker shelled HGNs are known to bear the majority of their EM field concentration at the conical region of the particles interface while thinner shelled HGNs have significant energy centered at their cavity walls.[172]

1.4.3 First hyperpolarizabilities (β)

Raman scattering results from the induced dipole oscillations in a material as it interacts with an applied EM field. The greater the propensity of a molecule to generate a dipole, the more intense the plasmonic oscillations will be and the larger the signal enhancement.[137] For this reason, evaluating the first hyperpolarizability (β) of a nanostructure is useful since β, which is a measure of how easily a dipole is induced in a molecule in the presence of an electric field, is correlated with Raman signal intensity.[175]

When HGNs of different sizes were compared to solid Au using two-photon Rayleigh scattering (TPRS) to measure their 1st hyperpolarizabilities it was found that the β values of the HGNs greatly exceeded those of the solid NPs.[176-177] HGNs with overall diameters of ~30 and ~78 nm and shell ~8 and ~11 nm had β values of 5.4 X10^5 (x10^{-30} esu), 6.3X10^5(x10^{-30} esu)while 20 nm solid Au NPs showed a β value of 2.4X10^5(x10^{-30} esu).[177] This is not surprising since β is known to scale linearly with surface area.[175] For comparison, the first hyperpolarizability of an HGN with ~80 nm diameter is 3 times that of a solid Au nanoparticle of the same size and ~1.5 times that of a solid Au nanoparticle with a 30 nm diameter.[86,178]

1.5 Imaging

Non-invasive biological imaging has been used for decades to accurately visualize structures *in vivo* and to diagnose and help treat disease.[67,96.179-184] Common techniques include near infrared fluorescence (NIRF), positron emission tomography (PET), optical acoustic tomography (OAT), photo acoustic tomography (PAT) and

magnetic resonance imaging (MRI).[183,185-188] Typically QDs, fluorescent dyes and iodinated agents are used as contrast agents and some methods call for the use of radioactive isotopes.[188-194] Unfortunately, each of these agents has its own drawbacks when used in biological applications.

QDs and dyes have issues related to biological incompatibility and lack of stability to photodegradation.[187,195-196] Additionally, QDs have been shown to remain in major organs for months after injection producing immunogenic reactions in vivo.[197-200] Iodinated agents are also less than ideal because of their biological toxicity and short circulation time in vivo.[201-203] For example, Kim *et al*. reported that when Ultravist, an iodine based contrast agent, was used in a rat model the circulation time was less than 10 minutes compared to that of 30 nm spherical Au nanoparticles which circulated in vivo for over 4 hours.[201]

Gold nanostructures are often used to overcome the limitations found with standard contrast agents.[204-207] In addition to their biocompatibility, Au nanoparticles have longer *in vivo* circulation times during the imaging process and in some cases are faster. Additionally, since the atomic number of Au is higher than that of iodine, Au nanostructures have higher absorption efficiencies which means that in vivo contrast will be enhanced. [201,209,211]

HGNs are a natural extension of Au nanoparticles used in imaging. As noble metal structures, they have enhanced EM field strength because of their plasmon resonance, and surfaces can be easily functionalized to target bio-molecules. They are

also resistant to photobleaching and have molar extinction coefficients (ε) that are larger than those of dyes and QDS.[177,212-213] For instance, Lu *et al*. recently reported that a 40 nm HGN with a 2-3 nm shell and an SPR of 800 nm has a molar absorption coefficient of $1.4X10^{11}$ M^{-1} cm^{-1}.[212] In comparison, fluorophores have ε in the range of $5.0X10^{3}$ to $2.0X10^{5}$ M^{-1} cm^{-1} and QDs have molar absorption coefficients ~$1X10^{5}$ M^{-1} cm^{-1} making both far less effective as contrasting agents. [214-216]

Photoacoustic imaging is a hybridized technique combining non-ionizing radiation and ultrasonic detection.[161,217-219] The photoacoustic signal is considered inherently weak due to the low intrinsic absorption of oxyhemoglobin and deoxyhemoglobin in the NIR.[212,220-222] However, high spatial resolution and enhanced sensitivity were found to accompany the use of HAuNS in the PAT experiment reported by Lu *et al*.[212] In this work, the authors conjugated thiolated PEG to the surface of NIR absorbing HAuNS and used them to image living mouse brain vascular.[212] One half of the mice subjects were injected with PEG-HAuNs and the other half with saline. The researchers were able to visualize brain blood vessels as small as ~100 μm for up to 2 hours post injection in the mice that had been treated with PEG-HAuNS at concentrations as low as ~20 pM.[212] Furthermore when the researchers compared the photoacoustic brightness of HGNs to other common imaging agents, it can be seen in figure 1.7 that the use of HGNs produced significant optical enhancement.

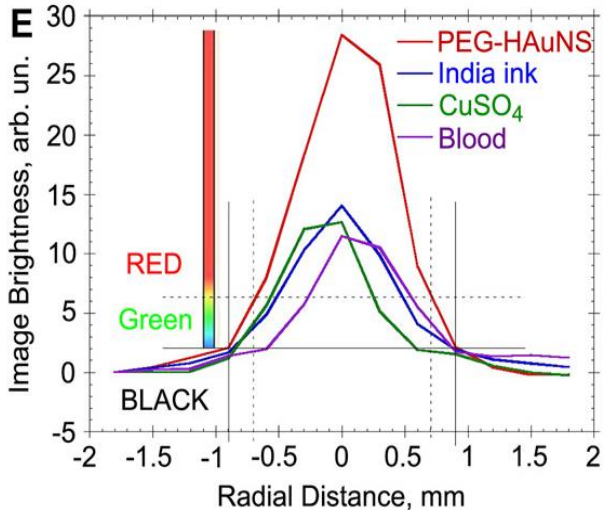

Figure 1.7: Quantitative analysis of photoacoustic image brightness through cross section of blood (O.D. 1.6), $CuSO_4$ (O.D. 2.0), India ink (O.D. 0.8) and PEG-HAuNS (O.D. 0.7).[212]

Hollow gold nanospheres have also been used instead of dyes to image the Primo Vascular system in a rat model. This work will be discussed in detail in chapter 3.

1.6 Conclusion

Over the last decade, significant advancements have been made in understanding how the plasmonic response of HGNs can be tuned through synthesis to produce particles that are useful for a wide variety of applications including bio-diagnostics, bio-delivery and photothermal therapies. The study of plasmon coupling, collective charge transfer and the EM enhancement associated with aggregation, pinhole generation, surface morphology, size and aspect ratio have demonstrated that

HGNs exhibit a number of interesting plasmonic properties. However, many outstanding issues remain to be addressed including gaining a better understanding of the intricate interaction between HGNs and cells as well as bio-accumulation and bio-clearance *in vivo*. While there has been some progress made in determining the ideal size and aspect ratio for optimal photothermal energy conversion, further research is clearly needed for a more complete understanding and full optimization.

Chapter Two

Key Factors Affecting the Reproducibility of Synthesis and Growth Mechanism of Near Infrared Absorbing Hollow Gold Nanospheres

2.1 Introduction

Noble metal nanoparticles are of great interest for the therapeutic treatment of cancer via photothermal ablation (PTA) therapy due to their small size and strong optical absorption.[223-233] In PTA metal nanoparticles attached to cancerous cells are resonantly illuminated by light causing rapid particle heating, modifying the local cellular temperature significantly, and inducing cell death.[234-241] Both cellular uptake and photothermal conversion are dependent on nanoparticle size and shape, with spherical nanostructures demonstrating the best performance to date.[242-245] To generate highly efficient PTA candidate structures, it is important to take into account surface plasmon resonance (SPR) wavelength, which is largely determined by particle shape and, to a lesser degree, size.[246] Particle size and shape also determine biological interaction, and therefore place a limitation on the type of structures that can be used.[242-245,247-250]

Solid spherical gold nanoparticles are of the correct form factor for optimal PTA use, however, the maximum SPR absorption lies between 520 - 540 nm depending on size (10 nm – 40 nm).[223,251] This minimal variation in wavelength limits

their application in PTA where it is desirable to work in the region of 690-900 nm due to the high optical transmission of blood and tissue in this region.[225-226,246,252]

Although aggregated plasmonic particles present a significant red shift in SPR from their spherical constituents, making them spectrally ideal in ensemble for PTA, individually they lack spectral homogeneity and are generally too large to be effective.[253-255] Nanorods are another interesting system with broad NIR absorbance, however, they are highly polarization sensitive, reducing absorption efficiency.[242,256]

Hollow gold nanospheres (HGNs) have emerged as an excellent candidate for cancer imaging and therapy.[251,256-265] Their native surface chemistry is simple and can be easily functionalized for subsequent bioconjugation to target receptors in cancer cells. Formed through a galvanic replacement reaction between sacrificial cobalt templates and gold ions, HGNs are highly uniform structures that can be tuned from the visible to the NIR.[223,233,266] Their shape ensures ease of cell penetration, due to spherical symmetry and uniform cellular interaction regardless of orientation. HGNs also have a single homogeneously broadened SPR which can be tuned to resonance with the excitation source, and will provide strong absorbance for every particle in the system. In addition, the thin shell diameter facilitates rapid electron-phonon coupling, allowing for more efficient conversion of absorbed photons to heat than solid gold particles.[267-268]

As discussed in chapter one our laboratory previously reported the synthesis of HGNs which could be tuned from the visible to the NIR.[66] However, the synthesis of

NIR absorbing particles was unstable and produced particles of low homogeneity. Subsequently, we reported a more reproducible method for the synthesis of NIR absorbing HGNs based upon the use of Co nanoparticles prepared in the presence of poly(vinylpyrrolidone) (PVP).[269] PVP was used to successfully passivate the unstable cobalt particles during the hydrolysis step of the synthesis, allowing for the generation of larger NIR absorbing particles. However, the presence of PVP introduced additional problems. First, HGNs prepared with PVP exhibit larger variations in core diameter and shell thickness. Second, they tend to form organized structures, including back-bone like chains in which the gold shell forms preferentially along the traverse axis of the particle chain. Both of these problems were associated with a significant and undesirable broadening of the SPR absorption spectrum. Additionally, it has been shown in preliminary studies that the use of PVP results in HGNs with decreased binding affinity for PEGylated linkers used to conjugate antibodies, which in turn reduces the number of HGNs that can effectively target specific receptors.

In this chapter we present a modified HGN synthesis that produces more stable and homogeneous particles with higher reproducibility NIR absorbance than those previously reported.[228,266,270] Importantly, the high reproducibility is achieved without using a polymer. We have found that it is possible to separate cobalt seed formation from stabilization by initiating the reaction with lower concentrations of sodium citrate. This ensures that fewer and larger seed particles will be formed when the cobalt salt is reduced by borohydride. The reduction of sodium borohydride

concentration in the synthesis, and the addition of citric acid, significantly shorten the hydrolysis reaction time and reduce the potential for particle oxidation, which compromises the integrity of the cobalt sacrificial templates used to form HGNs. This synthetic advance has led to the discovery of a greatly extended growth time for the cobalt template particles. The results help to shed new light on the mechanism of Co seed as well as HGN growth.

2.2 Experimental

2.2.1 Materials

Cobalt chloride hexahydrate (99.99%), trisodium citrate dehydrate (>99%), sodium borohydride (99%), citric acid (99%) and chloroauric acid trihydrate (ACS reagent grade), were obtained from Fisher Scientific. All water used in the syntheses was 18 MΩ milli-Q filtered.

2.2.2 Cobalt Nanoparticle Synthesis and Gold Shell Growth

All glassware was cleaned with aqua regia and rinsed with high purity water prior to use to eliminate adsorbents. The cobalt particle synthesis was performed on a Schlenck line. 100 µl of aqueous 0.4 M cobalt chloride ($CoCl_2$) and 100 µl of 0.1 M aqueous sodium citrate were added to 100 ml of water in a double neck round bottom flask. The clear solution was pumped down for 5 minutes then exposed to N_2 to deoxygenate the solution. After ~2 minutes under N_2 gas, 400 µl of freshly prepared 0.25 M sodium borohydride ($NaBH_4$) was added to the solution. The round bottom

flask was then swirled by hand until the color changed from clear to brown to gray, indicating the reduction of Co^{2+} ions in solution to Co^{0} nanoparticles. 175 µl of 0.1 M aqueous citric acid was then injected and the solution swirled for a few seconds to increase the rate of sodium borohydride hydrolysis and to prevent aggregation. After 10 minutes of growth, 30 ml of cobalt template solution was quickly added to 10 ml of water containing 20 µl of 0.1 M aqueous chloroauric acid ($HAuCl_4$) solution and swirled rapidly. After an immediate, slight color change from gray to blue-gray, the particles are exposed to air and swirled until the color change is complete to purple, blue, or green, depending on particle parameters. The gold shell forms within seconds onto the cobalt particle. If there is stoichiometrically less gold than cobalt a cobalt seed particle will remain within the gold shell. Upon exposure to oxygen, this cobalt core oxidizes and dissolves, revealing the true color of the HGN solution.

2.2.3 Characterization of HGNs

High-resolution transmission electron microscopy (HRTEM) was performed using a FEI Titan 80-300 with accelerating voltage set to 300 kV. EM characterization was performed on FEI F20 UT Tecnai HRTEM/STEM operated at 200 kV accelerating voltage located at National Center for electron Microscopy (NCEM) at Lawrence Berkeley National Laboratory. Low resolution electron microscopy was performed on an FEI Quanta 3-D dual bean microscope with accelerating voltages of 5.00 kV and 30.00 kV at the Keck Center in the Electrical Engineering Department of the University of California Santa Cruz.

2.3 Results

2.3.1 Effect of growth parameters on HGN SPR properties

Figure 2.1a shows electronic absorption spectra of HGNs formed using the slow and fast addition of the cobalt nanoparticle solution to the gold salt solution. The slow addition was performed using a cannula and resulted in a nearly dropwise addition. In the fast method, the cobalt solution was poured into a secondary container where it could be rapidly added to the gold solution with manual stirring. The spectrum associated with the slow addition is centered ~640 nm and has a FWHM (full width at half maximum) of 675 meV. The spectrum of the HGNs prepared by the fast addition exhibits an SPR at ~ 790 nm with a FWHM of 443 meV. Slow addition resulted in both a broadening of the SPR and a spectral blue shift. This reflects the non-uniform mixing of the cobalt and gold solutions where some cobalt particles were in regions of higher gold concentration and form thicker shells, while other cobalt particles were in regions of low gold concentration and form thinner shells. Because the reaction of the cobalt particles with gold salt was extremely rapid the two solutions must mix at a similarly high rate in order to produce HGNs with homogeneous shell diameters.

Figure 2.1b shows the result of modifying the ratio of cobalt chloride to sodium citrate. Previously, we had shown that sodium citrate and sodium borohydride could be used as a primary means of controlling the size of the cobalt nanoparticles. To produce HGNs with strong SPR in the NIR, larger diameters (>40 nm) are required.[266] Modifying the cobalt chloride:sodium citrate molar ratio between 1:1 and

1:4, we were able to generate particles with SPR at 650 nm (FWHM – 306 meV, 1:1), 725 nm (FWHM – 520 meV, 1:2), and 800 nm (FWHM – 557 meV, 1:4).

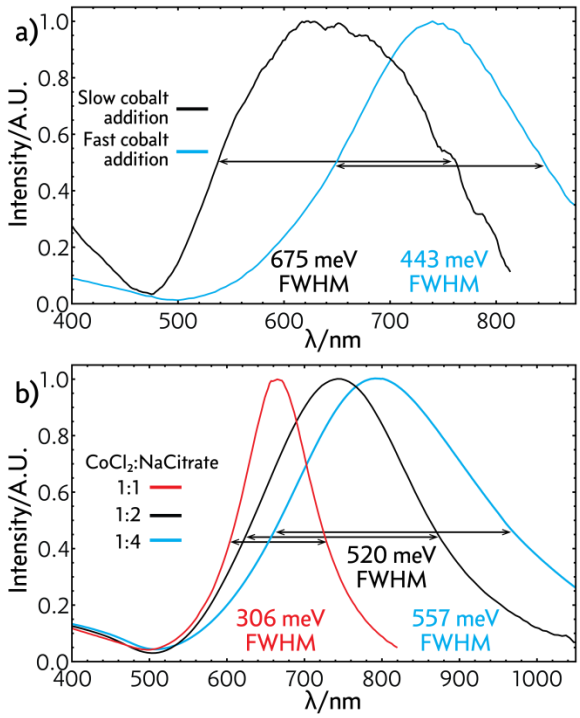

Figure 2.1: Absorption spectra of HGNs prepared (a) by adding and mixing the Co nanoparticles to the $HAuCl_4$ solution by slow (black curve) and fast addition (blue curve), and (b) with varying ratios of CoCl2:NaCitrate (1:1 - red, 1:2 – black and 1:4 - blue).

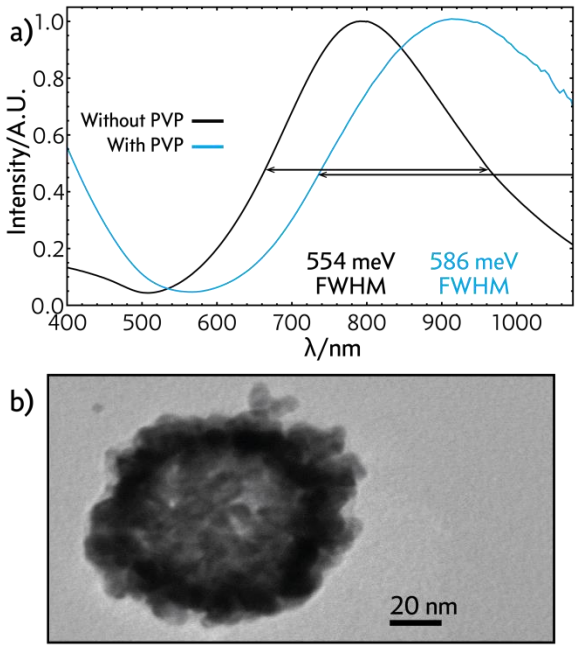

Figure 2.2: (a) Absorption spectra of HGNs prepared with (blue) and without PVP (black), and (b) TEM image of HGN prepared with PVP.

2.3.2 Effect of PVP on Co nanoparticles used as templates for gold shell growth

To examine the effect of PVP on the HGN synthesis, cobalt nanoparticles were prepared by borohydride reduction with and without PVP. Representative absorption spectra are shown in Figure 2.2a. Both samples show strong SPR in the NIR, however, those prepared with PVP are significantly red-shifted (peak at approximately 910 nm vs 795 nm). When PVP was used, there is significant broadening of the SPR FWHM.

Figure 2.2b shows a representative TEM image of an HGN prepared with PVP. The gold shell is non-uniform, reflecting a star-shaped patchwork-like formation of the gold layer. This irregular surface morphology and lack of core diameter and shell

thickness homogeneity is responsible for the observed broadening of the SPR spectrum. It is not clear why such particles show such a strong red shift as compared to the more homogeneous ones, however, the convoluted gold structure and nanoporous nature may be responsible, i.e. reminiscent of strong aggregates of gold nanoparticles that tend to have NIR SPR.[271]

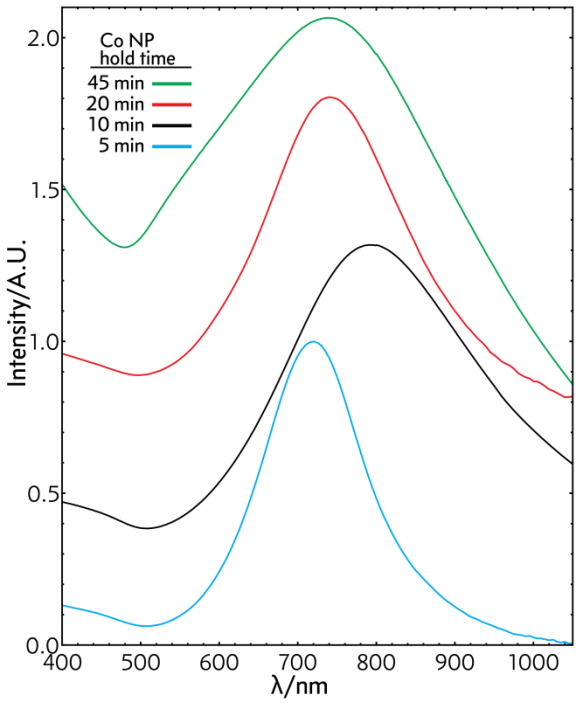

Figure 2.3: Absorption spectra of HGN solutions formed after various wait times after borohydride addition: 45 min (green), 20 min (red), 10 min (black) and 5 min (blue). Spectra are baseline shifted for clarity.

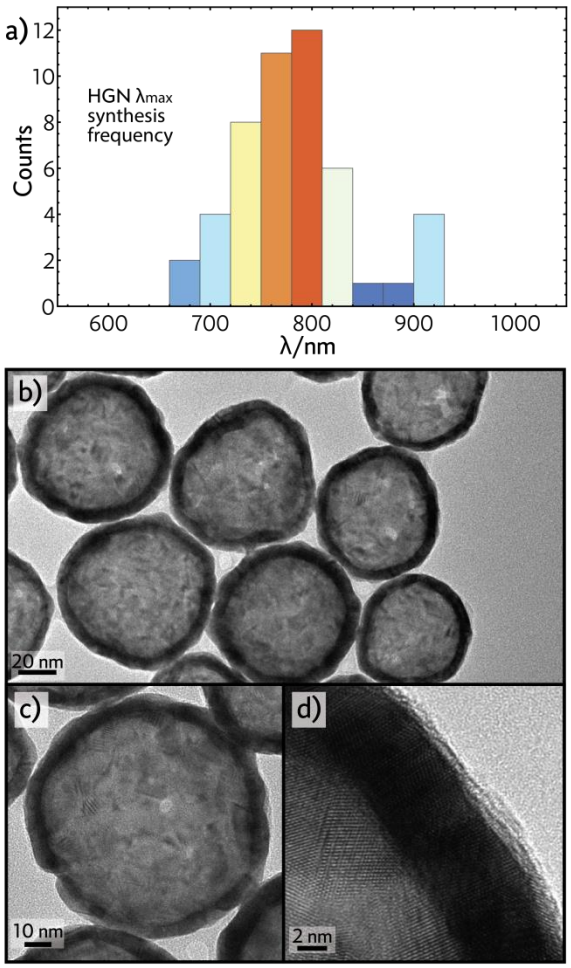

Figure 2.4: (a) histogram showing central HGN absorption wavelength (λ_{max}) for fifty syntheses; (b) (c) and (d) HRTEM images of HGNs at various magnifications.

2.3.3 Effect of hydrolysis and growth time on SPR

We next investigate the optimal growth time of Co nanoparticles using fast addition. In earlier studies, there was a 45 minute delay between cobalt particle formation, and the addition of gold to allow for complete hydrolysis of the sodium borohydride. Having determined that we could significantly reduce this waiting

period by decreasing the concentration of sodium borohydride and adding citric acid to increase the hydrolysis rate, we carried out a time-course study to determine the optimal incubation period.

Figure 2.3 shows the absorption spectra of four syntheses with different reaction times following the addition of borohydride to the cobalt-citrate solution, but before the addition of gold to the cobalt nanoparticles. HGNs prepared after reaction times of 5, 10, 20 and 45 minutes generated SPR absorption maxima (and spectral widths) at 730 nm (FWHM – 143 meV), 800 nm (FWHM 266 – meV), 760 nm (FWHM – 186 meV), and 760 nm (FWHM – 338 meV) respectively.

To determine synthetic reproducibility, the HGN synthesis was carried out fifty times by the fast addition method using Co nanoparticles that reacted for 10 minutes at a cobalt chloride:sodium citrate molar ratio of 1:4. Figure 4a shows a histogram of these results as counts versus the maximum SPR absorption (λ_{max}). A high percentage of the HGNs generated by this optimized synthesis are clustered around 800 nm, which is the desired wavelength.

Figure 2.4 b-d show representative HRTEM images at different magnifications of HGNs prepared under optimized conditions. These HGNs exhibit a uniform appearance with respect to both their core diameter (64.1 nm ± 6.4 nm) and shell thickness (6.4 nm ± 0.58).

2.4 Discussion

The primary goal of this investigation was to make highly reproducible HGN's that absorb consistently in the NIR without the addition of polymers like PVP that can hinder applications like PTA. We reasoned that although PVP was effective in stabilizing Co nanoparticles during growth, that it might lack the porosity necessary for efficient diffusion of the gold and cobalt ions underlying the galvanic replacement process. This interference with oxidation and reduction prevents the formation of homogeneous spheres with uniform core diameters and shell thickness. It has been shown in this work (Figure 2.2b) that the integration of PVP during synthesis results in irregular, spikey, HGNs. Furthermore, HGNs prepared with PVP demonstrate a broadening of the absorption SPR. Both the star shaped morphology, which produces multiple resonances, and the broadened FWHM, which indicates a wide distribution of sizes within the population and/or aggregation, result in a smaller percentage of the ensemble being on resonance with the excitation wavelength used in PTA therapy and will diminish conversion to heat. We therefore, undertook a careful and systematic examination of the conditions involving the preparation of cobalt nanoparticles in the absence of PVP to see if we could achieve reproducible, homogeneous HGNs with SPR in the NIR having a more uniform core and shell.

One of the key findings demonstrated in our study is that it is possible to significantly shorten the reaction time between the borohydride reduction step and the galvanic replacement. This is essential because even after deoxygenation, the cobalt nanoparticles will oxidize from water contact over time, resulting in poorly formed HGNs. It is known that some oxygen is necessary for good cobalt particle formation,

but that the presence of too much oxygen causes the particles to degrade or form cobalt oxide.[266]

A critical step in the formation of HGNs is the elimination of any remaining sodium borohydride prior to the addition of the gold salt. Initial work.[266] used a higher concentration of borohydride for reduction and therefore required 45 minutes, or longer, for this step. Since extended exposure to water results in oxidation of cobalt, the synthesis was difficult to control and particle stability was compromised leading to a lack of homogeneity, which is reflected as a broadening of the absorbance FWHM. To increase the rate of hydrolysis, a decreased borohydride concentration was used and citric acid was added post reduction to both increase the borohydride hydrolysis rate and prevent aggregation. It was found that the cobalt reaction step could be reduced to as short as 5 minutes, but that cobalt growth was not complete until 10 minutes. HGNs formed after 10 minutes of reaction have narrow line widths, which have previously[272] been shown to be consistent with a homogeneous ensemble, can be produced.

The process of nucleation and growth, while two distinct and separate events in the formation of Co nanoparticles, are interconnected. Sodium citrate is believed to control the growth of the nascent cobalt nanotemplate by acting as a capping agent, and stabilizer. It is also correlated with the optimization of the nucleation sites available for particle growth once the reducing agent, sodium borohydride, is added.[273] For this reason, the ratio of cobalt chloride to sodium citrate must be carefully controlled. High citrate concentrations will generate a larger number of

cobalt seeds, resulting in smaller cobalt particles, while low citrate concentrations will generate unstable particles which tend toward aggregation. We have found that it is possible to separate the process of cobalt seed formation from particle stability by decreasing the concentration of sodium citrate added prior to borohydride reduction and by adding an aliquot of citric acid afterwards. This reduction in sodium citrate concentration leads to the synthesis of more uniform, large cobalt nanoparticles that generate HGNs with SPR in the NIR and that have larger core diameters and thinner gold shells.[231]

Another factor influencing the uniformity of shell thickness was the manner in which the cobalt and gold solutions were mixed together. Previous work employed the use of a cannula which transferred the cobalt nanoparticles to the gold ions at a sluggish rate resulting in inconsistent mixing.[269] Since only a portion of the cobalt was in contact with the gold ions initially, they were exposed to a higher concentration of gold. This produced HGNs with thicker gold shells. The cobalt nanoparticles that came out of the cannula later were exposed to lower gold concentrations and had thinner shells. This variation in shell thickness was observed as an unwanted broadening of the FWHM, indicative of polydispersity within the sample. By implementing a fast addition, which relied on transferring the cobalt to a secondary container, and then quickly combining the two solutions and mixing manually, we could ensure that all the Co nanoparticles were in immediate contact with the $HAuCl_4$ solution. The resulting particles maintained SPR with narrow line width indicating homogeneity of both core and shell diameters.

We have shown here that the cobalt reaction time has a strong effect on the resulting HGN optical properties (Figure 2.3). The initial red shift in HGN absorbance between 5 and 10 minutes of reaction time is likely due to further cobalt particle growth during this period. This is an interesting result in itself as previous reports of this cobalt synthesis[273] have considered the reaction complete within one minute, however, it is clear from this result that particle growth is not complete for over 5 minutes after the addition of the reductant. This may explain some of the difficultly in preparing reproducible HGNs. Cobalt nanoparticles that reacted for more than ten minutes show a blue shift in absorption. We believe this may be due to the oxidation and etching of the cobalt surface but further studies will need to be employed to provide evidence to support this hypothesis.

The fabrication of HGNs from Co nanoparticles is a highly complex process that is only beginning to be understood. Figure 2.5 illustrates the proposed reactions leading to the formation of HGNs. In the first step, Co_2B is the primary product that results from the addition of $NaBH_4$ to the cobalt chloride/sodium citrate solution (Equation 1). $NaBH_4$ is a strong reducing agent that surmounts an energy barrier through supersaturation to create a nucleation burst of the cobalt seed particles. These seeds are then able to grow into nano-sized clusters by diffusional capture of atoms in solution. Primary clusters are formed following aggregation of these nano-sized clusters, leading to large spherical particles. This process critically depends upon dissolved oxygen. In the absence of oxygen only Co_2B is produced upon reduction, while in the presence of oxygen, the boron atom is oxidized to B_2O_3, with the

simultaneous reduction of the cobalt atom to elemental Co solid (Equation 2).[274] The level of oxygenation is critical, and if too high, the cobalt atom may be oxidized, rather than reduced, to cobalt oxide (a clear and colorless solution).

$$2\ CoCl_2 + 2NaBH_4 + 9\ H_2O \rightarrow Co_2B + 4\ NaCl + 12.5\ H_2 + 3\ B(OH)_2 \quad (1)$$

$$4\ Co_2B + 3O_2 \rightarrow 8\ Co + 2\ B_2O_3 \quad (2)$$

$$3Co^0 + 2Au^{3+} \rightarrow 3Co^{2+} + 2Au^0 \quad (3)$$

When the diameter of the Co nanoparticle is fixed, a third step involving galvanic replacement is carried out (Equation 3). Here, cobalt is oxidized back to Co^{2+} and the Au^{3+} ions are reduced to elemental gold, depositing on to the cobalt template as hollow spheres. While this mechanism is not well understood, it is believed that during galvanic replacement, each of the materials displays a sufficient porosity allowing for diffusion of the cobalt ions outward and away from the transient cobalt template and diffusion of the gold ions inward and onto the transient cobalt template. Scheme 1 illustrates the synthetic process by which HGNs are formed.

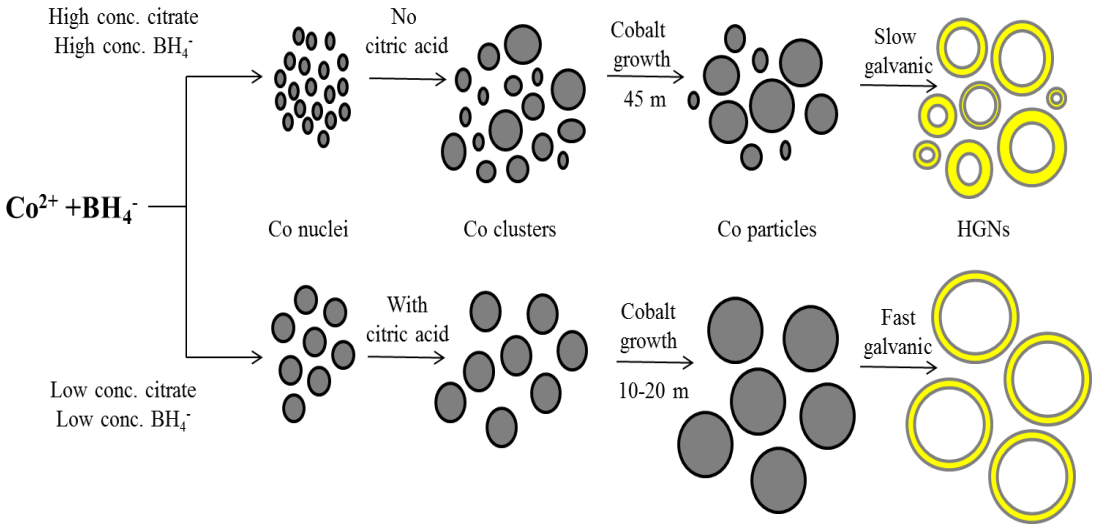

Figure 2.5: Schematic illustration of the HGN synthesis and growth mechanism. Upon the addition of sodium borohydride to the cobalt salt/sodium citrate solution, Co^{2+} is reduced to Co^{1+} by BH_4, and produces Co_2B. Upon reaction with small amounts of oxygen, Co_2B is converted to Co^0. It is this species that coalesces to form cobalt seed clusters stabilized by citrate ions. At high citrate concentrations, and higher molarities of borohydride, a large number of seeds are formed, which then go on to generate small particles. At the same cobalt concentrations, a relatively lower concentration of citrate will produce fewer, larger seeds. At very low concentrations of citrate, which are desirable for large, NIR absorbing HGNs, the cobalt particles are unstable. To counter this, we have found that the addition of citric acid will aid directly after seed nucleation can stabilize the particles without generating additional seed clusters. In addition, citric acid decreases the pH of the growth solution, increasing the rate of hydrolysis of the sodium borohydride. This means that all seeds will experience growth uniformly. The reduction of the growth time from 45 m to 10 m results in large cobalt nanoparticles which are free of oxidative damage. Finally, whereas slow addition of the gold solution and cobalt solution during the galvanic replacement step produce variation in the gold shell thickness, increasing the rate at which galvanic replacement takes place produces uniform gold shells.

2.5 Conclusion

We have demonstrated an improved and optimized synthesis for highly reproducible NIR absorbing HGNs with narrow line width that can be produced without the use of polymers. We have found that the reaction time of the cobalt particles has a significant effect on the resulting HGN properties, and that by reducing the amount of borohydride used, this time can be reduced to as little as 5 minutes, allowing for significantly more consistent results. Additionally, by decreasing the concentration of sodium citrate, and introducing a secondary addition of citric acid after cobalt seed formation, we have been able to generate large cobalt particles, while maintaining good stability.

Chapter Three

Additional Studies and Applications of Hollow Gold Nanospheres (HGNs)

3.1 Study of the Interaction of Citrate-Capped Hollow Gold Nanospheres with Cu^{2+}

3.1.1 Introduction

Since metal ions are common components of biological solutions, it is important to determine the factors affecting the interaction between various metal ions and gold nanostructures that can lead to differences in stability and aggregation. While aggregation resulting from the formation of coordination complexes between metal ions and ligands on the surface of gold nanostructures may be undesirable for certain applications like photo thermal therapies, metal ion induced aggregation may be useful in other applications. For example, the LSPR shift resulting from metal ion induced aggregation has been exploited for use in the colorimetric detection of metal ions.[275-277] However, the possible effect of metal ions on the properties and stability of HGNs have not yet been explored or well understood.

Citrate is a common ligand used in both the synthesis of gold nanostructures and as a capping agent to prevent aggregation.[66,278-279] However, in the presence of metal ions, gold nanostructures capped with citrate[40] or other chelating ligands such as amino acids[275-277] tend to aggregate due to the coordination complexes formed

between the capping agent and metal ions. In fact, this metal ion induced nanoparticle aggregation has been explored to develop inexpensive metal ion detection methods using citrate and amino acid capped gold nanoparticles.[275-277,280] In this study, citrate was employed as a stabilizing agent because of its enhanced negative charge when compared to amino acids, for example, cysteine at a neutral pH.[281-282]

In this study, we have conducted a systematic study of interaction between the HGNs and Cu^{2+}. The strength of the interaction between the HGNs and Cu^{2+} was determined by the slope of the calibration curve that relates the extent of aggregation of HGNs with the concentrations of the Cu^{2+} in solution. The extent of aggregation of HGNs was determined using the ratio of absorbance at the λ_{max} of the non-aggregated HGNs solution to the absorbance at the λ_{max} of the aggregated HGNs solution. We found that the extent of metal ion-induced aggregation depends on the nature and the concentration of the metal ion, as well as the concentration and the level of dispersion of the HGNs. The results of this study provide information that may be used in the design of HGNs that are stable in electrolyte solutions and the development of HGNs based colorimetric methods of metal ion analysis.

3.1.2 Experimental

The interaction of citrate-capped HGNs with Cu^{2+} was studied using UV/Vis absorption spectroscopy. a typical experiment, 900 µL of the HGNs solution was placed in a cuvette. A spectrum was then collected across the visible region from 350 nm – 800 nm. The HGNs were then titrated with small increments of a 10 mM metal

ion solution. A new spectrum was taken every 5 minutes after each addition of the metal ion solution until the SPR stabilized and no longer shifted. Usually, 5 - 20 min was needed to allow the reaction to reach equilibrium. The ratio of absorbance at the λ_{max} of the non-aggregated HGNs solution to the absorbance at 750 nm or 700 nm (λ_{max} of the aggregated HGNs solution) after each addition of metal ion was determined and graphed against the concentration of the metal ion. The absorbance ratio was used instead of absorbance at one wavelength in order to eliminate the effect of the HGNs concentration on the slope of the calibration curve. The slopes of the calibration curves were used to compare the strength of the interaction between the HGNs and Cu^{2+}.

3.1.3 Results and Discussion

3.1.3.1 Interaction of Citrate-capped HGNs with Common Metal Ions

The citrate-capped HGNs used in the study were characterized by scanning electron microscope (SEM). Representative SEM images of HGNs before and after exposure to Cu^{2+} metal can be seen in Figure 3.1. Before exposure to Cu^{2+} salt the HGNs are relatively monodispersed with very little aggregation. The average particle size, including shell, is 17.6±2 nm. Once the particles have interacted with Cu^{2+} salt all the particles are aggregated in to one large, irregularly shaped body. These aggregates are up to several microns in diameter.

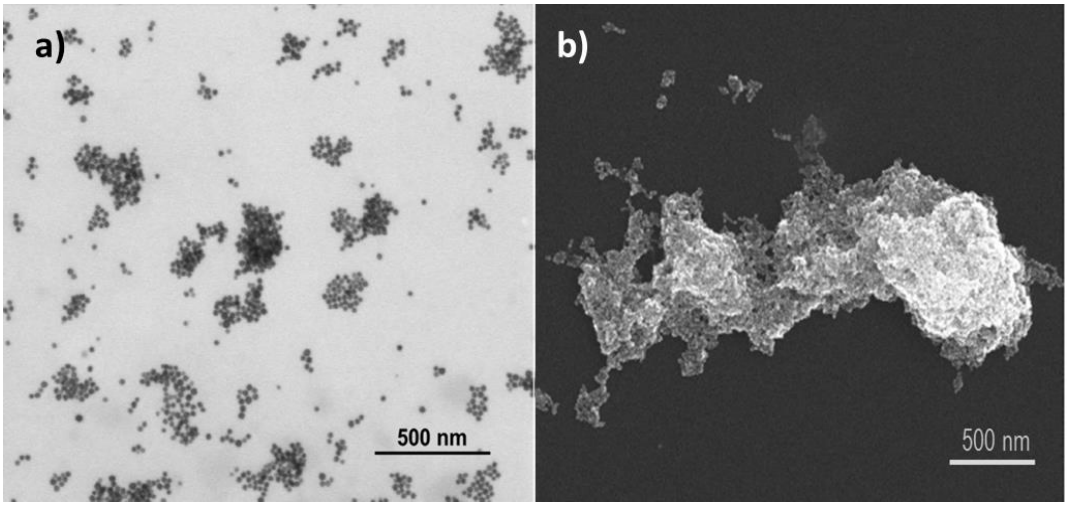

Figure 3.1: SEM image of HGN's before and after exposure to Cu^{2+} metal ions. Image (a) shows HGNs suspended in water. The nanoparticles are monodispersed with an average diameter, including both core and shell, of 17.6±2.0 nm. Image b shows the aggregation of HGNs following titration with Cu^{2+} ions.

Typical changes in the absorption spectrum of the citrate-capped HGNs with increasing concentration of Cu^{2+} are shown in Figure 3.2 using Cu^{2+} as examples. As the metal ion concentration increases, the absorption maximum is shifted to a longer wavelength, which is consistent with the aggregation of the HGNs. It can be seen that when the HGNs are suspended in solution, without the addition of any metal ions, the absorption peak is centered at ~550 nm. This peak is symmetric in shape and has a narrow full width half maximum (FWHM), which is indicative of a homogeneously sized and monodispersed nanoparticle population in solution. Once the metal ions are added the spectrum both red shifts and broadens. In addition to a shoulder near the original absorption of ~550 nm, there is a new absorption peak at ~650 nm. This

indicates polydispersity of size among the HGNs in solution. Additionally, the absorption FWHM extends several hundred nanometers indicative of aggregation.

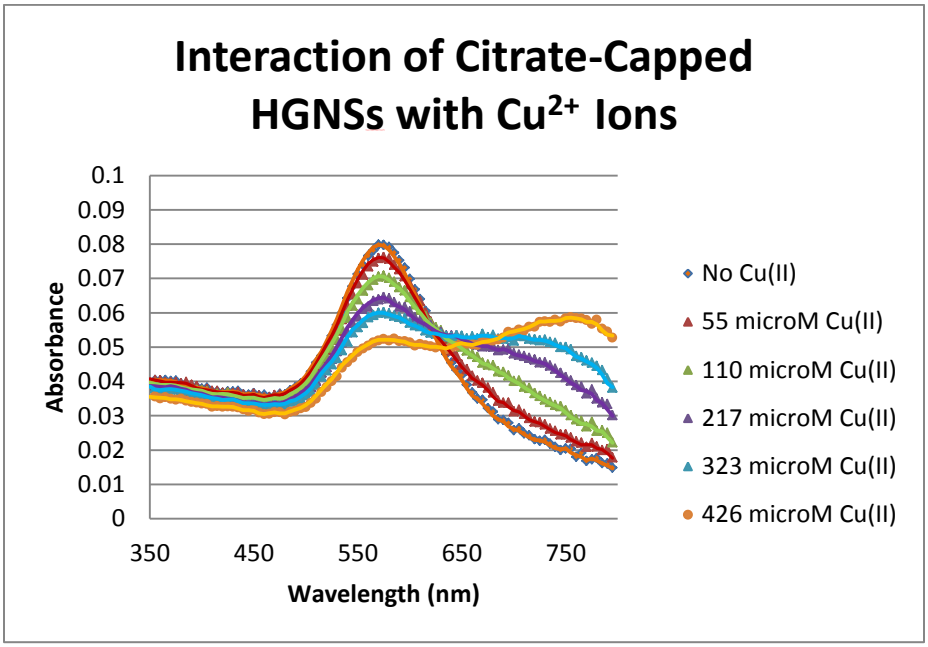

Figure 3.2: Plasmon resonance spectra of citrate-capped HGNs at the presence of various concentrations of Cu^{2+}.

3.1.3.2 Effects of the properties of the HGNs on the calibration curve

It was observed that the calibration curves were dependent on the concentration and the level of dispersion of the HGNs before the addition of metal ions. The concentration of HGNs did not affect the slope of the calibration curve, but did affect the linear range of the calibration curve. The calibration curves are based on absorbance ratio instead of absorbance at a particular wavelength, which eliminates the dependence of the slope of the calibration curve on the concentration of the HGNs. However, the detection limit and the linear concentration range of the

calibration curve did vary with the concentration of the HGNs used. It was found that the higher the concentration of the HGNs is, the higher both the lower and the upper limits of the linear concentration range are. The limits of the linear range increase because a higher concentration of HGNs requires a higher concentration of metal ions to reach the same level of aggregation.

The slope of the calibration curve was independent of the concentration of the HGNs and was correlated to the level of HGN dispersion before the introduction of metal ions. The absorbance ratio of the HGNs in the absence of metal ions is a good indicator of the level of dispersion of the HGNs, with a higher absorbance ratio indicating greater dispersity.

3.1.3.3 Effects of the nature of the metal ions

The calibration curves were determined for the binding of HGNs with Cu^{2+}. It was observed that the slope of the calibration curve was dependent on the nature of the metal ions when HGNs of the similar size, level of dispersion and concentration were used. The slope of the calibration curve indicates the sensitivity of HGNs aggregation to the change in metal ion concentration, which in turn indicates the binding strength between the HGNs and the metal ions.

A calibration curve for Cu^{2+} is shown in Figure 3.3. The slope of the linear portion of the graph for Cu^{2+} is -0.0623 μM^{-1}.

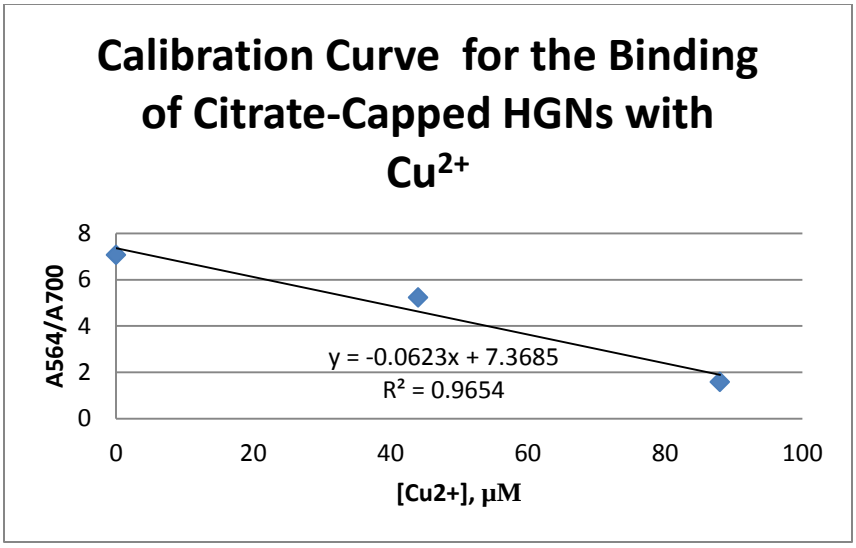

Figure 3.3: Calibration curves for the binding of citrate-capped HGNSs with Cu^{2+}

3.1.4 Conclusion

The results of this study indicate that the interaction between citrate-capped HGNs and Cu^{2+} depends on the nature and the concentration of the metal ions, as well as the concentration and the level of dispersion of HGNs before the addition of metal ions. In general, the strength of interaction between the HGNs and Cu^{2+}, represented by the slope of the calibration curve, correlates to the stability constant ($\log K_1$) of the metal–citrate complex. It was found that the larger the $\log K_1$ is, the stronger the interaction is, and the larger the slope of the calibration curve is. This type of correlation could be used to predict and compare the relative strength of interaction between citrate-capped HGNs and different metal ions and to determine the stability of the HGNs in a solution with a particular metal ion composition. In addition, lower HGNs concentration and higher level of dispersion of HGNs increase the sensitivity of the HGNs to metal ion induced aggregation. The results have important

implications in the use of HGNs or similar metal nanostructures for biomedical applications such as sensing, imaging, drug delivery, and cancer therapy. In addition, the results provide some new insights for the development of colorimetric analysis of metal ions using HGNs.

3.2. A Novel Technique for Visualizing Intra-Lymphatic Primo Vascular System Using Hollow Gold Nanospheres

3.2.1 Introduction

The primo vascular system (PVS) network is present in mammals in solid organs, structures of the central nervous system, skin, and inside blood and lymphatic vessels (LVs).[283-289] The potentially regenerative role of the PVS was initially described by Bonghan Kim[290-291] and recent reports suggest that the PVS plays a role in non-marrow hematopoiesis and as a storage site for adult stem cells.[292-293] The PVS network is small in diameter (20-50 μm) and translucent, making it difficult to visualize even with the aid of a microscope. [288,294-295] However, one advantage to the translucence is that the LVs have been visualized with contrasting agents including fluorescent nanoparticles[296-298] and various dyes including Janus Green B, and Alcian Blue.[288,299-302] The use of contrasting agents with microscopy has allowed for the observation of IL-PVS in different species including rabbits, rats and mice.[283,288-289,296-297,300] However, the use of Alcian blue, the contrasting agent which has shown the best performance in literature, is tedious, time consuming, toxic and unreliable.[288,301-302]

The main objective of this study is, therefore, to develop a new method for identifying the IL-PVS in a user-friendly way and with an acceptable reproducibility. A technique was designed after carefully studying the unique micro-anatomical structures of the PV and its sub-PVs inside an LV.[283,303] One of the main characteristics of the PV is that it has pores on its external wall.[303-306] Findings from a rabbit PV study using phase contrast X-ray microscopy described PV pores as ~0.5 mm apart along the PV wall and oval in shape.[303] On average, the internal diameter of the pore was reported to be smaller (~1 μm) than the external diameter (2-5 μm).[303]

We have designed a method to optically visualize the IL-PVS using a novel contrasting agent, hollow gold nanospheres (HGNs). HGNs are an excellent e choice because their observed color can be easily tuned through synthesis. They are also non-toxic, biocompatible, chemically inert and in the correct size regime. Additionally, HGNs were found to disperse easily in bio-fluids and be non-reactive with biomolecules within the lymphatic fluid making them useful in the successful visualization of the IL-PVS.

3.2.2 Materials and Methods

HGN's synthesized for this study were prepared as described in chapter 2 with modifications. The HGNs were turquoise and green in order to show maximum optical contrast to tissue and blood *in vivo*. The turquoise HGNs had a surface plasmon resonance (SPR) of 675 nm and diameters ranging from 50-70 nm, while the

green HGNs had an SPR of 800 nm and a diameter of 100-125 nm. The optical density of the HGNs varied from 0.35-5.0. HGNs were characterized by transmission electron microscopy (TEM). Figure 3.4 shows a representative HRTEM image of HGNs. The particles are spherical and monodispersed with a uniform gold shell surrounding a hollow interior.

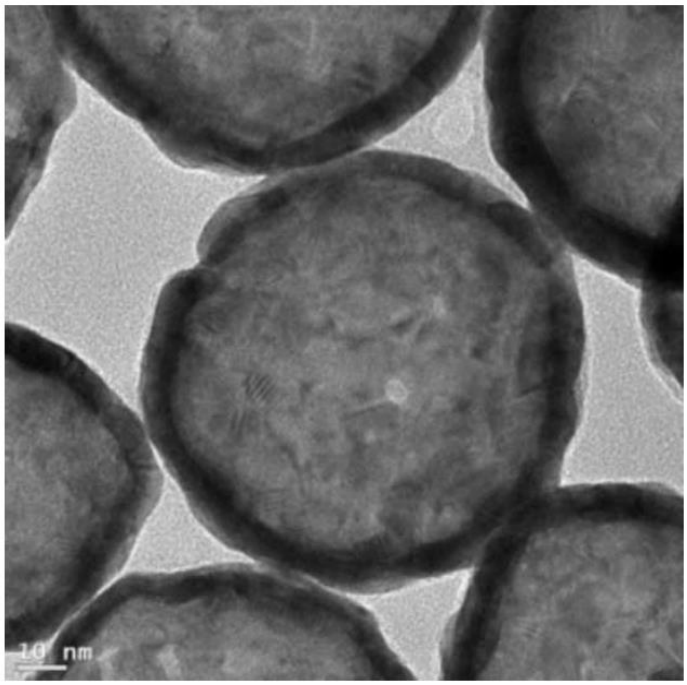

Figure 3.4: Representative HRTEM image of HGNs.

Prior to use for IL-PVS visualization, HGNs were concentrated 30 times by centrifugation for 30 min at 400 *g* for the particles with a diameter range of 100-125 nm, and at 1,125 *g* for the particles 50-70 nm. After centrifugation the supernatant was carefully removed leaving an HGN pellet. The pellet was resuspended in PBS to

constitute a 400 μL HGN suspension and it was drawn into a 1 mL syringe ready for infusion.

3.2.3 Visualization and Harvesting of the IL-PVS Using HGNs

Rats were divided into three study groups to determine the effect of HGN size on IL-PVS visualization and also to determine whether gender was important. In Group 1 (n=11), LLNs of male rats were injected with HGNs in a size range from 100-125 nm. In Group 2 (n=4), LLNs of male rats were injected with HGNs in a size range from 50-70 nm. In Group 3 (n=4), LLNs of female rats were injected with HGNs in a size range from 50-70 nm. The prepared HGN suspension (400 μL) was injected slowly at a time span of approximately 15 seconds into the LLNs using a 30-gage needle. Within minutes following the infusion of the HGN suspension, abdominal fatty tissue surrounding LVs was carefully dissected to better visualize the lumen of vessels. Figure 3.5 is an image of multiple LVs with IL-PVS (black arrows) and PNs (white arrows) in a rat model, contrasted by HGNs.

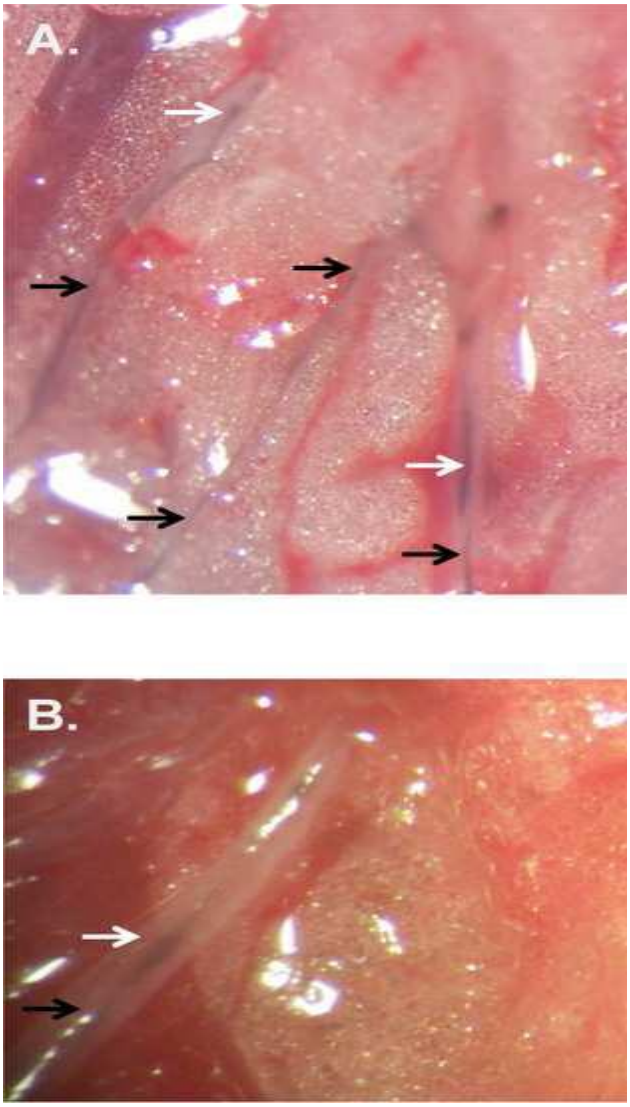

Figure 3.5: (A) Image of multiple LVs with IL-PVS (black arrows) and PNs (white arrows) in rat, contrasted by HGNs. (B) High magnification image (40x) of IL-PV (black arrow) with PN (white arrow) contrasted by HGNs.

3.2.4 Results and Discussion:

Table 1 summarizes our experimental study results. With the HGN method, the IL-PVS was confirmed in 18 out of 19 rats studied. HGNs for both size ranges tested, i.e., 50-70 nm and 100-125 nm, provided good optical contrast for the IL-PVS. The method produced the same results in both genders. The average time between the HGN injection and the IL-PVS to be visible was less than 10 min. The only failure was experienced with one of the earlier cases, which appeared to be caused by a faulty HGN injection. Following the HGN injection, LVs did not darken as expected, indicating that HGNs were not flowing out from the LLN into the LVs.

Table 1. Summary of Results of IL-PVS visualization in rats using HGNs.

Group #	Gender (n)	HGN size (nm)	Color	# of rats identified with IL-PVS	Time to visualize IL-PVS (min)
1	M (11)	100-125	Green	10	9.2±2.6
2	M (4)	50-70	Turquoise	4	7.5±2.5
3	F (4)	50-70	Turquoise	4	10.0±4.5

Table 1: Summary of results of IL-PVS visualization in rats using HGNs.

3.2.5 Conclusion:

Although many reports on the PVS have demonstrated that the system has an important role in normal physiological function, difficulties in identifying and harvesting its components has significantly delayed the advancement of PVS research. Our approach to developing an IL-PVS visualization technique, based on the microstructure of the PV, which uses properly sized HGNs with ideal optical

contrast properties, provided a rapid and reliable method. Administration of HGNs to LLNs in a size range of 50-125 nm provided a turquoise to green color optical contrast that allowed us to identify the IL-PVS within 10 min at a 95% success rate in a rat model.

3.3 Synthesis, Characterization and Surface Enhanced Raman Scattering (SERS) of Hollow Gold-Silica Double Shell Nanostructures

3.3.1 Introduction

Surface-enhanced Raman scattering (SERS) is a powerful spectroscopic technique that can provide non-destructive and ultrasensitive characterization of analytes down to the single-molecule level while simultaneously examining their chemical structure.[307-309] Several studies have shown enhancement factors ranging from 10^5 to as high as 10^{15}, leading to Raman scattering cross-sections that are comparable to or even larger than those of fluorescent organic dyes.[310-312] Because of their SPR, noble metal nanoclusters (*e.g.*, gold or silver nanoparticles) are prime materials for observing enhanced Raman signals for molecules adsorbed to them.[313-316] Utilizing the benefits from the extremely high enhancement effect arising from the proximity of nanostructured metal surfaces, SERS has been exploited in many studies to detect trace amounts of biologically relevant molecules including bacteria and viruses.[317-320]

A technique reported with high-quality SERS spectra is shell-isolated nanoparticle-enhanced Raman spectroscopy, in which the Raman signal amplification

is provided by gold nanoparticles (AuNPs) in conjunction with an ultrathin silica or alumina shell.[312,321-325] Nanomaterials with silica shells grown around gold nanoparticles with adsorbed dye molecules have been shown to be effective SERS probes.[312,323] Silanization of various metal and semiconductor nanoparticle systems has shown great success in protecting their surface characteristics and facilitating bioconjugation[326-327] in several key manners, including enhancement of the colloidal stability of nanoparticles, providing tunable solubility in various solvents, and tailoring their size and shape-dependent optical properties.[323,328] The numerous applications that are relevant to silica coating within the materials and biomaterials disciplines has been already reported, however in almost all cases the coatings are limited to a particular type of nanoparticle or surface capping agent.[329-333] Some methods exist whereby highly controlled silica coating shells are deposited onto AuNPs by priming initially the gold surface with (3-aminopropyl)-trimethoxysilane (APTMS) or thiol-modified poly(ethylene glycol) (mPEG-SH) and in turn growing the shell in ethanol using a modified Stöber method, obtaining different sizes and shapes.[323,334]

In this work, we have carried out a systematic study of the structural and optical properties of two unique gold and silica nanostructures, hollow gold-silica double shell (HGSDS) and hollow gold-silica composite (HGSC), and demonstrated their applications in detection of R6G and glucose. While gold serve to enhance the Raman signal, the silica surface affords strong interaction with β-glucose and R6G, which is highly desired for SERS. Since SERS detection of glucose is generally

challenging, the successful detection of β-glucose by SERS within a clinically relevant concentration range shows the promise of the HDSGS and HGSC as potential SERS substrates for detecting molecules that strongly interact with silica or gold.

3.3.2 Experimental

3.3.2.1 Hollow Gold Nanospheres (HGNs) synthesis

Hollow gold nanospheres (HGNs) were synthesized following protocols referred to in chapter 1 section 1.3.4 with some modifications. All glassware that was used was cleaned thoroughly with Alconox, aqua regia, and ultrapure water. In a 500 mL two-necked round-bottom flask, 100 mL of ultrapure (18 MΩ) water was combined with 100 μL of 0.4 M cobalt chloride hexahydrate ($CoCl_2 \cdot 6H_2O$, Sigma) and 400 μL of 0.1 M sodium citrate trihydrate ($Na_3C_6H_5O_7 \cdot 3H_2O$, Fisher). The solution was deaerated by bubbling with argon gas for 40 minutes without magnetic stirring to avoid cobalt nanotube formation. To that solution, 100 μL of 1.0 M sodium borohydride ($NaBH_4$, Acros) was injected, turning the solution from a pale pink to brown color over the course of few seconds indicating the formation of cobalt nanoparticles. The synthesis was carried out using air-free methods to inhibit premature oxidation of the cobalt particles.

The as-formed cobalt nanoparticle solution was further deaerated by passing argon through the reaction flask for a further 40 minutes until the evolution of H_2 bubbles ceased, indicating the complete hydrolysis of borohydride. Subsequently, 30

mL of the cobalt nanoparticles were transferred to a 100 mL beaker and immediately added to a stirring solution of 10 mL of ultrapure water and 15 μL of 0.1 M chloroauric acid trihydrate ($HAuCl_4 \cdot 3H_2O$, Acros), causing the simultaneous oxidation of Co nanoparticles and the reduction of Au^{3+} into elemental gold. The solution was allowed to stir for another five minutes under ambient conditions to allow the complete oxidation of any unreacted cobalt.

3.3.2.2 Hollow gold–silica double shell and composite

The formation of the silica shell was carried out using a modified Stöber method.[335] Briefly, 4 mL of as-prepared HGNs were mixed with 100 μL of 3-mercaptopropyltrimethoxysilane (MAPTS, $HS(CH_2)_3Si(OCH_3)_3$, Fluka), and 10 mL of isopropanol, and was stirred in a closed 20 mL vial for 2 hours. Varying amounts of ammonium hydroxide (NH_4OH, 30%, Certified ACS Plus Fisher Chemical) were added, namely (a) 200 (sample name HGSDS-1), (b) 400 (HGSDS-2), and (c) 2000 μL (HGSC). Finally 300 μL of tetraethylorthosilicate (TEOS, $Si(OC_2H_5)_4$, Fluka) were added to the vial and stirred for 24 hours. Samples HGSDS-1 and HGSDS-2 were washed by centrifugation (3000 rpm), rinsed twice with ultrapure water (18 MΩ) and once with ethanol to ensure the removal of the organic residuals. The collected nanoparticles were dispersed in 5 mL of ethanol (Gold Shield Chemical Company) or ultrapure water. The HGSC samples were not washed due to the fact that the HGN-SiO_2 complex had not precipitated following centrifugation at 19,000 rpm.

3.3.2.3 HGSDS and HGSC with R6G and β-glucose

The procedure for introducing R6G to the surface of the HGSDS consisted of mixing 1 mL of one of the HGSDS samples, dispersed in water, with 0.9 mM of R6G ($C_{28}H_{31}N_2O_3Cl$, Acros). R6G solutions were prepared in 1 mL of water. The β-glucose was bonded to samples with low and high HGSDS-1 and HGSC concentrations, with a volume ratio (Vr) between nanoparticles and glucose of 1:50 and 1:1, respectively. HGSDS-1 and HGSC were mixed with 5, 10, 20 and 30 mM of anhydrous dextrose anhydrous, ($C_6H_{12}O_6$, also known as β-glucose, Fisher). β-glucose solutions were prepared in 10 mL and 1 mL of ethanol for low and high concentrations, respectively. The solutions were allowed to stir for 24 hours.

3.3.3 Electron microscopy and optical characterization

The morphology and size of the HGSDS and HGSC nanospheres were characterized by scanning transmission electron microscopy (STEM) using an FEI Quanta 3D FEG Dual beam microscope with an accelerating voltage of 30 kV. For improved contrast between the gold and SiO_2, an SEM (FEI Nanosem 200) using STEM (scanning transmission electron microscopy) mode was used. High-resolution transmission electron microscopy (HRTEM) was performed using a FEI Titan 80-300 with accelerating voltage set to 300 kV.

UV-Vis absorption measurements were carried out using an HP 8452A spectrometer with a spectral resolution of 2 nm. Samples were sonicated 10 minutes prior to obtaining the spectrum. The Raman signals were collected using two Raman

Systems (A and B). Raman System A is a Renishaw Raman System (Renishaw Inc., model RM2000) with a 20× objective lens in backscattering geometry. The excitation laser operated at 632.8 nm with a power of ~2 mW. The integration time for each Raman measurement was 30 seconds. For the bulk detection, the laser excitation light was directly focused onto the surface of the sample solution (350 μL) with the same laser power and integration time.

3.3.4 Results and Discussion

Figure 3.3(a) shows the HRTEM of the as-prepared HGNs, revealing a core diameter of 32 nm with a shell of ~7 nm in thickness, consistent with what has been reported previously (25). Figure 3.3(b) is a micrograph of the HGSC particles which show a core diameter of ~35 nm and a 15 nm shell thickness. The mixture of gold and silica was confirmed by HRTEM analysis, shown in Figure 3.3(c), which displays contrasting colorations, suggesting that gold and silica nanoparticles were mixing.

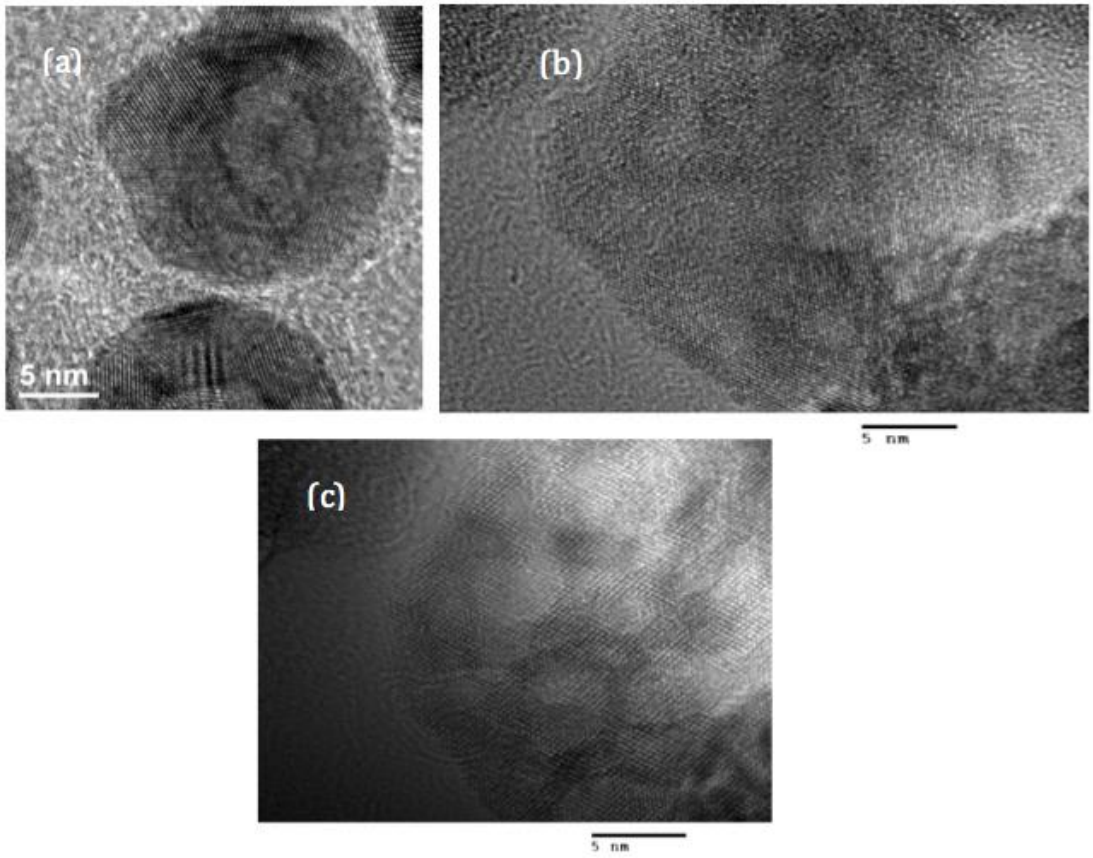

Figure 3.3: HRTEM images of (a) HGNs (b)HGSC and (c) mixture of gold and silica on HGSC.

3.3.4.1 Optical properties and SPR

Figure 3.7 displays the UV-Vis spectra of the various samples used in this study. For the HGNs, a SPR is manifested at 580 nm with an accompanying FWHM of ~100 nm, as shown in Figure (a). The 580 nm SPR, red-shifted from the normal 520 nm absorbance of solid Au nanoparticles, is indicative of the hollow nature of the HGNs.[66] This is consistent with the dimensional results gleaned from the HRTEM images of Figure 3.7 The relatively small FWHM is indicative of a fairly

monodisperse ensemble average of particle sizes. The electronic absorption spectrum of the as-formed spherical silica nanoparticles is shown in Figure 3.7(b). A monotonically decreasing absorption profile is evident, showing a weak absorption band at ~350 nm. A long tail persists to red-shifted wavelengths, indicating strong scattering due to the large size of the particles. The absorption spectrum of the 1 μm-sized HGSDS-1 sample, Figure 3.7(c), shows strong scattering characteristics also, which is consistent with the overall large and approximately micron-sized nanoparticles. There is an absorption peak near 300 nm followed by a long tail to red wavelengths. The absorbance spectrum of the smaller 500 nm HGSDS-2 sample is shown in Figure 3.7(d). Intriguingly, the spectrum of the HGSDS-2 shows an absorbance centered at 440 nm with a FWHM of ~105 nm. The peak position is due to the sensitive interplay between the silica coating and the underlying HGN resonances. The slightly increased FWHM, relative to the starting HGNs, indicates that particle size distribution likely became slightly broader upon silica coating. Finally, Figure 3.7(e) shows the absorption of the HGSC nanoparticles, which have a peak at 450 nm and a FWHM of ~110 nm. As with the HGSDS-2 sample, the peak position of the HGSC is likely due to contributions from both silica and gold materials. Additionally, the FWHM indicates some particle size inhomogeneity.

The close proximity of the HGNs to one another, coupled with the presence of the thick silica shell and additional gold layer on the silica surface, could account for the drastic spectral differences that were observed in the UV-Vis spectra shown in Figure 3.7. The exact position of HGN SPR is extremely sensitive both to particle

size and wall thickness.[336] It is known that the gold plasmon may be shifted from blue to near-IR wavelengths for certain geometries, such as nanoshells or high aspect ratio nanorods and the deposition of a second metal overlayer and thickness variations of the HGN may also drastically alter the SPR peak position.[336-340] The blue-shift is likely due to a change in the HGN cavity sizes, which has been shown by the HRTEM in Figure 3.6 (b).

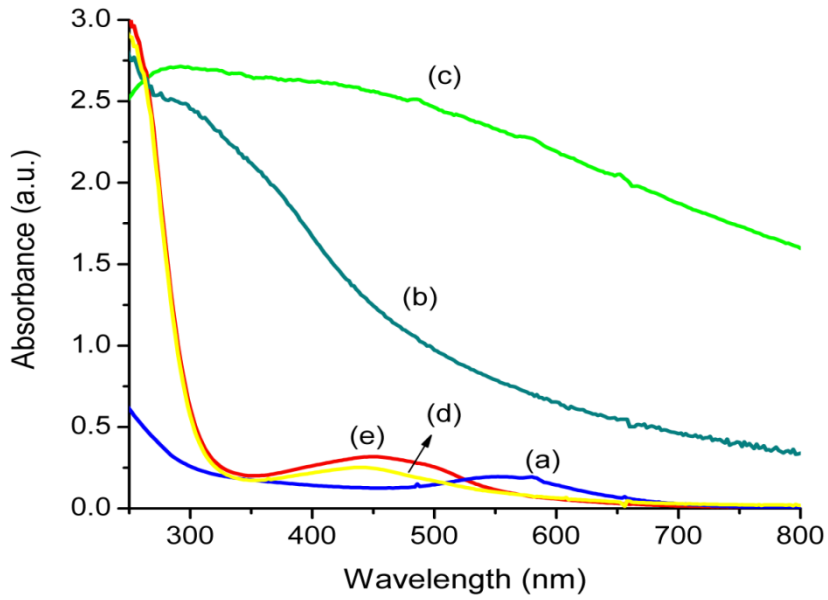

Figure 3.7: UV-Vis absorption spectra for: (a) HGNs (b) SiO_2 (c) HGSDS-1 (d) HGSDS-2 and (e) HGSC.

3.3.4.2 Surface-enhanced Raman scattering (SERS)

Figure 3.8 shows the SERS spectra of 0.9 mM R6G using HGNs and HGSDS-1 as the SERS substrate. Characteristic Raman signals (45, 46) of R6G at 775, 953, 1132, 1278, 1455 and 1646 cm^{-1} are shown in Figure 3.8 (a,b), where it is observed that band positions do not change with the presence of the silica coating. As can be seen in Figure 3.8 (a), the HGN-R6G spectrum shows the lowest Raman signal intensity. The signal increases ~7× when HGSDS-1 were used instead of the HGNs, as seen in Figure 3.8 (b), indicating that the HGSDS-1 sample has a much higher SERS efficiency than the HGNs as a substrate material.

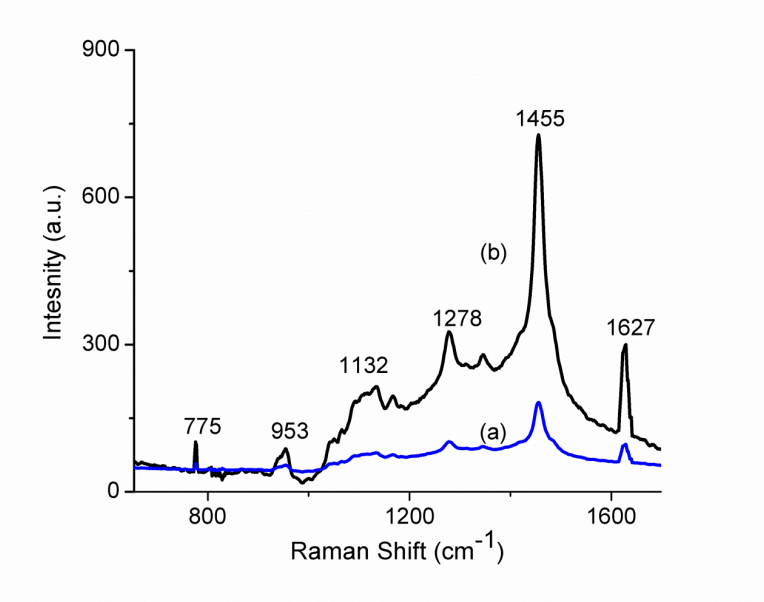

Figure 3.8: SERS spectra of R6G dye using (a) HGNs and (b) HGSDS-1 as substrates.

Figure 3.9 is a series of SERS spectra after the subtraction of the ethanol signal from that of the signal due to the β-glucose-HGSDS-1 sample. In this manner, the presence of the β-glucose could be confirmed by subtraction of the ethanol peaks, resulting in a spectrum comprised solely of β-glucose molecules. A linear relationship between the Raman intensity and the β-glucose concentration is evident at band positions of 880, 1040, 1062 and 1091 cm^{-1} which correspond to β-glucose.[341] The most intense peak was the 880 cm^{-1} band followed by the 1091 cm^{-1} peak. The inset of Figure 3.9 shows the accompanying blue-shift of the band with increasing β-glucose concentration.

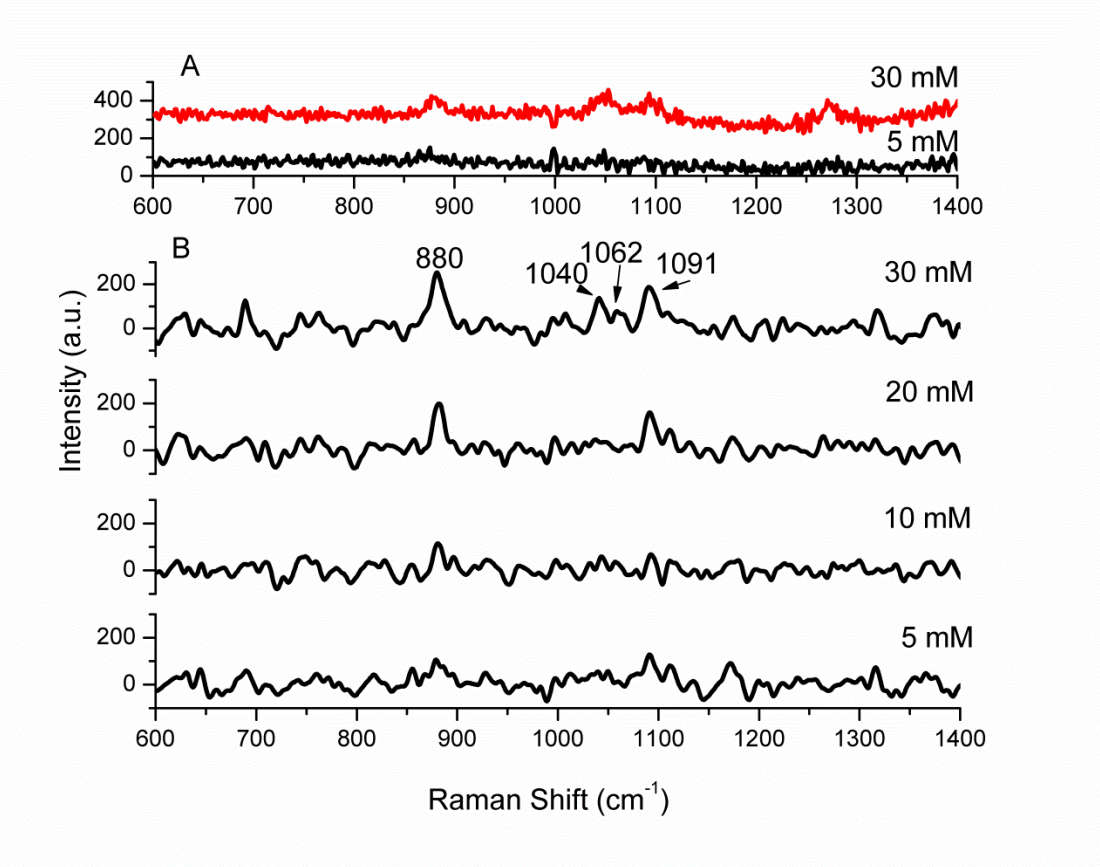

Figure 3.9: SERS spectra of β-glucose using HGSDS-a as a substrate.

As can be seen in Figure 3.8 (b), the SERS signal increases ~7× using HGSDS-1 as opposed to HGNs. It is important to note from Figure 3.8 (b) that, given the overall maximum SERS signal intensity of ~800 corresponding to 0.9 mM, a much lower limit of detection is likely. In other words, given the signal intensity, it is reasonable to assume that the limit of detection of R6G is much lower than 0.9 mM. Nevertheless, from Figure 3.8, it is reasonable to say that the silica surface is a good linker to the R6G; therefore, more R6G molecules adsorb onto the SiO_2 surface and the signal is increased. Additionally, the second gold layer on the surface of the HGSDS-1 serves to increase the zone of electromagnetic field enhancement lost by the thick coating and provides an increased density of Raman "hot spots."

3.3.5 Conclusion

In summary, we have demonstrated that HGSDS and HGSC are highly active SERS substrates for quantitative β-glucose detection in the concentration range of 5-30 mM. Compared to HGNs, the SERS signal of β-glucose using HGSDS and HGSC is enhanced, which is attributed to the relatively strong interaction between the glucose and the SiO_2 surface. This is very significant because β-glucose has traditionally been challenging to detect by SERS due to its small Raman cross-section and weak interaction with bare metal surfaces. Fundamentally, this adsorption problem has been overcome due to the chemical interplay between hydroxyls on the

silica surface and the glucose structure which facilitate the adsorption. The developed gold-silica nanostructures are also potentially useful for biomedical imaging and therapy applications. Imaging can be based on SERS or heat generated by photothermal conversion from light illumination. Similarly, they can be used for photothermal ablation therapy of cancer. Future research will explore such applications of the nanostructured studied in this work.

Chapter Four

Fe_3O_4@SiO_2 Nanoparticles Functionalized with Gold and Poly(vinylpyrrolidone) for Bio-Separation and Sensing Applications

4.1 Magnetism Background

4.1.1 Magnetism

Magnetism arises from both electronic orbital angular momentum and the intrinsic spin of an electron around its own axis. Orbital and spin motion each contribute to the magnetic dipole moment of a material which determines how a material will respond to an applied magnetic field (AMF) acting perpendicular to its magnetic axis. The magnetic moment of a material determines the torque it will experience in an applied field. It can be considered as a vector with both magnitude and direction. The net magnetic moment of a material is the sum of contributions from both electronic spin and angular momentum. The magnetic field produced by a material is proportional to its magnetic moment.

4.1.2 Magnetic materials

Magnetic materials can be classified according to the susceptibility (χ) and permeability (μ) they experience when exposed to an AMF. Susceptibility is a dimensionless proportionality constant indicative of the degree of magnetism, M, a material experiences when interacting with external field H:[342]

$$M = \chi H \quad (4)$$

If susceptibility is positive the material is paramagnetic and the magnetic field is strengthened through attraction. If susceptibility is negative the material is diamagnetic and the field will be weakened through repulsion.[342] Permeability describes how conductive a material is, with higher permeability being associated with lower resistance to an AMF. Permeability, μ, describes how magnetic induction B changes with respect to the applied field H:[342]

$$B = \mu H \quad (5)$$

4.1.2.1 Diamagnetism and paramagnetism

When exposed to an AMF diamagnetics produce a weak magnetic field opposite to the applied field. The field is diminished because of this opposition. In diamagnetics all orbital shells are filled and there are no unpaired electrons.[343] Susceptibility is temperature independent, negative, and varies between 10^{-3} and 10^{-6}.[342] Permeability is ≤ 1. When the external field is removed electronic spins relax to their initial positions.

Paramagnetic materials have unpaired electrons in their orbitals. In the absence of an applied field magnetic moments are randomly oriented producing a net magnetic moment of zero. Upon magnetic induction the magnetic moments align themselves in the direction of the applied field.[343] (Producing weak magnetic field in direction of applied one). Susceptibility is positive, temperature dependent and varies between 10^{-3} and 10^{-5}. Permeability is ≥ 1.[342]

4.1.2.2 Ferromagnetism, Anti-ferromagnetism and Ferrimagnetism

Ferromagnetic materials are multi-domain structures having unpaired electrons. All the magnetic moments in one domain are aligned parallel to one another. Atomic moments in these materials exhibit strong interactions and exhibit large net magnetization even in the absence of an applied field. Under magnetic induction all the magnetic moments in all domains align themselves with the applied field. Susceptibility of the ferromagnetic materials is positive (>> 1) and permeability is >>1.[342] All ferromagnetic materials have a temperature known as the Curie temperature (T_c). Above the Curie temperature the material loses its ferromagnetic properties and the magnetic moments are disordered. Below the Tc the magnetic moments are ordered.[344]

Anti-ferromagnetism magnetic moments of different sublattices align with equal magnitude in opposite directions. Anti-ferromagnetic materials display non-zero net magnetization in response to an applied field. Above the Neel temperature, T_N, anti-ferromagnetic materials becomes paramagnetic. Magnetic susceptibility is maximal at the Neel temperature.[344]

Ferrimagnetism occurs mainly in magnetic oxide materials with more complex structures. Two sublattices, A and B, are separated by oxygens that mediate the exchange interactions.[342] In ferrimagnetic materials, the magnetic moments of the A and B sublattices are opposite in direction but unequal in magnitude. This results in a net magnetic moment. Ferrimagnetics have high resistance and anisotropy which is directionally dependent and induced by an applied field. They exhibit spontaneous

magnetic behavior below the T_C and show no magnetic ordering, or paramagnetic behavior, above T_C.[344]

4.1.3 Superconducting quantum interference device (SQUID)

A superconducting quantum interference device (SQUID) is a superconducting ring with one or more Josephson Junctions. Cooper pairs of electrons can tunnel through Josephson Junctions without applied bias creating a resistanceless current which flows across the insulator.[345] Josephson Junctions enable flux trapped in the ring to change by discrete amounts. Small quantized periodic changes in the magnetic flux of a superconducting ring are then able to be measured as physical quantities like current, voltage and magnetic susceptibility.

4.3.3.1 Josephson Junctions

The Josephson Effect describes the process of Cooper pairs of electrons tunneling through Josephson Junctions without excitation or applied bias. Josephson Junctions are thin insulating barriers (< 2nm) also known as weak links situated along the superconducting ring. Tunneling occurs because superconductors lose their resistance below their critical temperature T_C.[346] Cooper pairs are able to travel through the junction and flow as a supercurrent without resistance because their binding energy is large compared to thermal energy scattering and the overall system energy is reduced by their coupling.[346] Energy phases become coherent and pairs can tunnel when the energy associated with electronic coupling exceeds thermal fluctuations.[347] Long range quantum coherence occurs because the entire population of superconducting electrons can be described by the same wavefunction. Although

the wavefunction of electrons may vary in phase within the superconductor all Cooper pairs within the junction maintain the same phase.[345] As Cooper pairs tunnel from one superconductor to another there is no energy loss. The supercurrent describing Cooper pair tunneling is given by:

$I=I_0 \sin\delta$ (6)

Where I_0 is the critical current and δ is the difference between the two wave phases of the two superconductors.[348]

Another consequence of transitioning below critical temperature is the active exclusion of any magnetic field present in the superconducting loop due to the Meissner Effect. As a magnetic field is applied to the superconductor below the critical temperature the superconducting loop will oppose the magnetic field by generating a screening current that flows in an equal and opposite direction to the applied field.[346] This causes the net flux in the ring to be cancelled. Under these conditions current can flow without applied voltage with the Cooper pairs carrying the current. The screening current is periodic with a period equal to one flux quantum. SQUID measures changes in the magnetic field associated with one flux quantum:[346]

$$\phi_0 = \frac{2\pi\hbar}{2e} \cong 2.0678X10^{-15}Tm^2 \quad (7)$$

When a constant bias current is perpetuated by Cooper pairs the oscillating voltage can be measured and used to evaluate the flux change down to 10^{-15} T.

4.1.3.2 Hysteresis loops

The magnetic properties and heat generating capabilities of a material can be extracted from its hysteresis loop which characterizes the interaction between an ensemble and an applied field. Thermal energy production from hysteresis loss is governed by the first law of thermodynamics since energy, which is conserved, is made up of irreversible work and heat.[349] The applied field supplies the energy responsible for magnetic moment fluctuations which are converted in to heat following reversal of the applied magnetic field (AMF) post magnetic saturation of an ensemble.[350] The dipole response of an ensemble within a field and subsequent thermal energy production is determined by the size, shape, crystallinity, composition, volume and number of domain walls in a material.[351-352] Intra and inter-particle interactions and exchange mechanisms also contribute to the response of an ensemble to an AMF.

For magnetic induction to occur an ensemble must first overcome anisotropy and any exchange or dipole interactions.[349] As the number of atomic magnetic moments aligning themselves with the AMF increases, entropy decreases until maximum magnetic saturation (M_S) is obtained.[353] Larger M_S values are correlated to higher anisotropy and greater heat generation.[353] Magnetic saturation is also generally known to decrease as particle size gets smaller and as the temperature of the applied field is increased.[354-355] Coercivity, the ensembles resistance to demagnification, typically increases as particle size is reduced and decreases as the number of domain walls grows.[356] Larger coercivity values are correlated to enhanced heat generation.[357]

Hysteresis losses are observed when the field exceeds coercivity and are proportional to the product of M_R by H_C or the area of the hysteresis loop.[358-359]

4.2 Introduction

Composite materials are used in a wide range of applications including clinical diagnostics and therapeutics, the targeting of bioterrorism agents, waste water treatment and environmental remediation.[360-367] In order to enhance performance in these fields, researchers have started to synthesize and study composite materials that take advantage of both magnetic and plasmonic properties.[368-373] One combination attracting a great deal of attention is that of iron oxide and gold.[374-379]

Typically, iron oxide and gold composite materials are synthesized for use in bio-applications like imaging, cancer treatment, and drug delivery.[380-386] In order to be compatible *in vivo*, particle diameters are generally kept between 10-100 nm.[387-389]. For example, the trend in hyperthermia applications is to employ superparamagnetic particles that have a single domain and diameters < 20 nm in order to generate maximum heat.[390-393] However, there remains a need to synthesize magnetic@plasmonic particles with much larger diameters in order to better address the requirements of applications involving bio-separation, sensing and the targeting of environmental pollutants.

Various efforts to produce gold and iron oxide composite materials >100 nm have been made in recent years. Esenturk *et al*. created gold nanostars decorated with iron oxide.[394]. While the star shape is advantageous in an application like SERS, the

iron oxide covering the particle surface dampens the plasmonic response of the gold and reduces viability as a sensing substrate. Zhou *et al*. and Bao *et al*. both created gold decorated iron oxide nanoparticles > 100 nm, however their syntheses involve multiple iterations of gold seeding, which is complex and time consuming.[395-396] Another effort to produce large gold decorated particles involved the addition of a thick silica shell (~85 nm) over the magnetic core, which diminished the magnetic saturation of the material significantly and, when Lee *et al*. used concave gold coated iron oxide to detect rhodamine B using SERS, the surface of the nanoparticles had to be further functionalized with graphene quantum dots in order to detect the dye.[397-398]

Particles lacking uniform gold coverage have been shown to exhibit diminished plasmonic response. When polyethylenimine and gold modified $MnFe_2O_4$ substrates were synthesized for bacteria detection the particle surface had partially exposed polymer and magnetic components, resulting in a diminished SERS effect.[399] A lack of continuous shell has also been found by others.[400-401] Likewise, Paterson *et al*. synthesized 500 nm superparamagnetic iron oxide nanoparticles (SPION) clusters encapsulated in self assembled dextran strands and decorated sparsely with Au seeds.[402] The clusters had low magnetic saturation (20 emu/g) and the dextran covered most of the nanostructure surface, which is not ideal for applications such as SERS sensing.

In this work, we have synthesized large (~200 nm) composite nanoparticles with a unique surface morphology comprised of gold and PVP

(Fe_3O_4@SiO_2+Au+PVP). Particles were characterized by a combination of spectroscopic techniques including ultra-violet visible (UV-Vis) spectroscopy, energy dispersive spectroscopy (EDS), powder X-ray diffraction (PXRD), Fourier transform infrared (FTIR) spectroscopy, electron microscopy (EM), superconducting quantum interference device (SQUID) magnetrometry, and surface enhanced Raman scattering (SERS) spectroscopy. The gold and PVP coatings render the particles resistant to oxidation and easy to functionalize. The gold roughened nodules are desired for generating hot spots for EM enhancement and are uniformly distributed across the entire surface.[403] Furthermore, the polymer and noble metal coatings are ultra-thin so that the particles maintain a significant amount (68%) of their magnetic saturation values compared to bare magnetite. To evaluate their applications, we performed proof-of-concept experiments demonstrating bio-separation and SERS sensing in which we targeted glucagon like peptide 1 (GLP-1), a large gastrointestinal hormone that stimulates insulin release from pancreas β-cells.[404] We show a limit of detection (LOD) down to 10^{-7} M using SERS. Our targeting and binding was performed rapidly (~30 m) with only a mild reducing agent, tris(2-carboxyethyl)phosphine (TCEP), our bio-separation took ~30 s and our sensing was performed without the need for reporter molecules.

4.3 Experimental

4.3.1 Chemicals

Analytical reagent chemicals and 18.2 MΩ·cm ultrapure milli-Q water were used for the preparation of all solutions. All reagents were used without further purification. Sodium citrate ($C_6H_5O_7 \cdot 2H_2O$) and sodium borohydride ($NaBH_4$) were purchased from Fisher Scientific. Hydrogen-tetrachloroauric acid ($HAuCl_4$) was purchased from STREM chemicals. Polyvinylpyrrolidone (PVP) $(C_6H_9NO)_x$ (MW=55000), tetraethylorthosilicate (TEOS) ($Si(OC_2H_5)_4$), 4-phenyl-butaric acid ($C_{10}H_{12}O_2$), polyethylene glycol (PEG) (MW=3350) $(O\text{-}CH_2\text{-}CH_2)_x\text{-}OH$) and 3-aminotetramethoxysilane (APTMS) ($H_2N(CH_2)_3Si(OCH_3)_3$) were purchased from Sigma Aldrich. K-tertbutoxide (C_4H_9OK) was obtained from Spectrum Chemicals. 3-mercaptopropionic acid (MPA) ($HSCH_2CH_2CO_2H$) was purchased from Acros Chemicals. GLP-1 peptide (HGEGTFTSDVSSYLEEQAAKEFIAWLVKGRG-[peg3]-C-NH_2) was purchased from Ana Spec Inc. Tris(2-carboxyethyl)phosphine (TCEP) ($C_9H_{15}O_6P$) was purchased from Thermo Scientific. All glassware was cleaned with aqua regia and milli-Q water before using.

4.3.2 Preparation of Fe_3O_4

Magnetite particles were synthesized as previously reported in literature.[405] Briefly, trivalent iron was reduced to a mixture of ferric (Fe^{3+}) and ferrous ($Fe2^{+}$) ions. Under strong basic conditions a 1:2 molar ratio of ferric to ferrous ions coalesced to form Fe_3O_4. The reactions are shown in equation 1.[406]

$$Fe^{2+} + 2Fe^{3+} + 8OH^- \rightleftharpoons Fe(OH)_2 + 2Fe(OH)_3 \rightarrow Fe_3O_4\downarrow + 4H_2O \quad (1)$$

To achieve uniform, monodispersed magnetite spheres, 1.35 g $FeCl_3 \cdot 6H_2O$, 3.60 g sodium acetate, 0.10 g (3350 MW) polyethylene glycol (PEG) and 40 ml ethylene glycol were combined in a larger beaker and stirred at RT for ~ 30 minutes. During the course of the reaction the color changed from clear to mustard yellow-brown. After 30 minutes the solution was transferred to autoclave containers and heated at 200° C for ~10 hours. After cooling to RT the particles were collected with a magnet and the black solid product was washed first with ethanol and then water for 6 cycles each to remove impurities. The clean particles were then dried in an oven at ~70° C and the black powder was stored in glass vials.

4.3.2.1 Silica shell addition

The addition of the silica shell was achieved by using the well-known Stöber method (hydrolysis and condensation of tertaethoxyorthosilane (TEOS)) with modifications.[407] First, monodispersity of Fe_3O_4 nanoparticles was achieved by sonicating 20 mg Fe_3O_4, 95 mg 4-phenylbutyric acid and 65 mg K-tertbutoxide in 15 mL dichloromethane (DCM) and 10 mls toluene in a 250 mL pear-shaped flask. After 20 min of sonication at room temperature, the particles were washed twice each with methanol, isopropanol, and ethanol. Then, the monodispersed magnetite nanoparticles were combined with 38 mL ethanol, 6 mL water, and 1 mL NH_4OH at a concentration of 28% NH_3 in water. This suspension was then sonicated at 70° C for a few minutes before adding dropwise, over a period of 15 minutes, a solution consisting of 2 mL ethanol, 25 µL TEOS, and 6 drops (via Pasteur pipet)

mercaptopropionic acid (MPA). The solution was then sonicated for 3 hours and the resulting sample was washed three times with ethanol.

4.3.2.2 Addition of APTMS

To add the 3-aminopropyltrimethoxysilane (APTMS) linker, the Fe_3O_4 particles were resuspended in 30 mL ethanol and 1000 µL APTMS was added to the solution which was suspended in a boiling water bath. Stirring was performed manually for 1 h. The solution temperature was maintained at ~80°C. Additional ethanol was periodically added to maintain the initial volume. Following addition of the linker the sample was washed 3 times with ethanol and then water.

4.3.2.3 Gold and PVP deposition

The gold deposition synthesis was previously reported in literature and was carried out with modifications.[408] Gold deposition was achieved through the reduction and hydrolysis of $HAuCl_4$ gold salt. NaOH was used to raise the pH of the solution to ~10 allowing for hydrolysis to occur and the $HAuCl_4^-$ salt to form a gold hydroxyl solution. $HAuCl_4^-$ forms six major species $[Au(OH)_xCl_{4-x}]$ depending on the extent of hydrolysis of which only the $Au(OH)_3$ species precipitates and binds to the surface of the particles.[49] A round bottom flask was used as the reaction vessel for the gold deposition. A solution of 4.5 mL water and 1.5 mL 6.35 mM $HAuCl_4$ was adjusted to a stable pH of 10.0 using 0.1 M NaOH. The solution turned from clear to red-purple. The Fe_3O_4 sample was then added to the solution and sonicated for 20 min at 70 ºC. The sample was then washed 3 times with ethanol and then water.

To form a roughened surface morphology of gold nodules on the particles a seeded magnetite sample was suspended in a solution of 40 mL K-gold and 2 mL 10mM sodium citrate. K-gold was prepared by adjusting a 0.375 M solution of chloroauric acid ($HAuCl_4$) to pH 10 using potassium carbonate (K_2CO_3) and stirring in the dark for 24 h. A 6.6 mM solution of $NaBH_4$ solution (1 mL per 10 mLs K-gold) was prepared to reduce complexed gold hydroxide anions in K-gold in to $Au(OH)_3$ seeds. 4 mL $NaBH_4$ and 200 µL 1 % (w/v) PVP was added simultaneously to the sonicating solution. The solution was sonicated for 30 min at 70 ºC, then washed 3 times with ethanol and then water followed by drying.

4.3.3 Bio-Separation

To demonstrate our composite materials ability to rapidly bind and separate GLP-1 from solution we added 20 µL of an 8mM tris(2-carboxyethyl)phosphine hydrochloride (TCEP) to 2 mL of Fe_3O_4@SiO_2+Au+PVP nanoparticles containing GLP-1 at a concentration of 2.7 X 10^{-7} M. The solution was allowed to incubate for ~30 minutes at which time the nanoparticles were collected under magnetic induction and resuspended in water. The resulting suspension was then characterized with UV-Vis spectroscopy.

4.3.4 Instruments and Characterization

UV-Vis spectroscopy was performed using an Agilent Cary 60 UV-Vis spectrometer with solvent baseline correction and a scan rate of 24,000 $nm \cdot min^{-1}$. FTIR measurements were taken using a Perkin-Elmer Spectrum One with a resolution of 4 cm^{-1} using a scan range of 200-4000 cm^{-1} and a scan rate of 0.20 cm/s. PXRD

was performed on a Rigaku Smart Lab X-ray diffractometer with Cu Kα (1.54 Å) radiation with all samples analyzed from 20° to 80° (2θ) with a step size of 0.01° and scan rate of $1°\cdot min^{-1}$. STEM images were acquired using an FEI Quanta 3D dual beam microscope, operated at 10 kV. STEM-HAADF imaging and EDS elemental mapping were performed on a Philips F20 Tecnai TEM operated at 300 kV, fitted with a Bruker Quantax EDS detector. Samples were prepared for SEM and TEM analysis by drying Fe_3O_4 in ethanol on copper-carbon mesh grids. Magnetic properties were investigated by SQUID magnetrometry with an external magnetic field ranging from -10000 Gauss to 10000 Gauss at 300K. Raman and SERS data was collected using a Renishaw Invia Raman system with a 514 nm excitation wavelength, a laser power of 30 mW and a single 10 s accumulation.

4.4 Results and Discussion

4.4.1 Particle Morphology and Composition

Electron microscopy was used to determine the size and surface morphology of particles in each sample. Representative scanning electron microscopy (SEM) images of magnetite with and without a silica shell are shown in Figure 4.1. The bare magnetite particles are solid, spherical and monodispersed. The particles were analyzed with Image J software and have an average diameter of ~175 nm. The addition of silica is known to protect the surface of Fe_3O_4 from oxidation and render the particles stable to oxidation and easy to functionalize. The surface of the silica coated particle is significantly smoother than that of the bare magnetite. Silane

functionalization produced a shell of ~15 nm resulting in an average particle diameter for the silica coated magnetite of ~190 nm. Particles functionalized with gold plus PVP had their diameters increase up to an average of ~200 nm.

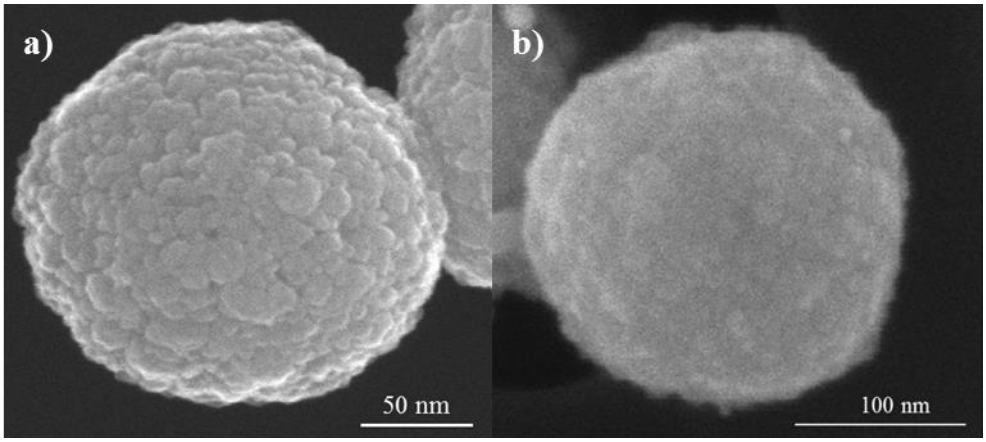

Figure 4.1: SEM images of a) pristine magnetite particles and b) magnetite particles with a silica shell.

Figure 4.2 shows a representative scanning transmission high angle annular dark field (HAADF) of the a) gold decorated intermediate step and b) gold plus PVP decorated magnetite particles. The presence of gold can be seen in the images as bright white spots on the surface of the particles. The gold clusters decorating the surface are nodulated and irregularly shaped however, the coverage along the surface of each particle is uniform and complete.

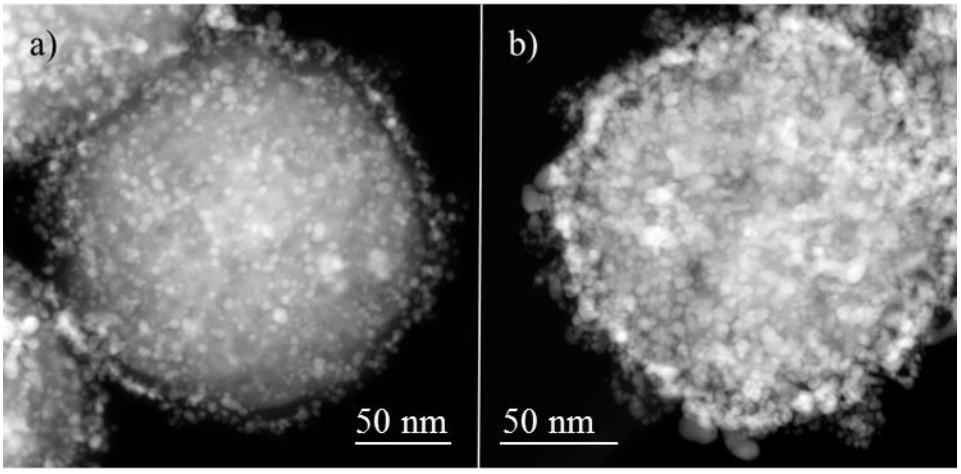

Figure 4.2: STEM-HAADF images of magnetite decorated with: a) gold intermediate and b) gold plus PVP

Figure 4.3a shows a STEM-HAADF image of gold decorated magnetite particles. Elemental analysis of the particles using energy dispersive x-ray spectroscopic (EDS) are shown in Figure 3, revealing iron (b), silicon (c), oxygen (d) and gold (e) in the composite material. There is uniform coverage of the particles with each individual element, confirming the functionalization of the ensemble with silica and gold.

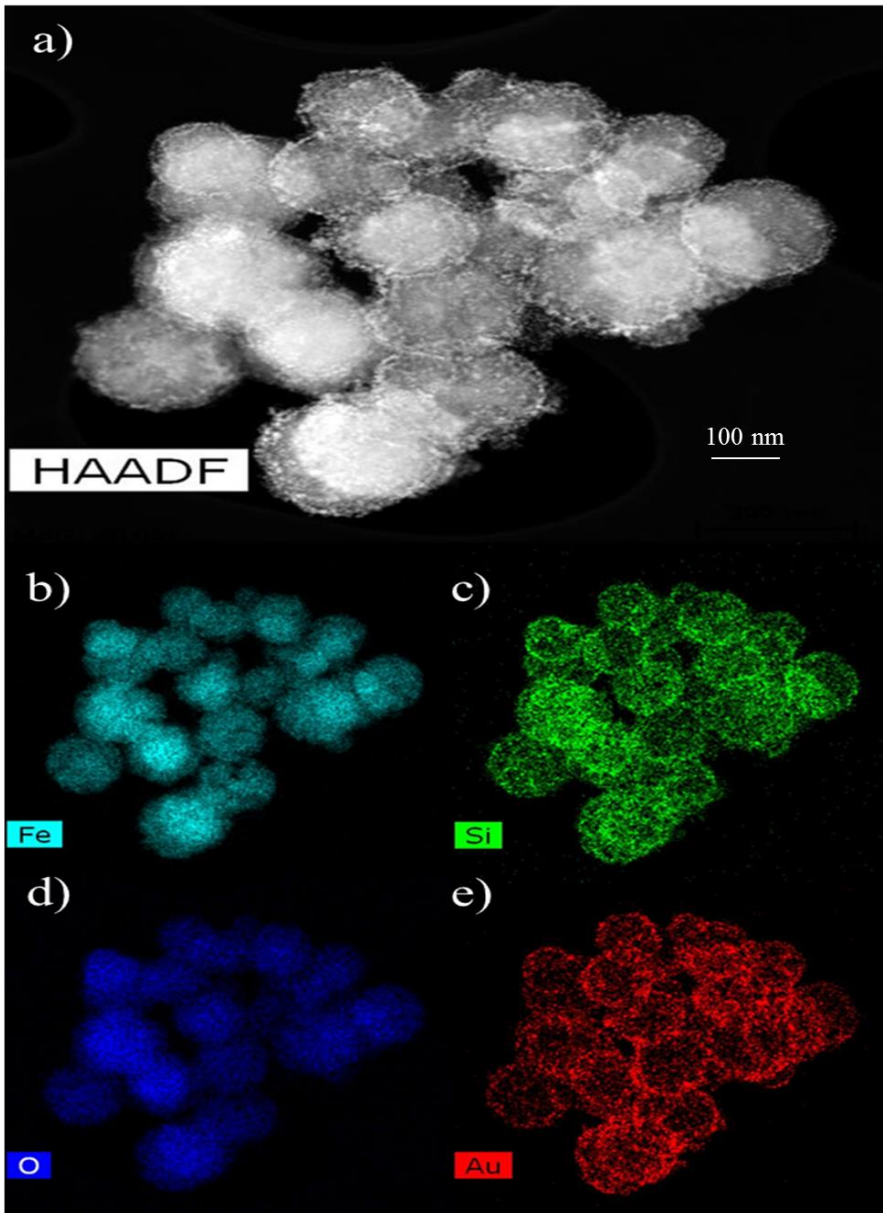

Figure 4.3: a) STEM-HAADF image of gold decorated magnetite. Elemental analysis of functionalized particles using energy dispersive x-ray spectroscopic (EDX): b) (turquoise) iron; c) (green) silicon; d) (blue) oxygen and e) (red) gold.

The XRD patterns for bare magnetite and magnetite decorated with silica and gold are shown in Figure 4.4. Magnetite has 2 theta peaks located at: 30.32°, 35.10°, 43.31°, 53.84°, 57.36°, 62.75°, and 74.11° corresponding to the (220), (311), (400), (422), (511), (440) and (533) faces of the crystal structure. The presence of gold yields four additional 2 theta peaks at 38.20°, 44.40°, 64.60° and 77.50° corresponding to the (111), (200), (220) and (311) faces of the metal. The unit cell constant for gold was found to be a = 4.0573 Å. XRD analysis also indicates that the stoichiometric formula of the magnetite used in these experiments is Fe_3O_4 and that the space group is Fd-3m.

Like other ferrimagnetic materials, Fe_3O_4, in the absence of a magnetic field, has a total non-zero magnetic moment made up of individual magnetic moments that are anti-parallel in orientation and unequal in magnitude. XRD analysis confirms that the magnetite used in this study has an inverse spinel structure with a unit cell constant of 8.3926 angstroms. There are 32 O^{2-} ions forming an fcc sublattice along the [111] direction within the lattice. Ferric Fe^{3+} cations fill all eight T_d sites, along with half of the O_h sites, and ferrous Fe^{2+} cations reside in the other half of the O_h sites.

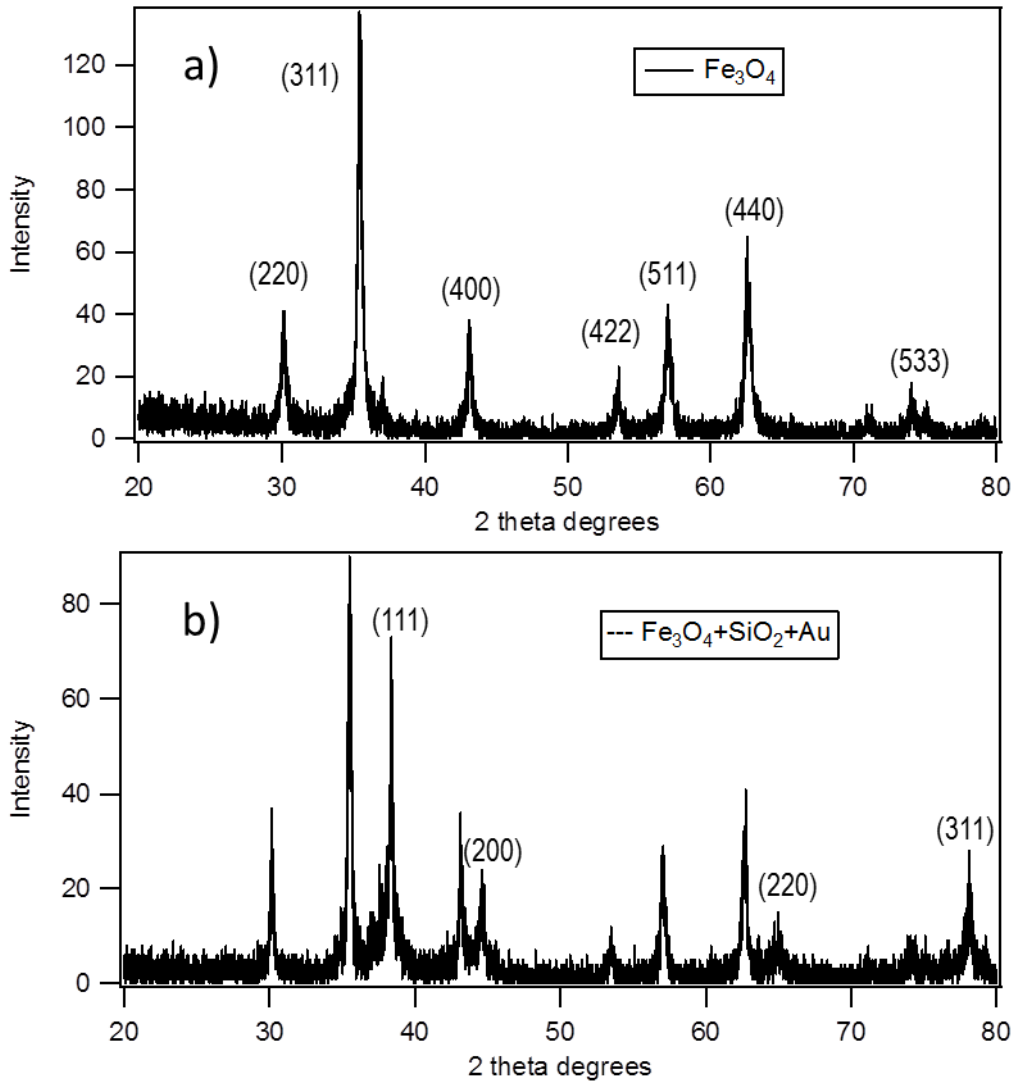

Figure 4.4: XRD spectra of a) Fe_3O_4 and b) Fe_3O_4@SiO_2+Au

4.4.2 Plasmonic and Surface Properties of Functionalized Particles

The silica shell addition, APTMS functionalization and gold+PVP functionalization were characterized using Fourier transform infrared spectroscopy (FTIR). Figure 4.5 describes the addition of silica and APTMS to the pristine magnetite. The red spectrum represents pristine magnetite, in which the first peak at

566 cm^{-1} is indicative of an Fe-O-H surface bending mode. There are also several peaks associated with surface OH bending modes located at 1054, 1634 and 3417 cm^{-1}.

The blue spectrum in Figure 4.5 represents the magnetite after addition of the SiO_2 shell. The appearance of a peak at 479 cm^{-1} is indicative of the Si-O-Si bending mode. The peak at 566 cm^{-1} for pristine magnetite shifts to 570 cm^{-1} indicative of Fe-O-Si bonding. The peak decreases significantly in intensity with the addition of the silica shell. Two additional peaks appear at 794 cm^{-1} and 1084 cm^{-1} corresponding to Si-O-Si symmetric stretching and Si-O-Si asymmetric stretching modes. The peak at 1641 cm^{-1} can be attributed to surface OH groups. The very broad peak centered ~ 3000 cm^{-1} is correlated to the addition of the silane shell and the surface OH groups associated with it.

The black spectrum in Figure 4.5 shows the addition of the APTMS linker to the silica coated magnetite. The disappearance of the peak at 479 cm^{-1} indicates surface coverage of the silane with APTMS linker. The peak at 590 cm^{-1}, which is shifted 20 cm^{-1} from the Fe-O mode at 570 cm^{-1}, indicates Fe-O-Si bending. There are two peaks corresponding to Si-O-Si symmetric and asymmetric stretch modes at 805 cm^{-1} (shifted 9 cm^{-1}) and 1075 cm^{-1} (shifted 9 cm^{-1}), respectively. There are also two peaks at 1213 cm^{-1} and 1413 cm^{-1} indicative of CN stretch and CH_2 bending modes. The peak at 1637 cm^{-1} is associated with the free NH_2 of the APTMS. The peak

centered at 3390 cm^{-1} is correlated to NH_2 indicating the presence of the APTMS linker.

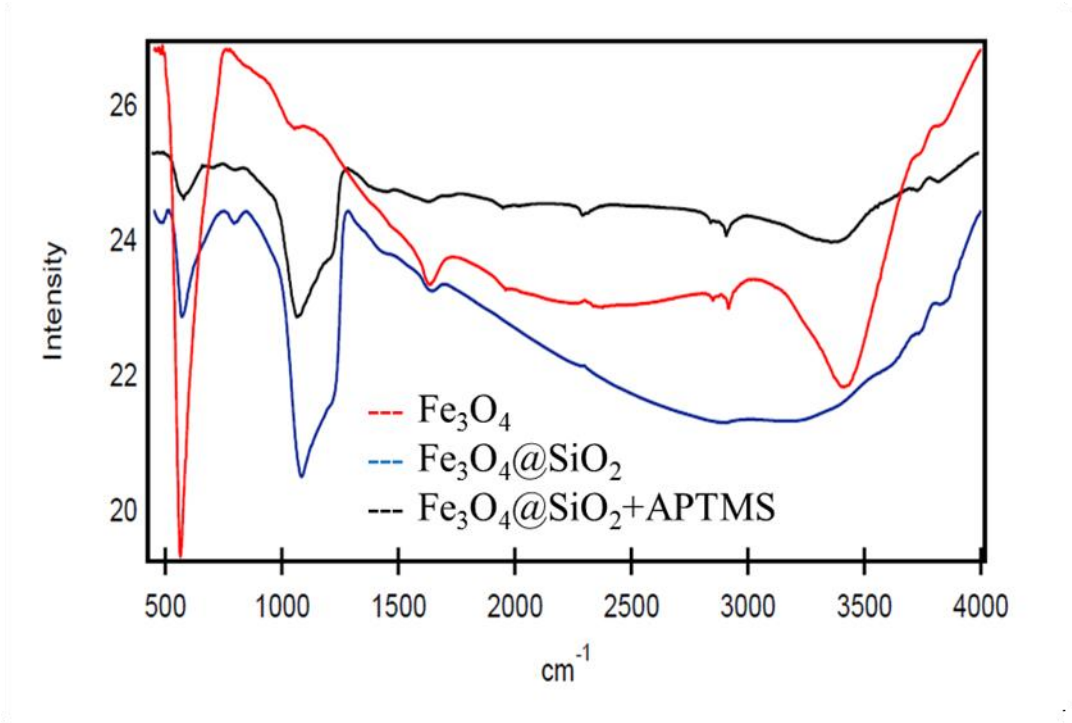

Figure 4.5: FTIR spectra for (upper-black) Fe_3O_4@SiO_2+APTMS; (middle-red) Fe_3O_4 and (lower-blue) Fe_3O_4@SiO_2.

The FTIR spectra of the magnetite nanoparticles with gold and gold plus PVP are shown in Figure 4.6. The spectrum for the APTMS functionalized ensemble is also included for reference. Once gold is added to the surface of the silica covered magnetite, the peaks associated with the APTMS sample are still observed. The 590 cm^{-1} peak representative of the Fe-O-Si bending mode is present. A new peak at 665 cm-1 is also present and can be attributed to surface OH groups due to oxidation. The two peaks associated with Si-O-Si symmetric and Si-O-Si asymmetric stretch at 799

cm^{-1} and 1071 cm^{-1} are also present, however, their intensities are reduced due to the surface coverage by gold. The peak at 1632 cm^{-1} indicative of the NH_2 bending mode is also reduced in intensity due to the surface coverage by gold. Peaks in the 2800-3000 cm^{-1} range are correlated to CH_2 symmetric and asymmetric stretching vibrations. The broad peak at ~3400 cm^{-1} is correlated to the presence of the nitrogen atom in the PVP ring.

When PVP and Au are both present at the surface of the magnetite particles there are several distinct changes. First a peak at 484 cm^{-1} appears which corresponds to the CN vibrational mode of PVP. The peak at 1465 cm^{-1} disappears while two new peaks at 1418 and 1576 cm^{-1} appear. The peak at 1418 cm^{-1} is correlated to CN vibrational mode of PVP. The peak at 1576 cm^{-1} is correlated to NH_2 vibrational mode. The peak at 1647 cm^{-1} represents the C=O vibrational mode associated with the pyrrolidone ring of PVP. The broad peak centered at ~3380 cm^{-1} is due OH groups at the surface of the particles.

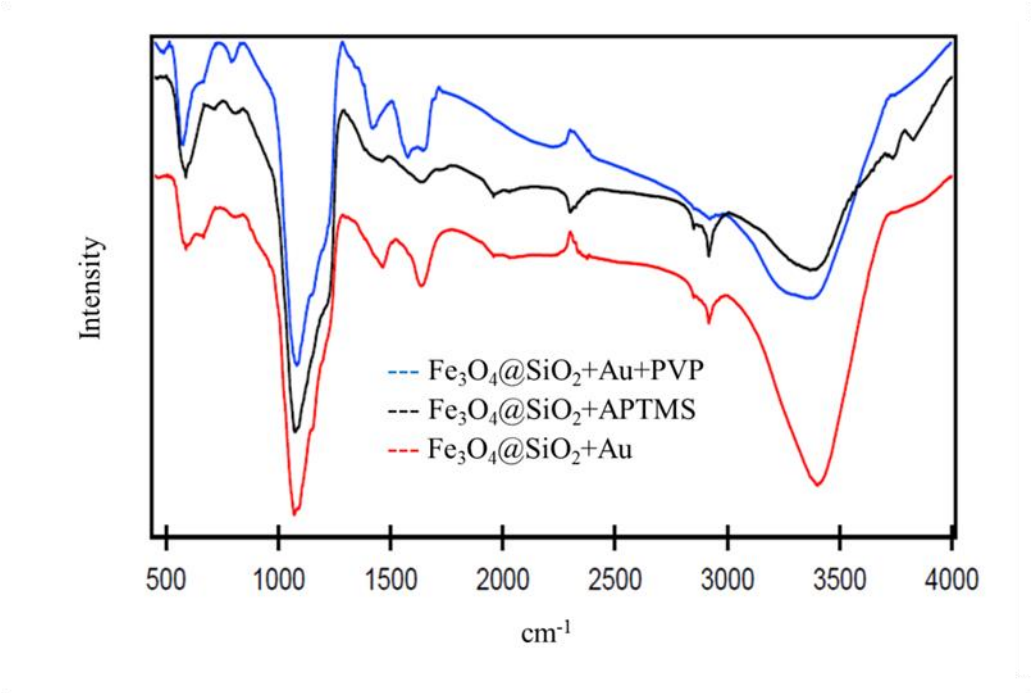

Figure 4.6: FTIR spectra for: (upper-blue) Fe_3O_4@SiO_2+Au+PVP; (middle-black) Fe_3O_4@SiO_2+APTMS and (lower-red) Fe_3O_4@SiO_2+Au.

Extinction bands are determined by particle size, shape, composition, degree of crystallinity and polydispersity within an ensemble. Therefore, any functionalization of the pristine magnetite will lead to changes in the spectrum of the material. Figure 4.7 shows extinction spectra for all four steps in the synthesis using water as a solvent. The pristine magnetite has a major excitation band at ~490 nm with a full width half maximum (FWHM) of 340 nm. Once the magnetite was functionalized with silica, the absorption peak red shifted to 545 nm (FWHM 410 nm). The ensemble functionalized with silica and the gold intermediate had an

extinction band centered at 615 nm (FWHM 555 nm) and the ensemble functionalized with gold plus PVP had a peak centered at 625 nm (FWHM 590 nm). The extinction peak for all three functionalized ensembles is red shifted from that of pristine magnetite. This red shift is attributed to the increase in particle diameter resulting from surface functionalization. The increase in FWHM for the functionalized ensembles, particularly the silica coated magnetite decorated with gold plus PVP, is due to the irregular distribution of material along the surface of the particles. It can be seen in the EM images that the surface morphology is rough and disordered. These differences between particles are known to increase the polydispersity within an ensemble which leads to a broadening of the extinction peak.[409]

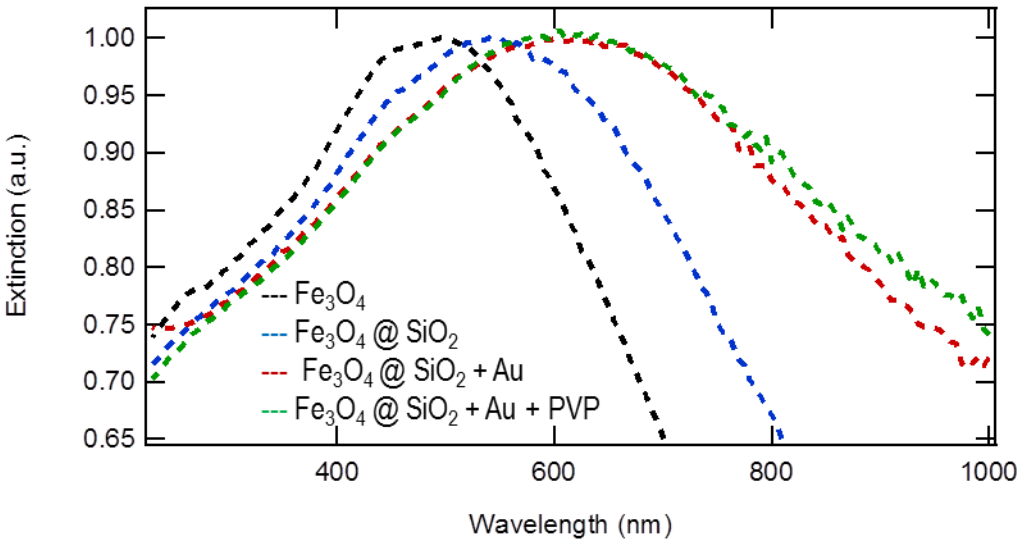

Figure 4.7: UV-Vis of (left to right): (black) bare Fe_3O_4, (blue) $Fe_3O_4@SiO_2$ intermediate, (red) $Fe_3O_4@SiO_2$+Au intermediate, (green) $Fe_3O_4@SiO_2$+Au + PVP. All spectra were taking using water as a solvent.

4.4.3 Magnetic Properties

Hysteresis loops showing the relationship between the magnetization (M) and the magnetic field (H) at RT is evident in the hysteresis loops shown in Figure 4.8. Data were obtained up to 10^4 Gauss but are shown only to ± 10000 Gauss, beyond which little change in M is observed. Magnetic saturation, corresponding to the alignment of all magnetic moments, was calculated for each ensemble and normalized to mass. Particles functionalized with SiO_2, gold and PVP obtain 68% (59.7 emu/g) of the saturated magnetic moment expected for bare magnetite on a per gram basis (90 emu/g), while the bare nanoparticles obtained 97% of the bare moment. Modified particles likely displayed a decrease in saturation due to the non-magnetic nature of the polymer and gold surface materials. This type of loss is correlated to the interruption of long range magnetic ordering induced by particle surface modification and can be observed in the EM images as the rough and disordered surface

morphology arising from the addition of the gold and polymer.

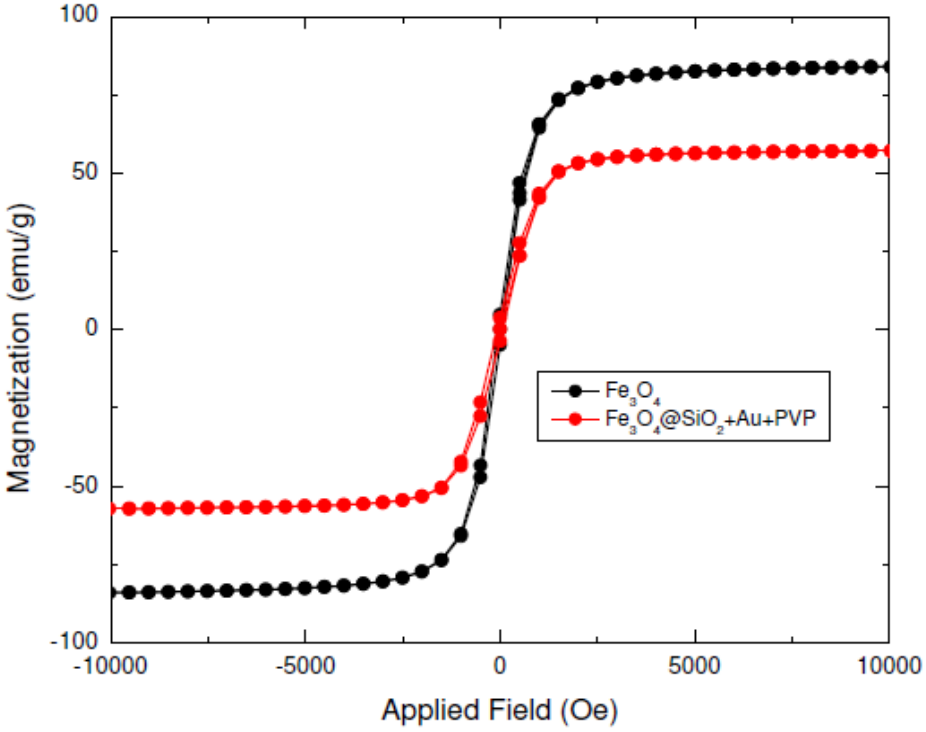

Figure 4.8: Hysteresis loops generated at RT for (upper) Fe_3O_4 and (lower) Fe_3O_4@SiO_2+Au+PVP.

To test our composite materials ability to target, bind and separate a moiety of interest we employed UV-Vis spectroscopy to characterize GLP-1 peptide bound to the Fe_3O_4@SiO_2+Au+PVP nanoparticles following reduction by TCEP and separation by magnetic induction. TCEP is a mild reducing agent which is known to reduce di-sulfide bonds over a wide range of pH conditions. Free thiols are then able to bind readily to gold through dative bonding. Once reduction and binding was complete (~30 m) the Fe_3O_4@SiO_2+Au+PVP nanoparticles were separated via

magnetic induction (`30s) and resuspended in water. Representative spectra are shown in Figure 4.9.

Fe_3O_4@SiO_2+Au+PVP nanoparticles, shown in the blue spectrum, display one broad peak centered at 700 nm. The peak is symmetric, indicative of relative homogeneity of particle size and shape within the ensemble, and has a full width half maximum (FWHM) of 395 nm. This broad FWHM is indication of the absorption of all wavelengths of light across the visible region. The GLP-1 peptide in aqueous solution, represented in the graph as the red spectrum, has one narrow peak centered at 275 nm. The black spectrum representing the GLP-1 peptide bound to the Fe_3O_4@SiO_2+Au+PVP nanoparticles post magnetic separation has two peaks. The first is a broad symmetric peak centered at 720 nm with a FWHM of 500 nm and is correlated to the Fe_3O_4@SiO_2+Au+PVP nanoparticles. The second peak is centered at 280 nm and is correlated to the bound GLP-1 peptide. The increase in FWHM and the slight red shift in SPR associated with the Fe_3O_4@SiO_2+Au+PVP peak is likely due to an increase in diameter resulting from the addition of the GLP-1 peptide to the surface of the nanoparticles. Additionally, there may be some aggregation resulting in polydispersity of the ensemble which is known to increase the FWHM.[409] The red shift in SPR associated with the bound GLP-1 peak is indicative of the molecule being attached to the surface of the Fe_3O_4@SiO_2+Au+PVP nanoparticles. The presence of the GLP-1 peak in this spectrum demonstrates that the nanoparticles are excellent in the rapid targeting and separating of a moiety of interest for bio-detection.

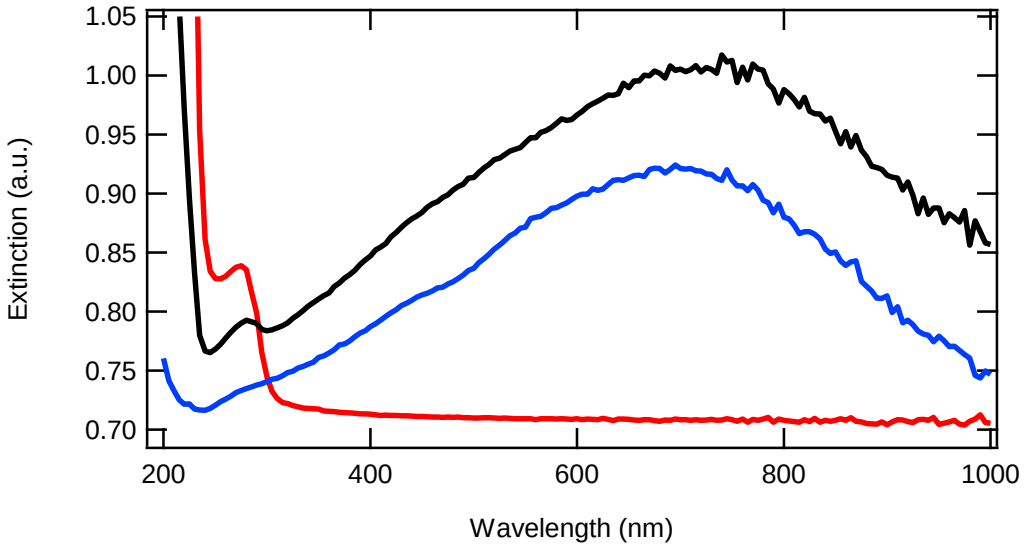

Figure 4.9: UV-Vis spectra for: (black) Fe_3O_4@SiO_2+Au+PVP nanoparticles bound to GLP-1; (blue) Fe_3O_4@SiO_2+Au+PVP nanoparticles and (red) GLP-1 in aqueous solution.

4.4.4 Surface enhanced Raman scattering (SERS) sensing

Raman spectra for (black) bare Fe_3O_4 nanoparticles and (red) Fe_3O_4@SiO_2+Au+PVP nanoparticles can be seen in Figure 4.10. Bare magnetite displays five peaks at 217, 282, 398, 489 and 595 cm^{-1}. The peak at 217 cm^{-1} describes Fe-O stretching. The peaks at 282 cm^{-1} and 398 cm^{-1} are correlated to symmetric and asymmetric Fe-O stretching respectively. The peaks at 489 cm^{-1} and 595 cm^{-1} represent Fe-O and Fe-O-Fe stretching. Once the magnetite nanoparticles have been functionalized with silica, gold and PVP two additional peaks appear at 659 and 820 cm^{-1}. The peak at 659 cm^{-1} corresponds to Si-O-Si bending modes and the peak at 820 cm^{-1} describes the C-C bond on the pyrrolidine ring in the PVP.

Additionally, the peak at 595 is shifted to 601 cm^{-1} and is correlated to Fe-O-Si stretching. It is also worth noting the effect of the SERS enhancement on the magnetite peaks which all show increased intensity due to the presence of gold.

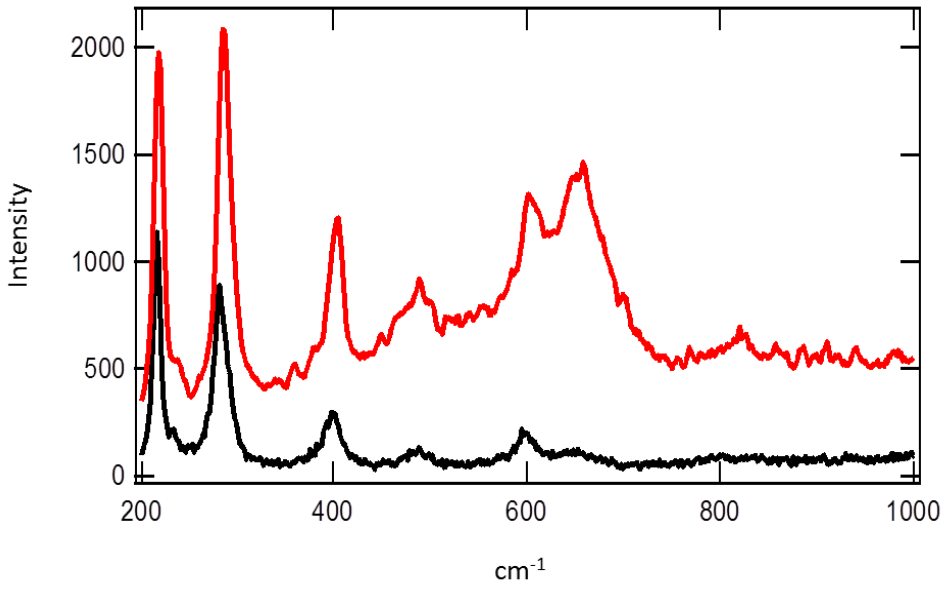

Figure 4.10: Raman spectra of bare Fe_3O_4 nanoparticles (black) and Fe_3O_4@SiO_2+Au+PVP nanoparticles (red).

Figure 4.11 shows Raman spectra for the GLP-1 peptide in aqueous solution and the SERS spectra for GLP-1 plus Fe_3O_4@SiO_2+Au+PVP nanoparticles. Even at the high concentration of 10^{-1} M, the aqueous GLP-1 solution shows poor peak resolution with only a hint of the dominant peak at ~878 cm^{-1} appearing. At lower concentrations (10^{-5} M) the spectrum is relatively flat without any peak definition. Representative SERS spectra for 10^{-3}, 10^{-5} and 10^{-7} M are also shown. The peak at ~878 cm^{-1} represents tryptophan. The doublet at ~1046 and 1085 is associated with

phenylalanine. The peak at ~1280 cm^{-1} is correlated to the amide III region and has been assigned to the alpha helix spanning the Ser^{11}-Ser-Tyr-Leu-Glu-Gly-Gln^{17} stretch of the peptide. CH deformation in the amide II region is described by the peak at ~1454 and its shoulder at ~1482 cm^{-1}. The ability of the Fe_3O_4@SiO_2+Au+PVP nanoparticles to resolve peaks at low concentrations and demonstrate a SERS enhancement factor of 2 X 10^6 is evidence of their ability to perform as a SERS substrate. While some iron oxide and gold substrates have shown comparable results, they typically rely on the use of Raman reporters or lengthy bioconjugation processes in order to target a biomolecule of interest.[410-411] Our bio-separation and bio-identification was performed rapidly (~30 m) with only a mild reducing agent, TCEP, used to encourage binding and our sensing was performed without the need for reporter molecules.

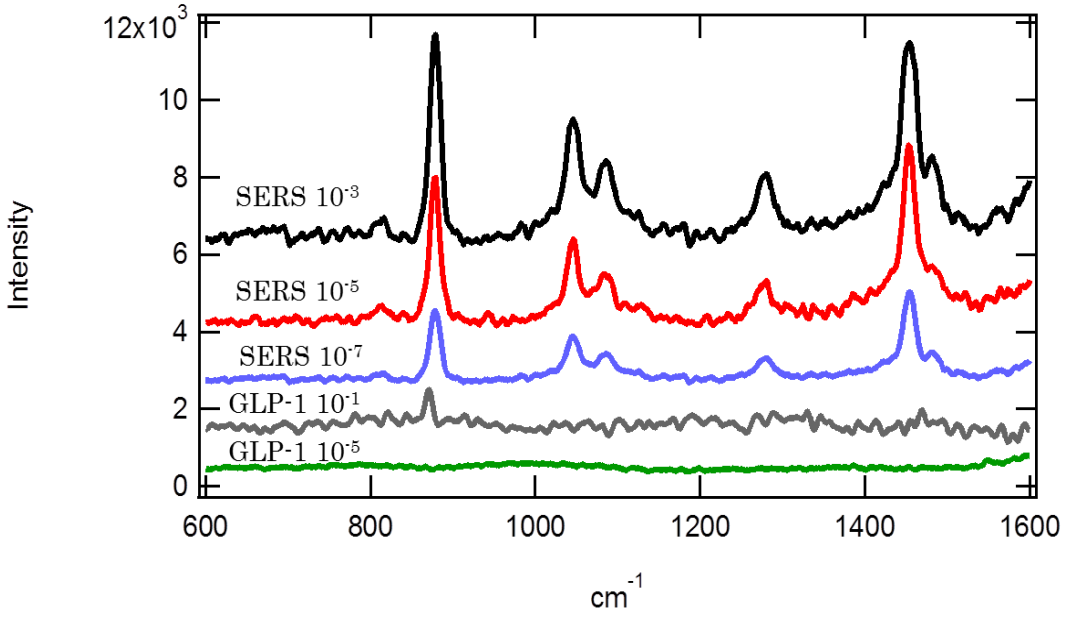

Figure 4.11: SERS spectra of GLP-1 at (black) 10^{-3} M; (red) 10^{-5} M and (blue) 10^{-7} M and Raman spectra of GLP-1 at (gray) 10^{-1} M and (green) 10^{-5} M.

4.5 Conclusion

Fe_3O_4@SiO_2 nanoparticles decorated with gold and PVP were synthesized, characterized and utilized to demonstrate sensing and bio-separation applications. The unique surface morphology comprised of roughened gold nodules was shown to be complete and uniform over the entire particle when observed by electron microscopy and HAADF imaging. These nodules, which are known to intensify the EM field of a materials surface through the generation of hot spots, make the Fe_3O_4@SiO_2+Au+PVP nanoparticles an excellent SERS substrate. When used to detect GLP-1 peptide we were able to resolve peaks of interest down to 10^{-7} M without the need for lengthy bioconjugation or Raman reporters. The ultra-thin nature of the coatings allowed for a large percentage (~68%) of the core magnetic saturation value to be maintained when compared to bare particles. The composite material was able to bind to the GLP-1 target within 30 minutes and separate the moiety from solution within 30 s under magnetic induction. The ability of this composite material to target, bind and separate a moiety of interest rapidly under magnetic induction along with being a strong plasmonic substrate for SERS makes them attractive candidates for both bio-separation and sensing applications.

Chapter Five

The Effect of Polymer and Gold Functionalization on the Magnetic Properties of Magnetite Nanoparticles

5.1 Introduction

Since the turn of the century a growing body of work has been published on chemically induced magnetism in noble metals particularly when they are embedded in a polymer matrix or capped with strong ligands.[411-418] The first to report experimental magnetism in a noble metal was Taniyama et al.[419] The authors compared Pd nanoparticles with varying diameters and found that magnetic saturation increased with decreasing particle size. They also reported a magnetic moment of 0.23 μ_B per atom for the smallest particle. Soon after, it was shown that Au nps in a polyvinylpyrrolidone (PVP) matrix exhibited a magnetic moment of 22 μ_B per particle.[448] This was attributed to a "special" spin correlation mechanism. Aside from one stand-alone paper[420] which describes 3.5 nm bare Au clusters as possessing a magnetic moment of 16 μ_B per cluster, magnetism in gold is typically due to strong interactions between the metal and a capping agent, with ferrimagnetism generally being attributed to interfacial electronic exchange which results in unpaired electrons in the 5d band of gold and a net magnetic moment. [412-413, 418-422]

In addition to facilitating magnetic behavior, polymers have been shown to increase magnetic saturation and coercivity in materials that are normally diamagnetic

in bulk, especially when strong ligands or capping agents are involved. [423,424-432] Gold, for instance, is known to have acceptor-donor type interactions with polymers, which are correlated to enhanced magnetic saturation in ensembles.[433] Polyvinylpyrrolidone (PVP) is known to form charge transfer complexes with fullerene[434-435] iodine[436] and metal nps including gold.[437-441] Jalian *et al*. observed an increase in coercivity from 210 Oe to 430 Oe for poly(vinyl alcohol) (PVA) coated $CoFe_2O_4$ particles compared to bare ensembles.[442] Thiolated sugars and monolayers of DNA have both been used to cap gold and promote magnetism via charge transfer mechanisms.[443-444] In addition to thiols other capping agents have been explored for their potential chemical inducement of magnetism in gold including amines and phosphines.[445-449] Enhancement is generally attributed to electronic interactions that result from changes in bonding, changes in coordination, and a lack of symmetry at particle surfaces.[424,450]

In this work silica coated magnetite particles (Fe_3O_4@SiO_2) functionalized with gold Fe_3O_4@SiO_2+Au), or gold plus poly (vinylpyrrolidone) (PVP) (Fe_3O_4@SiO_2+Au+PVP) were synthesized as in chapter 4. Their structural, plasmonic and magnetic properties were studied using scanning transmission electron microscopy (STEM), superconducting quantum interference device (SQUID) magnetrometry, and electron paramagnetic resonance (EPR) spectroscopy. The saturation magnetization (M_S) of particles functionalized with gold and gold plus PVP were 67.24 emu/g and 65.78 emu/g respectively. Both functionalized particles maintained a large percentage (78-80%) of their M_S values compared to pristine

magnetite. The coercivity (H_C) for pristine magnetite was 227.25 Gauss compared to 200.00 Gauss for Fe_3O_4@SiO_2+Au and 228.57 Gauss for Fe_3O_4@SiO_2+Au+PVP. Furthermore, these magnetic particles, being biologically compatible and resistant to oxidation, were functionalized with an antibody designed to target A431 oral cancer cells. The result demonstrated high specificity of binding compared to non-functionalized particles, attributable to a favorable interaction between gold and the antibody.

5.2 Experimental

5.2.1 Bioconjugation of antibody to magnetic particles

Fe_3O_4 particles decorated with gold plus PVP were prepared as outlined in chapter 4 and were bioconjugated through a two-step procedure as reported previously with some modifications.[40] First particles were functionalized by the addition of 100 μl of 1mg/ml OPSS-PEG-SVA solution to 500 μl of particles (optical density = 5.0) The functionalized particles were stirred and incubated overnight. Pegylated ensembles were washed by centrifuging for 5 minutes at 13000 rpm. 100 μl of as purchased Anti-EGFR solution was added to the washed particles and incubated for an additional 12 hours while stirring at 4 °C. The antibody conjugated particles were washed again by centrifugation for 5 minutes at 13000 rpm until no free antibody was observed in the supernatant. The final product was re-dispersed in to HBSS buffer saline solution.

5.2.2 Cell Experiment

Epidermal growth factor (EGF) overexpressing cell line (A-431) was cultured at the UCSC screening center in a 96 well plate. Cells were grown in Dulbecco's Modified Eagle's Medium (DMEM) supplemented with 10% Fetal Bovine Serum (FBS). The cell nuclei were stained using Hoechst 33342 and incubated with bioconjugated nanoparticles for one hour. Incubated cells were washed three times using HBSS saline solution, and imaged to determine binding efficiency.

5.2.3 Instrumentations and Characterization

STEM images were acquired using an FEI Quanta 3D dual beam microscope, operated at 10 kV. Samples were prepared for SEM and TEM analysis by drying Fe_3O_4 in ethanol on copper-carbon mesh grids. Magnetic properties were investigated by SQUID magnetrometry with an external magnetic field ranging from -2000 Gauss to 2000 Gauss at 10K and 300K. EPR spectroscopy was performed at 121K on a Bruker EMX spectrometer operating at an X-band frequency of 9.44 GHz using an ER 4122SHQE resonator with a 100 kHz modulation frequency, and a 5 Gauss modulation amplitude. Cell images were taken using a Leica EPI fluorescence microscope.

5.3 Discussion

Fe_3O_4@SiO_2+Au and Fe_3O_4@SiO_2+Au+PVP were prepared as described in chapter 4. Representative STEM images of both particle types are shown in Figure 5.1. The particles are spherical, monodispersed and ~200 nm in diameter. The gold coverage along the surface can be seen as the bright white spots in both 5.1 (a) and (b). The addition of gold creates small nodules which are irregular in shape and size

but uniform across the entire surface. As shown in 5.1 (b) adding more gold along with PVP generates a much thicker surface coating with even more enhanced nodules.

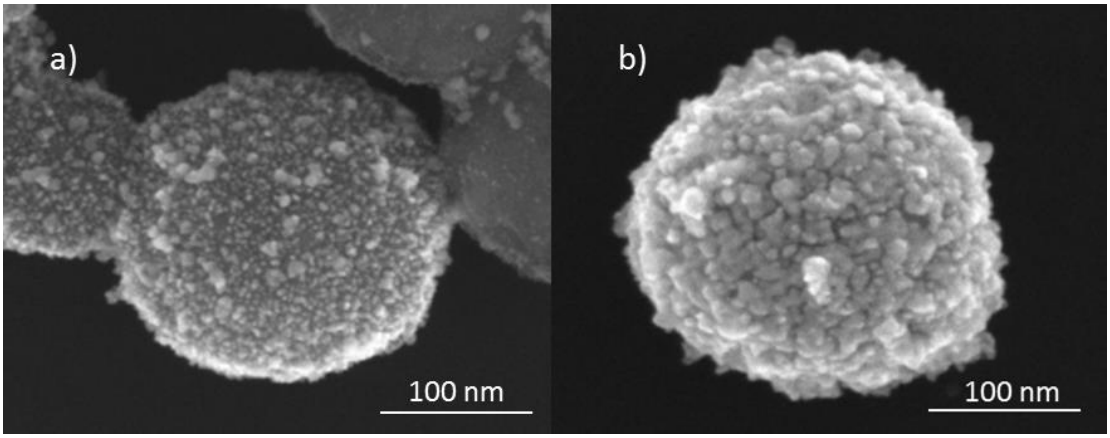

Figure 5.1: STEM images of (a) Fe_3O_4@SiO_2+Au and (b) Fe_3O_4@SiO_2+Au+PVP

Hysteresis loops showing the relationship between the magnetization (M) and the magnetic field (H) at a temperature of 10K is evident in the hysteresis loops shown in Figure 5.2. Data were obtained up to 10^4 gauss but are shown only to ± 2500 Gauss, beyond which little change in M is observed, in order to better resolve the coercive force.

Magnetic saturation, corresponding to the alignment of all atomic moments, was calculated for each ensemble and normalized to mass. All three functionalized ensembles maintained high magnetic saturation post functionalization (65.78-73.49 emu/g). Losses ranged from 13-22% of pristine magnetite's M_S value of 84.18 emu/g.

Modified particles likely displayed a decrease in saturation due to the non-magnetic nature of the polymer and gold surface materials. This type of loss is correlated to the interruption of long range magnetic ordering induced by particle surface modification and can be observed in the EM images as the rough and disordered surface morphology arising from the addition of gold and polymer.

In order to assess the magnetization of the core, we must estimate its mass from the mass of the entire nanoparticle. For the pristine Fe_3O_4 NPs, M_S is consistent with the bulk value. For Fe_3O_4@SiO_2, M_S slightly exceeds the bulk value at 10^4 Gauss by a few percent, which is likely due to uncertainty in the SiO_2 thickness. For the two ensembles with gold coatings we consider three different possible amounts of Au in the coating. For Fe_3O_4@SiO_2+Au, we consider 10 nm, 5 nm, 1.2, and 0 nm thick shells and for Fe_3O_4@SiO_2+Au+PVP we consider 10 nm, 5 nm, 2.3, and 0 nm thick shells. For a given sample mass, an assumption of a thick Au coating (10 nm) means a smaller fraction of the sample mass is in the core; hence the magnetization is produced by a smaller mass of Fe_3O_4 than if we assume a thinner effective Au coating. Since it is not possible that the Fe_3O_4 possesses a magnetization greater than the bulk MS value, this measurement can be used to place an upper bound on the effective Au layer thickness. A thickness of 1.2 nm for the Fe_3O_4@SiO_2+Au sample and a thickness of 2.3 for the Fe_3O_4@SiO_2+Au+PVP sample yields a value of MS consistent with the bulk M_S of Fe_3O_4 Since the Fe_3O_4@SiO_2 nanoparticles possessed an M_S of approximately 0.85 M_S at the same field, the thickness of the Au layer is likely less than 1.2 nm and 2.3 nm for Fe_3O_4@SiO_2+Au and Fe_3O_4@SiO_2+Au+PVP

respectively. We have also indicated the magnetization that would be obtained assuming no Au were present, which is a substantial fraction of the bulk M_S, showing that additional layers outside the SiO_2 have little, if any, effect on the moment in the core. Thus, we have succeeded in retaining a large, nearly bulk, magnetization while coating the nanoparticles with Au and Au plus PVP.

Remnant magnetization, the amount of magnetism retained after the applied field is removed, was evaluated for each ensemble. Pristine magnetite had a remanence of 0.136 emu compared to the silica coated particles of 0.045 emu. For a 1 nm thick shell, the lower bound, gold decorated silica coated magnetite had a remanence of 0.129, while ensembles functionalized with silica, gold plus PVP had a magnetic remanence of 0.114 emu.

We found that the coercive field, the amount of energy required to return the field to zero, was 227.27 Gauss for the pristine magnetite, 136.36 Gauss for the $Fe_3O_4@SiO_2$, 200.00 Gauss for the gold decorated silica coated magnetite and 228.57 Gauss for $Fe_3O_4@SiO_2$ plus gold and PVP ensemble. The enhancement found in the functionalized ensembles may be due to a reduction in dipole interactions caused by the dispersion of particles in a polymer matrix. It has been reported that when magnetic particles are embedded in non-magnetic matrixes, anisotropy and coercivity are increased.[434-436] Enhanced coercivity has also been correlated to donor acceptor relationships between Au and the free electrons associated with the pyrrolidone ring in PVP.[437-438]

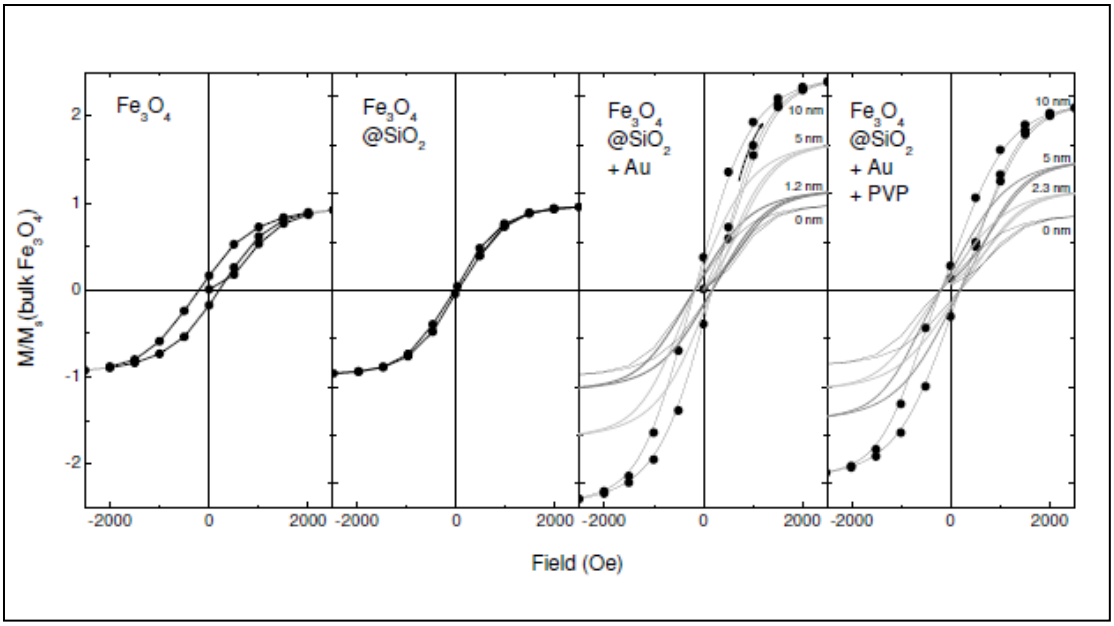

Figure 5.2: Hysteresis loops generated at 10K for: (a) Fe_3O_4; (b) $Fe_3O_4@SiO_2$; (c) $Fe_3O_4@SiO_2$+Au and (d) $Fe_3O_4@SiO_2$+Au+PVP. The data in (c) and (d) are calculated assuming a 10 nm Au layer and additional lines show the effect of different Au layer thicknesses.

Electron paramagnetic resonance (EPR) spectroscopy was employed to further investigate the magnetic properties of our particles. All samples were diluted to an optical density of 1.0 and then analyzed on a Bruker EMX spectrometer using an X-band frequency of 9.44 GHz at 121 K. EPR resonance occurs when the incident microwave radiation is equal to the energy difference between electronic spin states as they precess around the applied field and is proportional to the imaginary part of the susceptibility.[439] Resonance linewidths and height are known to depend on the magnetic free energy of the spin ensemble with the number of unpaired electronic spins being proportional to the area under the absorption curve.

Figure 5.3 shows the EPR spectra associated with the four ensembles. The peak to peak widths for each ensemble were: magnetite 1108.3 Gauss; Fe_3O_4@SiO_2 1031.9 Gauss; Fe_3O_4@SiO_2+Au 1172.7 Gauss and Fe_3O_4@SiO_2+Au+PVP 1235.5 Gauss. Maximum intensities for each sample were: magnetite 1.72 X 10^6; Fe_3O_4@SiO_2 0.94 X 10^6; Fe_3O_4@SiO_2+Au 0.92 X 10^6 and Fe_3O_4@SiO_2+Au+PVP 0.75 X 10^6.

All four samples produced the single broad spectrum associated with magnetite in literature[440] indicating that each ensemble is magnetic. However, the individual spectrums showed variation in height and width indicative of differences in the number of spin states associated with it. Line shape changes are attributed to changes in the chemical environment associated with each sample and the broadening found in each of the functionalized ensembles may be an indication that some of the magnetism is being carried by the coatings themselves. Line broadening in functionalized magnetite has also been reported to be due to the presence of surface oxyhydroxides and differences in Fe^{2+} and Fe^{3+} cations in the structural lattice.[441]

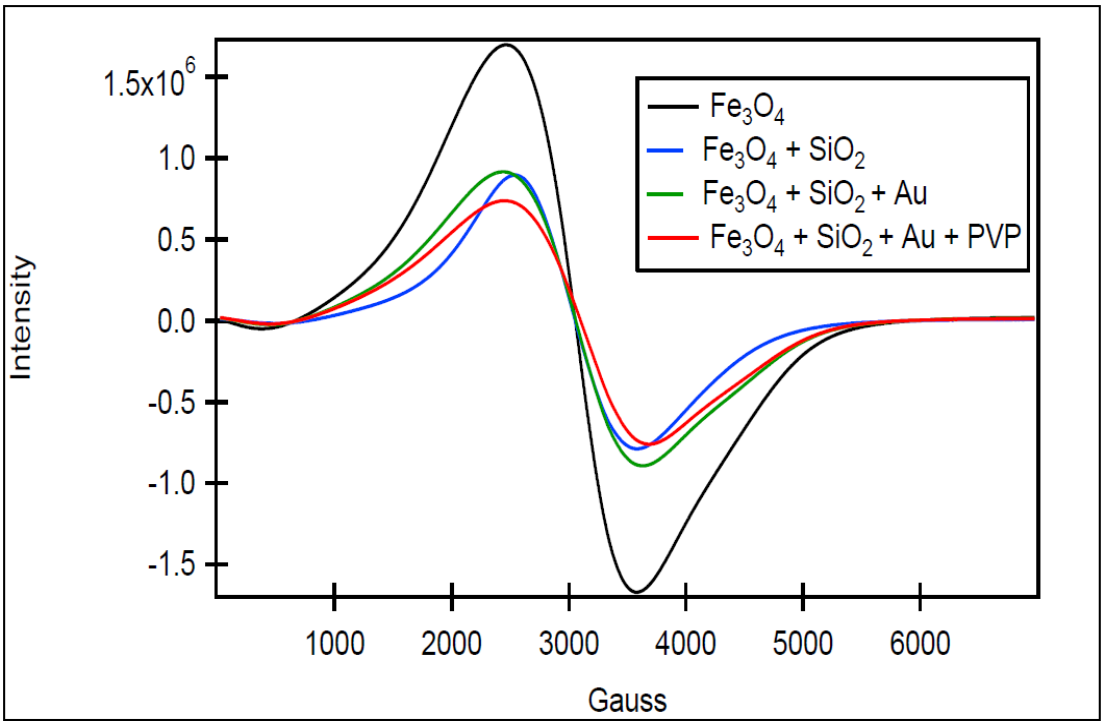

Figure 5.3: Electron paramagnetic resonance (EPR) spectra of: (black) pristine Fe_3O_4; (blue) Fe_3O4@SiO2; (green) Fe3O4@SiO2+Au and (red) Fe3O4@SiO2+Au+PVP.

Finally, in order to show that these particles are capable of binding to a specific biological moiety we performed cell experiments using the functionalized ensembles. The selective binding of functionalized magnetite ensembles is shown in Figure 5.4.

A-431 oral cancer cells are known to overexpress epidermal growth factor EGF) receptors on their surface, which can be targeted using an anti-EGFR antibody. Magnetite particles decorated with gold and gold plus PVP were conjugated with anti-EGFR targeting ligand through heterobifunctionalized PEG molecule as

described previously.[442] The cell nuclei were stained with 4',6-diamidino-2-phenylindole (Dapi), emitting at 461 nm (blue), and imaged using fluorescence microscopy as shown in Figure 5.4 (a). Strong binding to the cell receptors was observed after incubating Anti-EGFR conjugated Fe_3O_4@SiO_2+Au particles with the cells for 1 hour. Anti-EGFR targeting ligand was stained with Fluorescein isothiocyanate (FITC), emitting at 519 nm (green) for imaging purpose. The overlaid images of the cell nuclei and conjugated Fe_3O_4@SiO_2+Au particles are shown in Figure 5.4 (c). The same procedure was followed for Fe_3O_4@SiO_2+Au+PVP conjugated with anti-EGFR, However, the efficiency of bioconjugation was significantly lower due to presence of PVP on the surface of particles as shown in Figure 5.4 (d) On the other hand, non-conjugated Fe_3O_4@SiO_2+Au and Fe_3O_4@SiO_2+Au+PVP particles were completely washed away from the cells after incubation and showed no binding to the cells (Figure 5.4 b), indicating selective binding of targeting ligand to the receptors. These results suggest that magnetite functionalized with SiO_2, Au and PVP can be selectively and efficiently delivered to the tumor cells using specific targeting ligand.

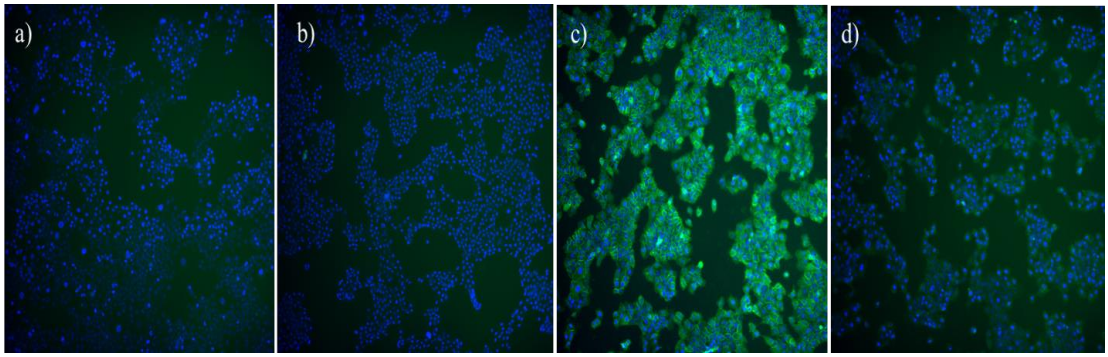

Figure 5.4: Cell images showing: a) A431 cell line stained with DAPI; b) A431 cell line plus pristine particles (no antibody); c) A431 cells (blue) and Fe_3O_4@SiO_2+Au (green) stained with FITC); d) A431 cells (blue) and Fe_3O_4@SiO_2+Au+PVP (green).

5.4 Conclusion

Magnetite particles functionalized with different combinations of silica, gold and PVP have been synthesized and characterized, with the goal to understand the effect of surface functionalization on their magnetic properties. In particular, SQUID magnetrometry measurements showed that all ensembles maintained high saturation compared to pristine magnetite. Particles functionalized with silica, gold and PVP retained 78% of the pristine Fe_3O_4 M_S while Fe_3O_4@SiO_2 and Fe_3O_4@SiO_2 +Au retained 80% and 87% respectively. Coercivity increased for the Fe_3O_4@SiO_2 +Au + PVP particles (228.57 Gauss) compared to pristine Fe_3O_4 (227.25 Gauss) and the Fe_3O_4@SiO_2+Au particles maintained 88% of pristine magnetite's coercivity, making both ensembles capable of generating thermal energy comparable to that of pristine magnetite. Additionally, the particles were shown to be effective at targeting and

binding to a biological moiety of interest making them useful in applications like bio-separation and imaging.

5.5 Future Work

The work in chapter two relied almost exclusively on the indirect evidence obtained by the characterization of the hollow gold nanospheres that were produced from the cobalt nanoparticle scaffold as opposed to direct evidence from the growth of the scaffold itself. For this reason there are some future experiments that could be performed to gain more quantitative information related to the hypotheses we provide. One strategy would involve *in situ* monitoring of the cobalt nanoparticle ensemble during the nucleation, coalescence and growth phases. This type of monitoring has been done to investigate the mechanism of growth for gold nanoparticles, particularly during coalescence.[451-452] In these investigations the authors use continuous flow small angle x-ray scattering (SAXS) with millisecond time resolution to monitor a flow cell containing their reaction fluid. They are then able to evaluate differences in nuclei formation (0.8-2 nm) during fast and slow reactions. This type of flow cell would need to be modified to prevent oxidation of the cobalt nanoparticles during the course of the reaction but would be helpful in allowing us to determine if fewer, larger seeds were being produced post reduction during nucleation as a result of the decrease in reagent concentration. Additionally, we could gain some direct evidence related to the kinetics of the nucleation period,

specifically the length of time involved in seed coalescence once citric acid is added to the reduced cobalt salt.

Other techniques that could be used to quantify the growth of cobalt nanoparticles are UV-Vis and dynamic light scattering. Although we did make efforts to use both characterization techniques in our research, cobalt is highly sensitive to oxidation and the particles would often oxidize within minutes to CoO before any data could be acquired. Again, the construction of a vessel that would prevent oxidation would be helpful in maintaining the integrity of the cobalt nanoparticles for the length of time required to take measurements on either instrument.

In the work described in chapter 4 although we bound our target analyte, GLP-1, to our substrate in order to demonstrate our ability to separate a moiety of interest from solution, we did not bind the analyte to our substrate prior to performing SERS spectroscopy. Doing so would have resulted in a larger percent of the ensemble population being in the near field of the substrate surface and would have enhanced the Raman signal significantly. A future experiment would involve targeting, binding and separating a moiety of interest and then immediately characterizing the analyte using SERS. This would likely enhance the SERS signal by at least two orders of magnitude.

In chapter five the initial purpose of functionalizing Fe_3O_4@SiO_2 with PVP and Au was to take advantage of both the magnetic and plasmonic properties of the magnetite and noble metal. We also wanted to determine if the interaction between

the gold and polymers facilitated the enhancement of magnetic properties associated with the material. While we were able to see encouraging results from the SQUID and EPR data, we were unfortunately not able to sufficiently determine experimentally where the magnetic enhancement in our material was coming from. The use of X-ray absorption near edge structure (XANES) spectroscopy would be helpful in allowing us to evaluate changes in the hole density of the 5d band of gold resulting from exchange mechanisms between the metal and the polymers.[421,445,453-454] We feel this final experiment would allow us to tell a more complete story with respect to this uniquely synthesized material.

References

1. Kreibig, U., Vollmer, M. *Optical Properties of Metal Clusters.* Springer, Berlin. 1995.

2. El-Sayed, M.A. *Acc. Chem. Res*. 34 (2001) 257.

3. Majer, S.A., Atwater, H.A. *J. Appl. Phys.* 98(2005)011101.

4. Anker, J.N., Hall, W.P., Lyandres, O., Shah, N.C., Zhao, J., Van Dyne, R.P. *Nat. Mater.* 7(2008)442.

5. Jain, P.K., Huang, X., El-Sayed, I.H., El-Sayed, M.A. *Acc. Chem. Res*. 41(2008)15878.

6. Blaber, M.G., Arnold, M.D., Ford, M.J. *J. Phys. Cond. Matter*. 22(2010)143201

7. Gramothev, D.K., Bozhevolnyi, S.I. *Nat. Photon.* 4(2010)83.

8. Prodan, E., Radloff, C., Halas, N.J., Nordlander, P. *Science.* 302(2003)419.

9. Halas, N.J., Lal, S., Chang, W.S., Link, S., Nordlander, P. *Chem. Rev.* 111(2011)3913..

10. Schuller, J.A., Barnard, E.S., Cai, W., Jun, Y.C., White, J.S., Brogersma, M.L. *Nat. Mater*. 9(2010)193.

11. Kumar, G.V.P. *Nanophotonics* 6(2012)064503.

12. Liz-Marzan, L.M., Murphy, C.J., Wang, J. *Chem. Soc. Rev*. 43(2014)3820

13. Meinyk, A.R., Harrison, M.J. *Phys. Rev. B* 2(1970)835

14. Link, S., El-Sayed, M.A. *Int. Rev. Phys. Chem.* 19(2000)409

15. Miller, M.M., Lazarides, A.A. *J. Phys. Chem. B* 109(2005)21556

16. Kelly, K.L., Coronado, E., Zhao, L.L., Schatz, G.C. *J. Phys. Chem. B* 107(2003)668

17. Liz-Marzan, L.M. *Materials Today* Feb. 2004 ISSN: 1369 7021

18. Sonnichsen, C., Franzl, T., Wilk, T., von Plessen, G., Feldman, J., Wilson, O., Mulvaney, P. *Phys. Rev. Lett.* 88(2002)077402

19. Koenderink, A.F., Polman, A., *Phys. Rev. B* 74(2006)033402

20. Miller, M.M., Lazarides, A.A., *J. Optics A. Pure Appl. Optics* 8(2006)S239

21. Feis, A., Gellini, C., Remingo-Salir, P., Becucci, M. *Photoacoustics* 2(2014)47

22. Faraday, M. *Phil. Trans. R. Soc. Lond.* 147(1857)145

23. Mie, G., *Annalen der Physik* 330(1908)377

24. Wokaun, A., Gordon, J.P., Liao, P.F. *Phys. Rev. Lett.* 48(1982)957

25. Meier, M., Wokaun, A. *Opt. Lett*. 8(1983)581

26. Graaff, R., Aarnoudse, J.G., Yup, J.R., Sloot, P.M.A, del Mul, F.F.M., Greve, J., Kollink, M.H. *Appl. Optics* 31(1992)1370

27. Horvath, H. *J. Quant. Spectroscopy & Radiative Transfer* 110(2009)787

28. Fu, Q., Sun, W. *Appl. Optics* 40(2001)1354

29. Jain, P., Huang, X., El-Sayed, I. H., El-Sayed, M.A. *Plasmonics* 2(2007)107

30. Ashcroft, *Solid State Physics*. Holt Rinehart and Winston, New York. 1976

31. Hovel, H., Fritz, S., Hilger, A., Kreibig, U., Vollmer, M. *Phys Rev. B* 48(1993)18178

32. Link, S., El-Sayed, M.A. *Ann. Rev. Phys. Chem* 54(2003)331

33. Kolwas, K., Derkachova, A. J. *Quant. Spectrosc. Rad. Transfer* 114(2013)45

34. Langer, J., Novikov, S.M., Liz-Marzan, L.M. *Nanotechnol* 26(2015)322001

35. Link, S., El-Sayed, M.A. *J. Phys. Chem B* 103(1999)4212

36. Arbouet, C., Voisin, D., Christofilos, P., Langot, N., Del Fatti, F., Vallerr, J., Lerme, G., Celep, E., Cottancin, M. Gaudry, M. Pellarin, M. Broyer, M. Maillard, M.,. Pileni, P., Treguer, M. *Phys. Rev. Lett.* 90(2003)1774011

37. Nehl, C.L., Grady, N.K., Goodrich, G.P,, Tam, F., Halas, N.J. Hafner, J.H. *Nano Lett.* 4(2004)2355

38. Jain, P.K., Lee, K.S., El-Sayed, I.H., El-Sayed, M.A. *J. Phys. Chem. B* 110(2006)7238

39. Liz-Marzan, L.M. *Langmuir* 22(2006)32

40. Wang, H., Brandl, D.W., Nordlander, P., Halas, N.J. *Acc. Chem. Res.* 40(2007)53

41. Pelto, M., Aizpurva, J., Bryant, G. *Laser and Photonics Reviews* 2(2008)136

42. Zhang, J.Z., Noguez, C. *Plasmonics* 3(2008)127

43. Grzelczak, M., Liz-Marzan, L.M. *Chem. Soc. Rev*. 43(2012)2089

44. Xie, H., Larmour, A., Smith, W.E., Faulds, K., Graham, D. *J. Phys. Chem. C.* 116(2012)8338

45. Cao Jr., R., Diaz-Garcia, A.M., Cao, R. *Coordination Chem. Rev*. 253(2009)1262

46. Mock, J.J., Barbic, M., Smith, D.R., Schultz, D.A., Schultz, S. *J. Chem. Phys.* 116(2002)6755

47. Coronado, E.A., Shatz, G.C. *J. Chem. Phys.* 119(2003)3926

48. Burda, C., Chen, X., Narayanan, R., El-Sayed, M.A. *Chem. Rev.* 105(2005)1025

49. Eustis, S., El-Sayed, M.A. *Chem. Soc. Rev*. 35(2006)209

50. Lee, K., El-Sayed, M.A. *J. Phys. Chem. B* 110(2006)19220

51. Perez-Juste, J., Pastoriza-Santos, I., Liz-Marzan, L.M., Mulvaney, P. *Coordination Chem. Rev.* 249(2005)1870

52. Gomez, D.E., Vernon, K.C., Davis, T. *J. Phys. Rev. B* 81(2010)075414

53. Zhang, J.Z. J. *Phys. Chem. Lett*. 1(2010)686

54. Lee, K.S., El-Sayed, M.A. *J. Phys. Chem. B* 109(2005)20331

55. Huang, X., El-Sayed, M.A. *J. Adv. Res.* 1(2010)13

56. Schwartzberg, A.M., Grant, C.D., Wolcott, A., Talley, C.E., Huser, T.R., Bogomolni, R., Zhang, J.Z. *J. Phys. Chem. B* 108(2004)19191

57. Grant, C., Norman Jr.,C.T., Morris, T., Syulczenski, G., Zhang, J.Z. *SPIE Proc.* 4807(2002)216

58. Albella, P., Garcia-Cuento, B., Gonzalez, F., Moreno, F., Wu, P.C., Kim, T.H., Brown, A., Yang, Y., Everitt, H.O., Videen, G. *Nano Lett*. 11(2011)3531

59. Loo, C., Lin, A., Hirsch, L., Lee, M.H., Barton, J., Halas, N.J., West, J., Drezek, R. *Technol. Cancer Res. Treatment* 3(2004)33

60. Hirsch, L.R., Gobin, A.M., Lowery, A.R., Tam, F., Dreyek, R.A. Halas, N.J., West, J. *Annals. Biomed. Eng.* 34(2006)15

61. Kalele, S., Gosavi, S.W., Wiban, J., Kulkarni, S.K. *Current Sci.* 91(2006)1038

62. Cole, J.R., Mirin, N.A., Knight, M.W., Goodrich, G.P., Halas, N.J. *J. Phys. Chem. C* 113(2009)12090

63. Amiens, C., Ciuculescu-Pradines, D., Philippot, K. *Coordination Chem. Rev.* 308(2016)409

64. Michaels, A., Jiang, M., Brus, L. *J. Phys. Chem. B.* 104(2000)11965

65. McFarland, A.D., Young, A., Dieringer, J.A., Van Duyne, R.P. *J. Phys. Chem. B.* 109(2005)11279

66. Schwartzberg, A.M., Olson, T.Y., Talley, C.E., Zhang, J.Z. *J. Phys. Chem. B* 110(2006)19935

67. Cheong, W.F., Prahl, S.A., Welch, A.J. *J. Quantum Electronics* 26(1990)2166

68. Habash, R.W., Bansal, R., Krewski, D., Alhafid, H.T. *Crit. Rev. Biomed. Eng.* 34(2006)459

69. Sokolov, K., Follen, M., Aaron, J., Pavlova, I., Malpica, A., Lotan, R., Richards-Kortum, R. *Cancer Res*. 63(2003)1999

70. Chithrani, B.D., Ghazani, A.A., Chan, W.C.W. *Nano Lett.* 6(2006)662

71. Chithrani, B.D., Chan, W.C.W. *Nano Lett.* 7(2007)1542

72. Lu, W., Xiong, C., Zhang, G., Huang, Q., Zhang, R., Li, C. *Clin. Cancer Res.*15(2009)876

73. Douglas, P., Stokes, R.J., Graham, D., Smith, W.E. *Analyst* 133(2008)791

74. Conner, E.E., Mwamuka, J., Gole, A., Murphy, C.J., Wyatt, M.D. *Small* 1(2005)325

75. Liang, H.P., Wan, L.J., Bai, C.L., Jiang, L. *J. Phys. Chem. B* 109(2005)7795

76. Preciado-Flores, S., Wang, D., Wheeler, D.A., Newhouse, R., Hensel, J.K., Schwartzberg, A.M., Wang, L., Zhu, J., Barboza-Flores, M., Zhang, J.Z. *J. Mater. Chem*. 21(2011)2344

77. Adams, S.A., Thai, D., Mascona, X., Schwartzberg, A.M., Zhang, J.Z. *Chem. Mater.* 26(2014)6805

78. Melancon, M.P., Lu, W., Yang, Z., Zhang, R., Cheng, Z., Elliot, A.M., Stafford, J., Olson, T., Zhang, J.Z. *Mole. Cancer Ther.* 7(2008)1730

79. Braun, G.B., Pallaoro, A, Wu, G., Missirlis, D., Zasadzinski, J.A., Tirrell, M., Reich, N.O. *ACS Nano* 3(2009)2007

80. You, J., Zhang, R., Zhang, G, Zhong, M., Liu, Y., Van Pelt, C.S., Liang, D., Wei, W., Sood, A.K., Li, C. *J. Control. Release* 158(2012)319

81. Sun, Y., Xiz, Y., *Nano Lett*. 3(2003)1569

82. Hao, E. Li, S.Y., Bailey, R.C., Zhou, S.L., Schatz, G.C., Hupp, J.T. *J. Phys. Chem. B* 108(2004)1224

83. Pena, O., Pal, U., Rodriquez-Fernandez, L., Crespo-Sosa, A. *J. Opt. Soc. Am. B* 108(2004)1224

84. Wu, L., Wang, Z., Zong, S., Huang, Z., Zhang, P., Cui, Y. *Biosensors Bioelectron*. 25(2009)826

85. del Fatti, N., Valle, F., Flytazanis, C., Hammanaka, Y., Nakamura, A. *Chem Phys.* 251(2000)215

86. Nappa, J. Revillod, G., Russier-Antoine, I., Benichous, E., Honin, C. Brevit, P.F. *Phys. Rev. B* 71(2005)165407

87. Mulvaney, P. Giersig, M., Ung, T., Liz-Marzan, L.M. *Adv. Mater* 9(1997)570

88. Ung, T., Liz-Marzan, L.M., Mulvaney, P. *Langmuir* 14(1998)3740

89. Caruso, R., Antonietti, M. *Chem. Mater*. 13(2001)3272

90. Caruso, F., Caruso, R.A., Mohwald, H. *Science* 282(1998)1111

91. Sun, Y., Mayers, B., Xia, Y. *Nano Lett.* 2(2002)481

92. An, K., Hyeon, T. *Nano Today* 3(2009)359

93. Chah, S., Fendler, J.H., Yi, *J. Colloid Interface Sci.* 250(2002)142

94. Liang, Z., Susha, A., Caruso, F. *Chem Mater*. 15(2003)3176

95. Abdolli, S.N., Naderi, M., Amoabediny, G. *Colloids Surf. A: Physiochem. Engineer. Aspects* 436(2013)1069

96. Chen, J., Wiley, B., McLellan, J., Xiong, Y., Li, Z.Y., Xia, Y. *Nano Lett*. 5(2005)2058

97. Fan, X., Zheng, W., Singh, D.J. *Light: Sci. Appl*. 3(2014)e179

98. Gonzalez, E., Arbiol, J., Puntes, V.F. *Science* 334(2011)1377

99. Choi, M.R., Stanton-Maxey, K.J., Stanely, J.K., Levin, C.S., Bardhan, R., Akin, D., Badye, S., Sturgis, J., Robinson, J.P., Bashir, R., Halas, N.J., Clare, S.E. *Nano Lett.* 7(2007)3759

100. Wang, Z.L., Ahmad, T.S., El-Sayed, M.A. *Surface Sci.* 380(1997)302

101. Hong, X., Wang, D., Cai, S., Rong, H. Li, Y., *J. Amer. Chem. Soc.* 134(2012)18165

102. Goris, B., Polavarapu, L., Bals, S., Tendeloo, G.V. Liz-Marzan, L.M. *Nano Lett.* 14(2014)3220

103. Oh, M.H., Yu, T., Yu, S., Lim, B., Ko, K., Willinger, M., Seo, D., Kim, B., Cho, M., Park, J., Kang, K., Sung, Y., Pinna, N., Hyeon, T. *Science* 340(2013)964

104. Xia, X., Wang, Y., Ruditsky, A., Xia, Y. *Adv. Matter*. 25(2013)6313

105. Kirkendall, *Trans. AIME* 171(1947)130

106. Tu, K.N., Gosels, U. *Appl. Phys. Lett.* 86(2005)093111

107. Yin, Y., Rioux, R.M., Erdonmez, C.K., Hughes, S., Somorjai, G.A., Alvisatos, A.P. *Science* 304(2004)711

108. Sun, Y., Xia, Y. *Science* 298(2002)2176

109. Liu, J., Bu, W., Pan, L., Shi, J. *Angewandte Chemie Int. Ed*. 52(2013)4375

110. Lisiecki, I., Pileni, M.P. *Langmuir* 19(2003)9486

111. Kobayashi, Y., Horie, M., Konno, M. Rodriguez-Gonzalez, B., Liz-Marzan, L.M. *J. Phys. Chem. B* 107(2003)7420

112. Xia, Y., Xiong, Y., Lim, B., Skrabalak, S.E. *Angew Chem. Int. Ed. Eng*. 48(2009)60

113. Grzelczak, M., Liz-Marzan, L.M. *Chem. Soc. Rev*. 43(2014)2089

114. Salgueirino-maceira, V., Correa-Duarte, M.A., Farle, M., Lopez-Quintelz, M.A., Sieradzki, K., Diaz, R. *Langmuir* 22(2006 374

115. LaMer, V.K., Dinegar, R.H. *J. Amer. Chem. Soc*. 72(1950)4847

116. Jana, N.R., Gearheart, L., Murphy, C.J. *Langmuir* 17(2001)6782

117. Zeng, J., Huang, J., Lu, W., Wang, X., Wang, B., Zhang, S., Hou, *J. Adv. Mater*. 19(2007)2172

118. Jackson, J.B., Wescott, S., Hirsch, L.R., West, J.L., Halas, N.J. *J. Appl. Phys. Lett.* 82(2003)257

119. Huang, C., Hao, Y., Nyagilo, J., Dave, D.P., Xu, L., Sun, X. *J. Nano Res*. 10(2010)137

120. Sanchez-Gaytan, B.L., Qian, Z., Hastings, S.P., Rica, M.L., Fakhraai, Z., Park, S.J. *J. Phys. Chem.* 117(2003)8916

121. Shi, W., Casas, J., Venkatarmasubramani, M., Tang, L. *ISRN Nanomaterials* 2012 article I.D. 659043

122. Meng, Q., Li, H., Yang, H. *Chinese J. Chem.* 28(2010)2015

123. Pu, Y.C., Song, F., Zhang, W., Lindley, S., Adams, S.A., Zhang, J.Z. *Particle Particle Syst. Characterization* 34(2017)160025

124. Peng, *Metallic Nanomaterials.* Wiley VCH, Verlag Weinheim Germany 2009 vol. 1

125 Park, J., Joo, J., Kwon, S.G., Jang, Y., Hyeon, T. *Angew Chem Int. Ed.* 46(2007)4643

126. Rodriquez-Fernandez, J., Funston, A.M., Perez-Juste, J., Alvarez-Puebla, R.A., Liz-Marzan, L.M., Mulvaney, P. *Phys. Chem. Chem. Phys.* 11(2009)5909

127. Bao, Y., An, W., Turner, H., Krishnam, K.M. *Langmuir* 26(2010)478

128. Yang, Z., Yang, N., Yang, J., Bergstrom, J., Pileni, M.P. *Adv. Funct. Mater.* 25(2015)891

129, Albrecht, M.G., Creighton, J.A. *J. Amer. Chem. Soc*. 99(1977)5215

130. Jeanmaire, D.L., Van Duyne, R.P. *J. Electranal. Chem*. 84(1977)5215

131. Moskovits, M.J. *J. Chem. Phys*. 69(1978)4159

132. Blatchford, C.G., Campbell, J.R., Creighton, *J.A. Surface Sci*. 120(1982)435

133. Otto, A., Mrozck, I., Grabhorn, H., Kemann, W.A. *J. Phys. Condens. Mater*. 4(1992)1143

134. Campion, A., Kambhampati, P. *Chem. Soc. Rev*. 27(1998)241

135. Kneipp, K.H., Kneipp, I., Itzkan, I., Dasari, R.R., Feld, M.S. *J. Condens. Mater*. 14(2002)R597

136. Nikoobakht, B. *J. Phys. Chem. A* 107(2003)3372

137. Stiles, P.L., Dieringer, J.A., Shah, N.C., Van Duyne, R.P. *Ann. Rev. Anal. Chem.* 1(2008)601

138. Fan, M., Andrade, G.F.S., Brolo, A.G. *Analytica Chimica Acta* 693(2011)7

139. Vendrell, M., Marti, K.K., Dhaliwal, K., Chang, Y.T. *Trends Biotechnol.* 31(2013)249

140. Moskovits, M. *Rev. Mod. Phys.* 57(1985)783

141. Nie, S., Emory, S.R. *Science* 275(1997)1102

142. Jian, K.B., Maillared, M., Brus, L. *J. Phys. Chem. C.* 112(2008)10323

143. Schwartzberg, A.M., Zhang, J.Z. *J. Phys. Chem. C* 112(2008)10323

144. Fang, Y., Song, N.H., Dlott, D.D. *Science* 321(2008)388

145. Creighton, J.A., Blatchford, C.G., Albrecht, M.G. *J. Chem. Soc. Faraday Trans*. 275(1979)790

146. Quinten, M. *J. Clust. Sci*. 10(1999)319

147. Wang, Y., Yan, B., Chen, L. *Chem. Rev*. 113(2013)11391

148. Moskovits, M. *Rev. Mod. Phys.* 57(1985)783

149. Kahraman, M., Yazici, M.M., Sahin, F., Bayrak, O.F., Culha, M. *Apl. Spectrosc.* 61(2007)479

150. Stamplecoski, K.G., Scaiano, J.C. *J. Phys. Chem. C.* 115(2011)1403

151. Sharma, B., Frontiera, R.R., Henry, A.I., Ringe, E., Van Duyne, R.P. *Materials Today* 15(2012)16

152. Kneipp, K., Kneipp, H., Kneipp, J. *Acc. Chem. Res.* 39(2006)443

153. Lee, S., Kim. S., Choo, J., Shin, S.Y., Lee, Y.H., Choi, H.Y., Ha, S., Kang, K., Oh, C.H. *Anal. Chem. Res.* 79(2007)916

154. Qian, X., Peng, X.H., Ansari, D.O., Yin-Goen, Q., Chen, G.Z., Shin, D.M., Yang, L., Young, A.N., Wang, M.D., Nie, S. *Nature. Biotechnol.* 26(2008)83

155. Rivas, L., Sanchez-Cortez, S., Garcia-Ramos, J.V., Morcillo, G. *Langmuir* 16(2000)9722

156. Tiwari, V.S., Oleg, T., Darbha, G.K., Hardy, W., Singh, J.P., Ray, P.C. *Chem. Phys. Lett.* 444(2007)

157. Lee, S., Chon, H., Lee, M., Choo, J., Shin, S.Y., Lee, Y.H., Rhyu, I.J., Son, S.W., Oh, C.H. *Biosensors Bioelectronics* 24(2009)2260

158. Schwartzberg, A.M., Oshiro, T.Y., Zhang, J.Z., Huser, T., Talley, C.E. *Anal. Chem.* 78(2006)4732

159. Laurence, T.A., Braun, G., Talley, C., Schwartzberg, A., Moskovits, M., Reich, N., Huser, T. *J. Amer. Chem. Soc*. 131(2008)162

160. Quinten, M. *J. Cluster Sci*. 10(1999)319

161. Cox, B., Laufer, J.G., Arridge, S.R., Beard, P.C. *J. Biomed. Opt*. 6(2012)061202

162. Ashwell, G.J., Leeson, P., Bahra, g.S., Brown, C.R. *J. Opt. Soc. Am. B* 15(1998)484

163. Galletto, P., Girault, H.H., Gomis-Bas, C., Schriffin, D.J., Antoine, R., Broyer, M. Brevet, P.F. *J. Physics Cond. Mater,* 19(2007)375108

164. Chen, C.K., de Castro, A.R.B., Shen, Y.R. *Phys. Rev. Lett.* 46(1981)2

165. Perez-Gonzalez, O., Zabala, N., Borisov, A.G., Halas, N.J., Nordlander, P., Aizpurua, J. *Nano Lett.* 10(2010)3090

166. Slaughter, L.S., Wu, Y., Willingham, B.A., Nordlander, P., Link, S. *ACS Nano* 4(2010)4657

167. Song, P., Nordlander, P., Gao, S. *J. Chem. Phys*. 134(2011)074701

168. Prodan, E., Radloff, C., Halas, N.J., Nordlander, P. *Science* 302(2003)419

169. Gunnarso, L., Rindzevicius, T., Prinkulis, J., Kasemo, B., Kall, M., Zhou, S., Schatz, G.C. *J. Phys. Chem. B* 109(2005)1079

170. Shuck, P.J., Fromm, D.F., Sundaramurthy, A., Kino, G.S., Moerner, W.E. *Phys. Rev. Lett*. 94(2005)1079

171. Romero, I., Aizpurua, J., Bryant, G.W., Garcia de Abajo, F.J. *J. Opt. Express* 14(2006)9988

172. Xu, H., Bjerneld, E.J., Kall, M., Borjesson, L. *Phys. Rev. Lett*. 83(1999)4357

173. Chandra, M., Dowgiallo, A.M., Knappenberger Jr., K.L. *J. Phys. Chem. C* 114(2010)19971

174. Tiggesbaumker, J., Koller, L, Meiwes-Broer, K.H., Liebsch, A. *Phys. Rev. A* 48(1993)1749

175. Prodan, E., Nordlander, P. *Chem. Phys*. 120(2004)5444

176. Knappenberger, K.L., Schwartzberg, A.M., Dogliallo, A.M., Lowman, C.A. *J. Amer. Chem. Soc*. 131(2009)13892

177. Mahmoud, M.A., El-Sayed, M.A. *J. Phys. Chem. C* 114(2010)7436

178. Nappa, J. Russier-Antoine, I., Benichou, E., Jonin, C., Brevet, P.F. *J. Chem. Phys.* 125(2006)184712

179. Hoelen, C.G.A., de Mul, F.F.M., Pongers, R., Dekker, A. *Opt. Lett*. 23(1998)648

180. Ntziachristos, V. *Nature Methods* 7(2010)603

181. Weissleder, R. *Nature Rev. Cancer* 2(2002)11

182. Wang, X.D., Pang, Y.J., Ku, G., Xie, X.Y., Soica, G., Wang, L.H.V. *Nature Biotechnol.* 21(2003)80034

183. Ermilov, S.A., Khamapirad, T., Conjusteau, A., Leonard, M.H., Lacewell, R., Menta, K. *J. Biomed. Opt*. 14(2009)024007

184. Chen, Y.S., Frey, W., Kim, S., Homan, K., kruizinga, P., Sokolov, K., Emelianov, S. *Optics Express* 18(2010 8867

185. He, X., Wang, K., Cheng, Z. *Nature Biotechnol*. 22(2006)339

186. Debbage, P., Jaschke, W. *Histo. Chem Cell, Biol*. 130(2008)845

187. Altinonglue, E., Adair, J.H., *Naomed. Nanobiotechnol.* 2(2010)461

188. Blasiak, B., Van Veggel, F.C.J.M., Tomanek, B. *J. Nanomaterials* 2013 Article ID 138578

189. Bruchez Jr., M., Moronne, M., Gin, P., Weiss, S., Alvisatos, A.P. *Science* 281(1998)2013

190, Mendintz, I.L., Uyeda, H.T., Goldman, E.R., Mattoussi, H. *Nature Materials* 4(2005)435

191. Fernandiz-Suarex, A., Ting, Y. *Nature Rev. Molecular Cell Biol*. 9(2008)929

192. Xu, C.J., Tung, G.A., Sun, S.H. *Chem. Mater.* 20(2008)4167

193. Li, J., Li, H., Wang, K., Zhang, X., Yao, C., Zhang, Y., Yuan, P. *Optics Express* 21(2013)21414

194. Petryayera, E., Algar, W.R., Medintz, I.L. *Appl. Spectrosc.* 67(2013)215

195. Yguerabide, J., Yguerabide, E.E. *Anal. Biochem.* 262(1998)137

196. Shaner, N.C., Steinbach, P.A., Tsien, R.Y. *Nature Methods* 2(2005)905

197. Elsaesser, A., Howard, C.V. *Adv. Drug Delivery Rev*. 64(2012)129

198.Gopee, N.V., Roberts, D.W., Webb, P., Cozart, C.R., Sitonen, P.H., Warbitton, A.R., Yu, W.W., Colvin, V.L., Walker, N.J., Howard, P.C. *Toxicol. Sci*. 98(2007)249

199. Jackson, B.P., Bugge, D., Ranville, J.F., Chen, C.Y. *Environ. Sci. Technol*. 46(2012)5550

200. Bruneau, A., Fortier, M., Gagne, F., Gagnon, C., Turcotte, P., Tayabal, A., Davis, T.L. Auffret, M., Fournier, M. *Environ. Sci. Processes Impacts* 15(2013)596

201. Kim, D., Park, S., Lee, J.H., Jeong, Y.Y. Jon, S. *J. Amer. Chem. Soc.* 129(2007)7661

202. Pasternak, J.J., Williamson, E.E. *Mayo Clinic Proceedings* 87(2012)390

203. Attia, M., Anton, N., Akasov, R., Chiper, M., Markvicheva, E., Vandanme, T.F. *Pharma. Res*. (2015)1

204. Eghtedari, M., Oravsky, A., Copeland, J.A., Kotov, N.A., Conjusteau, A., Motmedi. M. *Nano Lett*. 7(2007)1914

205. Chen, H., Sun, Z., Ni, W., Woo, K.C., Lin, H.Q., Song, L., Yan, C., Wang, J. *Small* 5(2009)2111

206. Boote, E., Fent, G., Kattumuri, V., Casteel, S., Katti, K., Chandra, N., Kannan, R., Katti, K., Churchill, R. *Acad. Radio*. 17(2010)410

207. Khlebtsov, N., Dykman, L. *Chem. Soc. Rev.* 40(2011)1647

208. Alric, C., Taleb, J., Le Duc, G., Mandon, C., Le Meur-Herland, A. C., Brochard, T., Vocanson, F., Janier, M., Perrieat, P., Roux, S. Tilement, O. *J. Amer. Chem. Soc.* 130(2008)5908

209. Ahn, S., Jung, S.Y., Lee, S.J. *Molecules* 18(2003)5859

210. Alkilany, A.M., Murphy, C.J. *J. Nanopart. Res.* 12(2010)2313

211. Zhang, Q., Iwakuma, N., Sharma, P., Moudgil, B.M., Wu, C., McNeill, J., Jiang, H., Grobmyer, S.R. *Nanotechnology* 20)2009)395102

212. Lu, W., Huang, Q., Ku, G., Wen, X., Zhou, M., Guzatov, D., Brecht, P., Su, R., Oraevsky, A., Wang, L.V., Li, C. *Biomaterials* 31(2010)2617

213. Sun, Y., Mayers, B., Xia, Y. *Adv. Mater*. 15(2003)641

214. Pansare, V., Hejazi, S., Prudhomme, R.K. *ACS Chem. Mater*. 24(2012)812

215. Sun, J., Goldys, E.M. *J. Phys. Chem. C.* 112(2008)9261

216. Jain, P., Kyeong, S.L., El-Sayed, I.H., El-Sayed, M.A. *J. Phys. Chem. B.* 110(2006)7238

217. Xu, M., Wang, L.V. *Rev. Sci. Instr*. 77(2006)041101

218. Li, W., Chen, X. *Nanomedicine* 10(2015)299

219. Van de Berg, P.J., Daoudi, K., Stenberger, W. *Photoacoustics* 2(2015)89

220. Liang, X., Deng, Z., Jing, L., Dai, Z., Huang, M. *Chem. Commun*. 94(2013)11029

221. Balasundaram, G., Ho, C.J.H., Li, K., Driessen, W., Dinish, U.S., Wong, C.L., Ntziachristos, V., Li, B., Olivo, M. *Int. J. Nanomed*. 10(2015)387

222. Dinish, U.S., Song, Z., Ju, C., Ho, H., Balasundaram, G., Attia, A.B.E., Lu, X., Tang, B.Z., Liu, B., Olivo, M. *Adv. Funct. Mater.* 25(2015)2316

223. Schwartzberg, A.M., Zhang, J.Z. *J. Phys. Chem. C* 112(2008)10323

224. Wang, X., Wang, C., Cheng, L., Lee, S.T., Liu, Z. *J. Amer. Chem. Soc*. 134(2012)7414

225. Young, J., Figueroa, E., Drezek, R. *Ann. Biomed. Eng*. 40(2012)438

226. Sperling, R., Rivera, G., Zhang, F., Zanell, M., Parak, W. *Chem. Soc. Rev*. 37(2008)1896

227. Lu, W., Xiong, C., Zhang, G., Huang, Q., Zhang, R., Zhang, *J. Clin. Cancer. Res.* 15(2009)876

228. Lu, W., Zhang, G., Zhang, R., Flores, L., Huang, Q., Gelovani, J., Li, C. *Cancer Res.* 70(2010)3177

229. Melancon, M., Lu, W., Yang, Z., Zhang, R., Cheng, Z., Elliot, A., Stafford, J., Olson, T., Zhang, J. Li, C. *Mol. Cancer Ther*. 7(2008)1730

230. Myroshnychenko, V., Rodriquez-Fernandez, J., Pastoriza-Santos, I., Funston, A., Novo, C., Mulvaney, P., Liz-Marzan, L., Garcia de Abajo, F. *Chem. Soc. Rev*. 37(2008)1792

231. Everts, M., Saini, V., Leddon, J., Kok, R., Stoff-Khalili, M., Preuss, M., Milican, C., Perkins, G., Brown, J., Bagaria, H., Nikles, D., Johnson, D., Zharov, V., Curiel, D. *Nano Lett.* 6(2006)587

232. Lu, W., Tian, M. *Drug Delivery Applications of Noninvasive Imaging: Validation from Biodistribution to Sites of Action;* John-Wiley & Sons, Inc.: Hoboken, NJ 2013; pp 308-332

233. Liang, H., Wan, L., Bai, C., Jiang, L. *J. Phys. Chem. B* 109(2005)7795

234. Hirsch, L., Stafford, R., Bankson, J. Sershen, S., Rivera, B., Prices, R., Hazle, J., Halas, N. J., West, *J. Proc. Natl. Acad. Sci. USA* 100(2003)13549

235. Hirsch, L, Gobin, A., Lowery, A., Tam, F., Drezek, R., Halas, N.J. *Ann. Biomed. Eng.* 34(2006)15

236. Lowery, A., Gobin, A., Day, E., Halas, N.J., West, *J. Int. J. Nanomed.* 1(2006)149

237. Jain, P., Huang, X., El-Sayed, I., El-Sayed, M. *Acc. Chem. Res.* 41(2008)1842

238. Dickerson, E., Dreaden, E., Huang, X., El-Sayed, I. H., Chu, H., Pushpanketh, S., McDonald, J., El-Sayed, M.A. *Cancer Lett.* 269(2008)57

239. Goodrich, G., Bao, L., Gill-Sharp, K., sang, K., Wang, J., Payne, J. *J. Biomed. Opt.* 15(2010)018001

240. Gobin, A., Moon, J., West, J. *Int. J. Nanomed.* 3(2008)351

241. Melancon, M., Zhou, M., Zhang, R., Allen, P., Wen, X., Huang, Q., Wallace, M., Myers, J., Stafford, R., Liang, D., Ellington, A., Li, C. *ACS Nano* 8(2014)4530

242. Chithranit, B., Ghazani, A., Chan, W. *Nano Lett.* 6(2006)662

243. El-Sayad, M.A. *Acc. Chem. Res*. 37(2004)326

244. Parab, H., Chen, H., Lai, T., Huang, J., Chen, P., Liu, R., Hsiao, M., Chen, C., Tsai, D., Hwu, Y. *J. Phys. Chem. C* 113(2209)7574

245. Akilany, A., Murphy, C.J. *J. Nanopart. Res.* 12(2010)2313

246. Zhang, J.Z. *J. Phys. Chem. Lett.* 1(2010)686

247. Chen, J., Glaus, C., Laforest, R., Shang, Q., Yang, M., Gidding, M., Welch, M., Xia, Y. *Small* 6(2010)811

248. Sun, Y., Mayers, B., Xiz, Y. *Adv. Mater.* 15(2003)641

249. von Maltzahn, G., Park, J., Agrawal, A., Bandaru, N., Sailor, M., Bhatia, S. *Cancer Res.* 69(2009)3892

250 Yuan, H., Khoury, C., Wilson, C., Grant, G., Bennett, A., VoDinh, T. *Nanomed. Nanotechnol. Bio. Med*. 8(2012)1355

251. Huang, X., Jain, P., El-Sayed, I.H., El-Sayed, M.A. *Lasers Med. Sci.* 23(2008)217

252. Melancon, M., Lu, W., Yang, Z., Cheng, Z., Elliot, A., Stafford, J., Olson, T., Zhang, J., Li, C. *Mol. Cancer Ther.* 7(2008)1730

253. Zharov, V., Galitovskaya, E., Johnson, C., Kelly, T. *Lasers Surg. Med*. 37(2005)219

254. Jain, P., Huang, X., El-Sayed, I.H., El-Sayed, M.A. *Acc. Chem. Res*. 41(2008)1578

255. Nam, J., Won, N., Jin, H., Chung, H., Kim, S. *J. Amer. Chem. Soc*. 131(2009)13639

256. Oyelere, A., Chen, P., Huang, X., El-Sayed, M.A. *Bioconjugate Chem.* 18(2007)1490

257. Huang, X., El-Sayed, I.H., Qian, W., El-Sayed, M.A. *J. Amer. Chem. Soc.* 128(2006)2115

258. Gobin, A., Lee, M., Halas, N.J., James, W., Drezek, R., West, *J. Nano Lett.* 7(2007)1929

259. Loo, C., Lowery, A., Halas, N.J., West, J., Drezek, R. *Nano Lett.* 5(2005)709

260. Gobin, A., Watkins, E. Queredo, E., Covin, V., West, J. *Small* 6(2010)745

261. Ke, H., Wang, J., Dai, Z., Jin, Y., Qu, E., Xing, Z., Guo, C., Yue, X., Liu, J. *Angew. Chem.* 123(2011)3073

262. Ji, X., Shao, R., Elliott, A., Stafford, J., Esparza-Coss, E., Bankson, J., Liang, G., Luo, Z., Park, K., Market, J., Li, C. *J. Phys. Chem. C.* 11(2007)6245

263. Jin, S., Jiang, Y., Qiu, R., Rauch, T., Wang, Y., Schackert, G., Krex, D., Lu, Q., Pfeifer, G. *Cancer Res.* 71(2011)7360

264. Bardhan, R., Chen, W., Perez-Torres, C., Bartels, M., Huschka, R., Zhao, L., Morosan, E., Pautler, R., Joshi, A., Halas, N.J. *Adv. Funct. Mater.* 19(2009)3901

265.Chen, W., Avala-Orozco, C., Biswal, N., Perez-Torres, C., Bartels, M., Bardhan, R., Stinnet, G., Liu, X., Ji, B., Deorukhkar, A., Brown, L., Guhas-Pautler, R., Krishnan, S., Halas, N.J., Joshi, A. *Nanomedicine* 9(2014)1209

266. Schwartzberg, A.M., Oshiro, T., Zhang, J.Z. Huser, T. Talley, C. *J. Phys. Chem. B* 110(2006)19935

267. Dowgiallo, A., Knappenberger, K. *Phys. Chem. Chem. Phys*. 13(2011)21585

268. Dowgiallo, A., Schwartzberg, A.M., Knappernberger, K. *Nano Lett*. 11(2011)3258

269. Preciado-Flore, S., Wang, D., Wheeler, D.A., Newhouse, R., Hensel, J., Schwartzberg, A.M., Wang, L., Zhu, J., Barboza-Flores, M., Zhang, J.Z. *J. Mater. Chem*. 21(2011)2344

270. Xie, H., Larmour, Y., Wark, A., tileli, V., McComb, D., Faulds, K., Graham, D. *Nanoscale* 5(2013)765

271. Schwartzberg, A.M., Grant, C., Wolcott, A., Talley, C., Huser, T., Bogomolini, R., Zhang, J.Z. *J. Phys. Chem. B* 108(2004)19191

272. Schwartzberg, A.M., Olson, T., Talley, C., Zhang, J.Z. *Anal. Chem.* 78(2006)4732

273. Kobayashi, Y., Horie, M. Konno, M., Rodriquez-Gonzalez, B., Liz-Marzan, L *J. Phys. Chem. B* 107(2003)7420

274. Salgueirino-Maceira, V., Correa-Durte, M., Farle, M., Lopez-Quintela, M., Sieradki, K., Diaz, R. *Langmuir* 22(2006)1455

275. Yang, W.; Gooding, J. J.; He, Z.; Li, Q.; Chen, G. *Journal of Nanoscience and Nanotechnology* 7(2007)712

276. Chai, F.; Wang, C.; Wang, T.; Ma, Z.; Su, Z. *Nanotechnology* 21(2010) 025501

277. Guan, J.; Jiang, L.; Li, J.; Yang, W. *J. Phys. Chem. C* 112(2008)3267

278. Turkevich, J.; Stevenson, P.C.; and Hillier, J. *Discuss Faraday Soc.* 11(1951)55

279. Frens, G. *Natl. Phys. Soc.* 241(1971)20

280. Chen, S.; Fang, Y.M.; Xiao, Q.; Li, J.; Li, S. B.; Chen, H. J.; Sun, J. J.; Yang, H. H. *Analyst* 137(2012)2021

281. Tro, N.J. *Chemistry: A Molecular Approach. 3rd Ed.* Pearson: Upper Saddle River, NJ. 2014; pA-10

282. Garrett, R.H., Grisham, C.M. *Biochemistry 5th Ed*.; Brooks/Cole, Cengage Learning: Belmont, CA. 2013: p 84

283. Kim, B.H. *Kyungrak System and Theory of Sana.* Medical Science Press, Pyongyang Democratic Peoples Republic of Korea 1965.

284. Shin, H.S., Johng, H.M., Lee, B.C., Cho, S.I., Soh, K.S., Baik, K.Y., Yoo, J.S., Soh, K.S. *Anatomical Record Part B New Anatomist* 284(2005)35

285. Nam, M.H., Lim, J., Choi, S.H., Kim, S., Soh, K.S. *J. Acupuncture Meridian Studies* 5(2012)210

286. Lee, B.C., Kim, K.W., Soh, K.S. *J. Acupuncture Meridian Studies* 2(2009)66

287. Yoo, J.S., Kim, M.S., Ogay, V., Soh, K.S. *Indian J. Exp. Bio*. 46(2008)336

288. Lee, C., Seol, S.K., Lee, B.C., Hong, Y.K., Je, J.H., Soh, K.S. *Lymphat. Res. Biol.* 4(2006)181

289. Lee, B.C., Soh, K.S. *Lymphology* 41(2008)178

290. Kim, B.H. *On the Kyungrak System.* Foreign Language Publishing House. Pyongyang Democratic People Republic of Korea. 1964

291. Kim, B.H. *Great Discovery in Biology and Medicine: Substances of Kyungrak*. Foreign Language Publishing House. Pyongyang, Democratic Peoples Republic of Korea. 1962

292. Lee, S.J., Park, S.H., Kim, Y.I., Hwang, S., Kwon, P.M., Han, I.S., Kwon, B.S. *Stem Cells Dev.* 2014

293. Hwang, S., Lee, S.J., Park, S.H., Chitteti, B.R., Srour, E.F., Cooper, S., Hangoc, g., Broxmeyer, H.E., Kwon, B.S. *Stem Cells Dev.*23(2014)2661

294. Noh, Y.I., Rho, M., Yoo, Y.M., Jung, S.J., Lee, S.S. *J. Acupuncture Meridian Studies* 5(2015)201

295. Kang, K.A., Madonado, C. Perez-Aradia, G., An, P., Soh, K.S. *Adv. Exp. Med. Biol.* 789(2013)289

296. Johng, H.M., Yoo, J.S., Yoon, T.J., Shin, H.S., Lee, B.C., Lee, C., Lee, J.K., Soh, K.S. *Evid. Based Compl. Alternat. Med.* 4(2007)77

297. Lee, S., Ryu, Y., Cha, J., Lee, J.K., Soh, K.S., Kim, S., Lim, J. *J. Acupuncture Meridian Studies* 5(2012)206

298. Lim, J., Jung, J.H., Lee, S., Su, Z., Qiang, Z., Cha, J.M., Lee, J.K., Soh, K.S. *J. Biomed. Optics* 16(2011)116010

299. Lee, B.C., Yoo, J.S., Baik, K.Y., Kim, K.W., Soh, K.S. *Anatomical Record Part B, New Anatomist* 286(2005)1

300. Jung, S.J., Bae, K.H., Nam, M.H., Kwon, H.M., Song, Y.K., Soh, K.S. J. *Acupuncture Meridian Studies* 6(2013)306

301. Jung, S.J., Cho, S.Y., Bae, K.H., Hwang, S.H., Lee, B.C., Kim, S., Kwon, B.S., Kwon, H.M., Song, Y.K., Soh, K.S. *J. Acupuncture Meridian Studies* 5(2012)234

302. Lee, S.H., Bae, K.H., Kim, G.O., Nam, M.H., Choi, Y.B., Kwon, H.M., Ryu, Y., Soh, K.S. *Evid. Based Compl. Alternat. Med*. 2013(2013)472704

303. Kim, M.S., Oh, S.W., Lim, J.H., Han, S.W. *Appl. Phys. Lett.* 97(2010)96

304. Yoo, J.S., Ayati, M.H., Kim, H.B., Zhang, W.B., Soh, K.S., *PLoS One* 5(2010)e9940

305. Lee, B.C., Yoo, J.S., Ogay, V., Kim, K.W., Dobberstein, H., Soh, K.S. *Microsc. Res. Tech*. 70(2007)34

306. Sung, B., Kim, B.S., Lee, B.C., Yoo, J.S., Lee, S.H., Kim, Y.J., Kim, K.W., Soh, K.S. *Naturwissenschaften* 95(2008)117

307. Kneipp K, Wang Y, Kneipp H, Perelman LT, Itzkan I, Dasari R. *Phys. Rev. Lett*. 78(1997)1667

308. Nie, S.M., Emery, S.R. *Science* 275(1997)1102

309. Vlckova, B., Pavel, .I, Sladkova, M., Siskova, K., Slouf, M.. *J. Mol. Struct.* 834(2007)42

310. Michaels, A.M., Nirma,,l M., Brus, L.E. *J. Amer. Chem. Soc*. 121(1999)0032

311. Tian, Z.Q., Ren, B., Li, J.F., Yang, Z.L. *Chem. Commun*. 34(2007)3514

312. Li, J.F., Ding, S.Y., Yang, Z.L., Bai, M.L., Anema, J.R., Wang, X. *J. Amer. Chem. Soc.* 133(2011)15922

313. Olson, T.Y., Schwartzberg, A.M., Ome, C.A., Talley, C.E., O'Connell, B., Zhang, J.Z. *J. Phys. Chem. C* 112(2008)6319

314. Pagliai, M., Caporali, S., Muiz-Miranda, M., Pratesi, G., Schettino, V. *J. Phys. Chem. Lett*. 3(2012)242

315. Schwartzberg, A.M., Grant, C.D., Wolcott, A., Talley, C.E., Huser, T.R., Bogomolni, R. *J. Phys. Chem. B*. 108(2004)19191

316. Schwartzberg, A.M., Oshiro, T.Y., Zhang, J.Z., Talley, C.E. *Anal. Chem*. 78(2006)4732

317. Yang, J., Wang, Z.Y., Zong, S.F., Song, C.Y., Zhang, R.H., Cui, Y.P. *Anal. Bioanal. Chem.* 402(2012)1093

318. Preciado-Flores, S., Wheeler, D.A., Tran, T.M., Tanaka, Z., Jiang, C.Y., Barboza-Flores, M. *Chem. Commun.* 47(2011)4129

319. Yang, D.P., Chen, S.H., Huang, P., Wang, X.S., Jing, W.Q. Pandoli, O. *Green Chem.* 12(2010)2038

320. Laucks, M.L., Sengupta, A., Junge, K., Davis, E.J., Swanson, B.D. *Appl. Spectrosc.* 59(2005)1222

321. Li, J.F., Huang, Y.F., Ding, Y., Yang, Z.L., Li, S.B., Zhou, X.S. *Nature* 464(2010)392

322. Anema, J.R., Li, J.F., Yang, Z.L., Ren, B., Tian, Z.Q. *Annual Rev. Anal. Chem.* 4(2011)129

323. Fernandez-Lopez, C., Mateo-Mateo, C., Alvarez-Puebla, R.A., Perez-Juste, J., Pastoriza-Santos, I., Liz-Marzan, L.M. *Langmuir* 25(2009)13894

324. Fales, A.M., Yuan, H., Vo-Dinh, T. *Langmuir* 27(2011)12186

325. Huang, J., Kim, K.H., Choi, N., Chon, H., Lee, S., Choo, J. *Langmuir* 27(2011)10228

326. Wolcott, A., Gerion, D., Visconte, M., Sun, J., Schwartzberg, A.M. Chen, S.W. *J. Phys. Chem. B* 110(2006)5779

327. Tian, Y., Hue, R.N., Yu, J.C., Chen, B.J., Sun, J.S., Cheng, L.H. *Chin. J. Chem.* 28(2010)921

328. Du, G.H., Liu, Z.L., Xia, X., Chu, Q., Zhang, S.M. *J. Sol-Gel Sci. Technol.* 39(2006)285

329. Bean, K., Black, C.F., Govan, N., Reynolds, P., Sambrook, M.R. *J. Colloid Interface Sci*. 366(2012)16

330. Jian, Y., Van de Broek, B., De Palma, R., Libaers, W., Clays, K., Van Roy, W. *Colloids Surf. A Physiochem. Eng. Aspects* 322(2008)225

331. Wang, D.Y., Caruso, R.A., Caruso, F. *Chem. Mater.* 13(2001)364

332. Wang, G.H., Zhang, Y., Zhang, D.H., Fan, J.P. *Int. J. Miner. Metall. Mater*. 19(2012)179

333. Zhang, J.X., Sun, W., Bergman, L., Roseholm, J.M., Linden, M., Wu, G.*J. Mater. Lett.* 67(2012)379

334. Liz-Marzan, L.M., Giersig, M., Mulvaney, P. *Langmuir* 12(1996)4329

335. Stober, W., Fink, A., Bohn, E. *J. Colloid, Interface Sci*. 26(1968)62

336. Wheeler, D.A., Newhouse, R.J., Wang, H.N., Zou, S.L., Zhang, J.Z. *J. Phys. Chem. C.* 114(2010)18126

337. Liz-Marzan, L.M., Giersig, M., Mulvaney, P. *Langmuir* 12(1996)4329

338. Liang, H.P., Wan, L.J., Bai, C.L., Jiang, L. *J. Phys. Chem. B.* 109(2005)7795

339. Ori, G., Gentili, D., Cavallini, M., Franchini, M.C., Zapparoli, M., Montorsi, M. *Nanotechnology* 5(2012)23

340. Rodriguez-Gonzalez, B., Burrows, A., Watanbe,M., Kiely, C.J., Liz-Marzan, L.M. *J. Mater. Chem.* 15(2005)1755

341. Speeding, F.M., Stamm, R.F *J. Chem. Phys.* 10(1942)176

342. Jiles, D. *Introduction to Magnetism and Magnetic Materials 3rd Ed*. CRC Press. Taylor and Francis Group. 2016

343. McQuarrie, D.A., Simon, J.D. *Physical Chemistry A Molecular Approach*. University Science Books. 1997

344. Stohr., J., Siegmann, H.C. *Magnetism From Fundamentals to Nanoscale Dynamics*. Springer, Berlin, Heidelberg. 2006

345. Fagaly, R.L. *Rev. Sci. Intsrum.* 77(2006)101101

346. Gallop, J.C., Petly, B.W. *J. Phys. E. Sci. Instrum.* 9(1976)417

347. Sawickil, M., Stefanowiczl, W., Ney, A. *Semicond. Sci. Technol*. 26(2011)063006

348. Aviv., G. *Experimental Physics Course: Superconducting Quantum Interference Device*. Depart. Phys. Ben-Guiron University of the Negev, Israel. 2008

349. Dennis, C.L., Ivkov, R. *Int. J. Hyperthermia* 29(2013)715

350. Carrey, J., Medhadaoui, B., Respaud, M. *J. Appl. Phys*. 109(2011)083921

351. Gupta, A.K., Gupta, M. *Biomaterials* 26(2005)3995

352. Baker, I., Zeng, Q., Li, W., Sullivan, C.R. *J. Appl. Phys.* 99(2006)08H106

353. Das, R., Rindaldi-Montes, N., Alonso, J., Amghouz, Z., Garaio, E, Garcia, J.A., Gorria, P., Blanco, J.A., Phan, M.H., Snikanth, H. *ACS Appl. Mater, Interfaces* 8(2016)25162

354. Banobre-Lopez, M., Teijeiro, A., Rivas, J. *Reports Practical Oncology Radiotherapy* 18(2013)397

355. Conde-Leboran, I., Baldomir, D., Martinez-Boubeta, C., Chubykalo-Fesenko, O., del Puerto Morales, M., Salas, G., Cabrera, D., Camarero, J., Teran, F.J., Serates, D. *J. Phys. Chem. C*. 119(2015)15698

356. Deatsch, A.E., Evans, B.A. *J. Mag. Mag. Mater.* 354(2014)163

357. Mehdaoui, B., Meffre, A., Carrey, J., Lachaize, S. Lacroix, L.M., Gougeon, M., Chaudret, B., Respaud, M. *Adv. Funct. Mater.* 21(2011)4573

358. Hergt, R., Dutz, S., Roder, M. *J. Phys. Condens. Mater.* 20(2008)385214

359. Malekigorji, M., Malekigorji, M., Holman, J., Skidmore, M. Hoskins, C. *Nanomedicine Nanotechnology* 6(2015)1000375

360. Rowland, C. E.; Brown III, C.W.; Delehanty, J. B.; Medintz, I. L. *Materials Today* 19(2006)464

361. Cashin, V. B.; Eldridge, D. S.; Yu, A.; Zhao, D. *Environ. Sci. Water. Res.* Technol. 2018 Advance Article

362. Lui, S.; Zhang, S.; Guo, J.; Wen, J.; Qiao, Y. *J. Mag. Mag. Mater*. 422(2017)280

363. Ali, J.; Najeeb, J.; Asim, M.; Farhan-Aslam, M.; Raza, A. J. *Biosens. Bioelectron*. 8(2017)1000235

364. Ragelle, H.; Danhier, F.; Preat, V.; Langer, R.; Anderson, D.G. *Expert Opinion Drug Delivery* 14(2017)851

365. Reddy, D. H. K.; Yun, Y.S. *Coord. Chem. Rev.* 315(2016)90

366. Yadav, K.K.; Singh, J.K.; Gupta, N.; Kumar, V. *J. Mater. Environment. Sci.* 2(2017)740

367. Lu, F.; Astruc, D. *Coord. Chem. Rev.* 356(2018)147

368. Fan, Z.; Shelton, M.; Kumar-Singh, A.; Senapati, D.; Khan, S.A.; Chandra-Ray, P. *ACS Nano* 6(2012)1065

369. Tian, X.; Zhang, L.; Yang, M.; Bai, L.; Dai, Y.; Yu, Z.; Pan, Y. *Nanomed. Nanobiotechnol*. 2018, 10:e1476. DOI:10.1002/wnan.1476

370. Bhatia, P.; Singh-Verma, S.; Sinha, M. M. *Adv. Nano Res*. 2018. 1, DOI: 10.21467

371. Das, R.; Rinaldi-Montes, N.; Alonso, J.; Amghouz, Z.; Garaio, E.; Garcia, J. A.; Gorria, P.; Blanco, J.A.; Phan, M.H.; Srikanth, H. *ACS Appl. Mater. Interfaces*. 8(2016)25162

372. Leung, K.C.F.; Xuan, S. *Chem. Rec*. 16(2016)458

373. Stafford, S.; Serrano-Garcia, R.; Gun'ko, Y. *Appl. Sci*. 8(2018)97

374. Esenturk, E. N.; Hight-Walker, A.R. *J. Nanopart. Res.* 151(2013)1364

375. Bagheri, S.; Aghaei, H.; Ghaedi, M.; Asfaram, A.; Monajemi, M.; Akbar-Bazrafshan, A. *Ultrasonics Chem*. 41(2018)279

376. Levin, C.S.; Hofmann, C.; Ali, T.A.; Kelly, A.T.; Morosan, E.; Nordlander, P.; Whitmire, K.H.; Halas, N.J. *ACS Nano* 3(2009)1379

377. Paterson, S.; Thompson, S.A.; Wark, A.W.; de la Rica, R. *J. Phys. Chem. C* 121(2017)7404

378. Rajkumar, S.; Prabaharan, M. *Current Topics Med. Chem.* 17(2017)1858

379. Sanavio, B.; Stellacci, F. *Current Topics Med. Chem.* 24(2017)497

380. Gaurdia, P.; Nitti, S.; Materia, M.E.; Pugliese, G.; Yaacoub, N.; Greneche, J.M.; Lefevre, C.; Manna. L.; Pellegrino, T. *J. Mater. Chem. B* 24(2017)4587

381. Hatchtel, J.A.; Yu, S.; Lupini, A.R.; Pantelides, S.T.; Gich, M.; Laromaine, A.; Roig, A. *Faraday Discuss*. 191(2016)215

382. Mohammad, F.; Yusof, N.A. *J. Colloid. Interface Sci.* 434(2014)89

383. Sabale, S.; Kandesar, P.; Jadhav, V.; Komorek, R.; Kishan-Motkuri, R.; Yu, X.Y. *Biomater. Sci.* 5(2017)22122

384. Han, L.; Zhang, Y.; Zhang, Y.; Shu, Y.; Chen, X.W.; Wang, J.H. *Talanta* 171(2017)32

385. Monaco, I.; Arena, F.; Biffi, S.; Locatelli, E.; Bortat, B.; La Cava, F.; Marini, G.M.; Severini, G.M.; Terreno, E.; Comes-Franchini, C. *ACS Bioconj. Chem.* 28(2017)1382

386. Meledandri, C.J.; Stolarczyk, J.K.; Brougham, D.F; *ACS Nano* 5(2011)1747

387. Chithrani, B.D.; Chan, W.C.W. *ACS Nano Lett*. 7(2007)1542

388. Salihov, S.V.; Ivanenkov, Y.A.; Krechetov, S.P.; Veselov, M.S.; Sviridenkova, N.V.; savchenko, A.G.; Klyachko, N.L.; Golovin, Y.I.;

Chufarova, N.V.; Beloglazkina, E.K.; Majouga, A.G. *J. Mag. Mag. Mater*. 394(2015)173

389. Nochehdehi, A.R.; Thomas, S.; Sadri, M.; Afghahi, S.S.S.; Hadavi, S.M. J. *Nanomed. Nanotechnol.* 8(2017)1000423

390. Aadinath, W.; Ghosh, T.; Anandharamakrishnan, C. *J. Mag. Mag. Mater.* 401(2016)1159

391. Deatsch, A. E.; Evans, B.A. *J. Mag. Mag. Mater.* 354(2014)163

392. Kaur, P.; Aliru, M.L.; Chadha, A.S.; Asea, A.; Krishnan, S. *Int. J. Hyperthermia* 32(2016)76

393. Hedayatnasab, Z.; Abnisa, F.; Daud, W.M.A.W. *Mater. Design* 123(2017)174

394. Esenturk, E.N.; Hight-Walker, A.R. *J. Nanopart. Res.* 15(2013)1364

395. Zhou, X.; Xu, W.; Wang, Y.; Kuang, Q.; Shi, Y.; Zhong, L.; Zhang, Q. *J. Phys. Chem. C* 114(2010)19607

396. Bao, F.; Yao, J.L.; Gu, R.A. *Langmuir* 25(2009)10782

397. Salguerino-Maceira, V.; Correa-Duarte, M.A.; Farle, M.; Lopez-Quintela, A.; Sieradzki, K.; Diaz, R. *Chem. Mater.* 18(2006)2701

398. Lee, D.K.; Song, Y.; Tran, V.T.; Kim, J.; Park, E.Y.; Lee, J. *J. Colloid. Interface Sci.* 499(2017)54

399. Wang, J.; Wu, X.; Wang, C.; Rong, Z.; Ding, H.; Li, H.; Li, S.; Shao, N.; Dong, P.; Xiao, R.; Wang, S. *ACS Appl. Mater. Interfaces* 8(2016)19958

400. Qiu, Y.; Deng, D.; Deng, Qianwen, D.; Wu, P.; Zhang, H.; Cai, C. *J. Mater. Chem. B* 22(2015)4487

401. Li, F.; Yu, Z.; Zhao, L.; Xue, T. *RSC Adv.* 6(2016)10352

402. Paterson, S.; Thompson, S.A.; Wark, A.W.; de la Rica, R. *J. Phys. Chem. C* 121(2017)7404

403. Guerrini, L.; Graham, D. *Chem. Soc. Rev.* 41(2012)7085

404. Garber, A.J. *Diabetes Care* 34(2011)S279

405. Liu, B.; Han, M.; Guan, G.; Wang, S.; Liu, R.; Zhang, Z. *J. Phys. Chem. C* 115(2011)17320

406. Wu, W.; Wu, Z.; Yu, T.; Jiang, C.; Kim, W.S. *Sci. Technol. Adv. Mater*. 16(2015)023501

407. Stober, W.; Fink, A.; Bohn, E. J. *Colloid Interface Sci.* 26(1968)62

408. Kah, J.C.; Phonthammachai, N.; Wan, R.C.Y.; Song, J.; White, T.; Mhaisalkar, S.; Ahmad, I.; Sheppard, C.; Olivo, M. *Gold Bulletin* 41(2008)23

409. Schwartzberg, A.M.; Grant, C.D.; Wolcott, A.; Talley, C.E.; Huser, T.R.; Bogomolni, R.; Zhang, J.Z. *J. Phys. Chem. B* 108(2004)19191

410. Selbes, Y.S.; Caglayan, M.G.; Eryilmaz, M.; Boyaci, I.H.; Saglam, N.; Basaran, A.A.; Tamer, U. *Anal. Bioanal. Chem.* 408(2016)8447

411. Garitaonandia, J.S., Goikolea, E., Insausti, M., Suzuki, M., Kawamura, N., Osawa, H., Gil del Muro, I., Suzuki, K, Cashion, J.D., Gorria, C., Plazaola, F., Rojo, T. *J. Appl. Phys.* 105(2009)07A907

412. Trudel, S. *Gold Bull.* 44(2011)3

413. Nealon, G.L., Donnio, B., Greget, R., Knappler, J.P., Terazzi, E., Gallani, J.L. *Nanoscale* 4(2012)5244

414. Crespo, P., de la Presa, P., Marin, P., Multigner, M., Alonso, J.M., Rivero, G., Yndurain, F., Gonzalez-Calbet, M.G., Hernando, A. *J. Phys. Cond. Mater.* 25(2013)484006

415. Tuboltsev, V., Savin, A., Pirojenko, A., Raisanen, J. *ACS Nano* 7(2013)6691

416. Hori, H., Teranishi, T., Nakae, Y., Seino, Y., Miyake, M., Yamada, S. *Phys. Lett. A* 263(1999)406

417. Carmeli, I., Leitus, G., Naaman, R., Reich, S., Vager, Z. *Israel J. Chem.* 43(2003)399

418. Yamamoto, Y., Hori, H. *Rev. Adv. Mater. Sci.* 12(2006)23

419. Taniyama, T., Ohta, E., Sato, T. *Europhys. Lett.* 38(1997)195

420. Magyar, R.J., Mujica, V., Marquez, M., Gozalez, C. *Phys. Rev. B* 75(2007)144421

421. Crespo, P., Litran, R., Rojas, T.C., Multigner, M., de la Fuente, J.M., Sanchez-Lopez, J.C., Garcia, M.A., Hernando, A., Penades, S., Fernandez, A. *Phys. Rev. Lett.* 93(2004)087204

422. Luo, W., Pennycook, S.J., Pantelides, S.T. *Nano Lett.* 7(2007)3134

423. Sodipo, B.K.; Aziz, A.A. *J. Mag. Mag. Mater.* 416(2016)275

424. Batlle, X.; Labarta, A. *J. Phys. D: Appl. Phys*. 35(2002)R15

425. Banerjee, S.; Raja, S.O.; Sardar, M.; Gayathri, N.; Ghosh, B.; Dasgupta, A. *J. Appl. Phys.* 109(2011)123902

426. Das, R.; Rinaldi-Montes, N.; Alonso, J.; Amghouz, Z.; Garaio, E.; Garcia, J.A.; Gorria, P.; Blanco, J.A.; Phan, M.H.; Srikanth, H. *ACS Appl. Mater. Interfaces* 8(2016)25162

427. Almasi-Kashi, M.; Ramazani, A.; Alikhanzadeh-Arani, S.; Pezeshki-Nejad, Z.; Montazer, A.H. *New J. Chem*. 40(2016)5061

428. Thorat, N.D.; Bohara, R.A.; Malgras, V.; Tofail, S.A.M.; Ahamad, T.; Alshehri, S.; Wu, K.C.W.; Yamauchi, Y. *ACS Appl. Mater. Interfaces* 8(2016)14656

429. Jalalian, M., Mirkazemi, S.M., Alamolhoda, S. *J. Mag. Mag. Mater.* 419(2016)363

430. Magura, J., Zelenakova, A., Zelenak, V., Kanuchova, M. *Appl. Surf. Sci.* 315(2014)392

431. Orlando, T., Capozzi, A., Umut, E., Bordonali, L., Mariani, M., Galinetto, P., Pineider, F., Innocenti, C., Masala, P., Tabak, F., Scavini, M., Santini, P., Corti, M., Sangregorio, C., Ghigna, P., Lascialfari, A. *J. Phys. Chem. C* 119(2015)1224

432. Behera, M., Ram, S. *Int. Nano Lett*. 3(2013)17

433. Carmeli, I. *Condensed Matter*. 2014, arXiv:1403.1471

434. Behera, M., Ram, S. *J. Incl. Phenom. Macrocycl. Chem*. 72(2012)233

435. Khairullin, I.I., Chen, Y., Hwang, L. *Chem. Phys. Lett.* 275(1999)1

436. Daniel, M.C., Astruc, D., *Chem. Rev.* 104(2004)293

437. Hoppe, C.E., Lazzari, M., Pardinas-Blanco, I., Lopez-Quintelz, I. *Langmuir* 22(2006)7027

438. Kemal, L., Jiang, X.C., Wong, K., Yu, A.B. *J. Phys. Chem. C* 112(2008)15656

439. Alexandridis, P. *Chem. Engg. Technol*. 34(2011)15

440. Shalklvicht, N., Escher, W., Burgi, T., Michel, B., Si-Ahmed, L., Poulikakos, D. *Langmuir* 26(2010)663

441. Ray, S.G., Cohen, H., Naaman, R., Liu, H., Waldeck, D.H. *J. Phys. Chem. B* 109(2005)14064

442. Jalian, M.; Mirkazemi, S.M.; Alamolhoda, S. *J. Mag. Mag. Mater.* 419(2016)363

443. De Faria, D.L.A., Gil, H.A.C. *J. Mol. Str.* 479(1999)93

444. de la Fuente, J. M., Alcantara, D., Eaton, P., Crespo, P., Rojas, T.C., Fernandez, A., Hernando, A., Pernades, S. *J. Phys. Chem. B* 110(2006)13021

445. Crespo, P., Garcia, M.A., Fernandez-Pinel, E., de la Vente, J., Merino, J.M., Quesada, A., Hernando, A. *Acta Physica Polonica A* 113(2008)515

446. Leff, D.V., Brandt, L., Heath, J.R. *Langmuir* 12(1996)4723

447. Lahiri, B.B., Muthukumaran, T., Philip, J. *J. Mag. Mag. Mater.* 407(2016)101

448. de la Presa, P., Multigner, M., de la Venta, J., Garcia, M.A. *J. Appl. Phys.* 100(2006)123915

449. Guerrero, E., Munoz-Marquez, A., Fernandez, A., Crespo, P., Hernando, A., Lucena, R., Conesa, J.C. *J. Appl. Phys.* 107(2010)064303

450. Crespo P.; de la Presa, P.; Marin, P.; Multigner, M.; Alonso, J.M.; Rivero, G.; Yndurain, F.; Gonzalez-Calbet, J. M.; Hernando, A. *J. Phys. Condens. Matter* 25(2013)484006

451. Polte, J., Kraehnert, R., Radtke, M., Reinholz, U., Riesmeier, H., Thunemann, A.F., Emmerling, F. *J. Physics Conference Series* 247(2010)1

452. Polte, J., Erle, R., Thunemann, A.F., Sokolov, S., Torsten-Ahner, T.T., Rademann, K., Emmerling, F., Kraehnert, R. *ACS Nano*. 4(2010)1076

453. Suda, M., Kameyama, N., Suzuki, M., Kawamura, N., Einaga, Y. *Angew. Chem. Int. Ed.* 47(2008)160

454. Zhang, P., Sham, T.K. *Phys. Rev. Lett*. 90(2003)245502